APPLICATION OF PRODUCT DESIGN CONCEPTS AND HYBRID SYSTEM DYNAMICS TO DEMONSTRATE ZENO BEHAVIOR AND ZENO PERIODIC ORBITS IN A PHYSICAL DOUBLE PENDULUM SETUP

A Thesis

by

BHARGAV KOTHAPALLI

Submitted to the Office of Graduate Studies of
Texas A&M University
in partial fulfillment of the requirements for the degree of

MASTER OF SCIENCE

May 2011

Major Subject: Mechanical Engineering

Application of Product Design Concepts and Hybrid System Dynamics to Demonstrate Zeno Behavior and Zeno Periodic Orbits in a Physical Double Pendulum Setup

APPLICATION OF PRODUCT DESIGN CONCEPTS AND HYBRID SYSTEM DYNAMICS TO DEMONSTRATE ZENO BEHAVIOR AND ZENO PERIODIC ORBITS IN A PHYSICAL DOUBLE PENDULUM SETUP

A Thesis

by

BHARGAV KOTHAPALLI

Submitted to the Office of Graduate Studies of
Texas A&M University
in partial fulfillment of the requirements for the degree of

MASTER OF SCIENCE

Approved by:

Co-Chairs of Committee,	Daniel A. McAdams
	Aaron D. Ames
Committee Members,	Andrew Duggleby
	Guido Kanschat
Head of Department,	Dennis O'Neal

May 2011

Major Subject: Mechanical Engineering

ABSTRACT

Application of Product Design Concepts and Hybrid System Dynamics to Demonstrate Zeno Behavior and Zeno Periodic Orbits in a Physical Double Pendulum Setup.

(May 2011)

Bhargav Kothapalli, B. Tech., Jawaharlal Nehru Technological University, India

Co-Chairs of Advisory Committee: Dr. Daniel A. McAdams
Dr. Aaron D. Ames

This thesis aims to explain how the concepts of functional modeling are implemented in the development and validation of real-world hybrid dynamic systems. I also discuss how control theory is integrated with the design process in order to understand the significance of periodic orbits on a simple dynamic system.

Two hybrid system applications with different levels of complexity will be considered in this thesis – an anthropomorphic Bipedal walking robot and a Double Pendulum with a mechanical stop. The primary objectives of this project are to demonstrate the phenomena of Zeno and zeno periodic orbits in hybrid dynamic systems involving impacts. Initially, I describe the salient features of the product design procedure and then explain the significance of functional modeling as a part of this process. We then discuss hybrid dynamic systems and the occurrence of Zeno behavior in their mathematical form. Also, the necessary conditions for existence of Zeno and

zeno equilibrium points are provided. Then the theory of completed Lagrangian hybrid systems is explained in detail.

We then examine the two hybrid dynamic systems being considered for this project. Prior research undertaken on bipedal walking is explored to understand their design and achievement of stable walking gaits with appropriate actuation mechanisms. Based on this insight, a suitable design procedure is employed to develop the bipedal robot model. The desired actuation mechanisms for all the configurations considered for this model as well as the challenges faced in employing optimal actuation will be discussed. However, due to the high level of complexity of the bipedal robot model, a simpler hybrid dynamic system is considered to simplify fabrication and control of the model. This is the motivation behind designing and building the Double Pendulum model with a mechanical stop in an attempt to observe zeno behavior in this system.

We begin by formally demonstrating that the "constrained" double pendulum model displays Zeno behavior and complete this Zeno hybrid system to allow for solutions to be carried past the Zeno point. The end result is periods of unconstrained and constrained motions in the pendulum, with transitions to the constrained motion occurring at the Zeno point. We then consider the development of a real physical pendulum with a mechanical stop and introduce non-plastic impacts. Later, we verify through experimentation that Zeno behavior provides an accurate description of the behavior of the physical system. This provides evidence to substantiate the claim that Zeno behavior, while it does not technically occur in reality, provides an accurate

method for predicting the behavior of systems undergoing impacts and that the theory developed to understand Zeno behavior can be applied to better understand these systems.

ACKNOWLEDGEMENTS

I would like to thank my co-chairs, Dr. Daniel McAdams and Dr. Aaron Ames, as well as my committee members, Dr. Andrew Duggleby and Dr. Guido Kanschat for their guidance and support throughout the course of this research.

I would like to convey my special thanks to my lab mates, Shishir Nadubettu Yadukumar, Ryan Sinnet, Eric Wendel, Ivan Joel Alaniz and Rigoberto Lopez for their invaluable assistance during various stages of this research. Thanks also go to my other lab members, friends and colleagues and the department faculty and staff for making my time at Texas A&M University a great experience.

Finally, thanks to my family for their encouragement and support in successfully accomplishing this endeavor.

TABLE OF CONTENTS

Page

LIST OF FIGURES

Page

Page

1. INTRODUCTION

Engineering design is an activity which affects almost every area of human life. It usually utilizes the laws and perceptions of science and personal experiences to provide essential requirements for obtaining solution ideas. Designing involves optimization of the product objectives while including all possible constraints [1]. The design process also aims to ensure that the system reliability does not directly depend on parameters that cannot be accurately determined. For any model, a formal mathematical validation and verification would be possible if its design process lends itself to formal and systematic methods. In this thesis, we will combine the concepts of *product design* with those of *hybrid system dynamics* to model two different hybrid dynamic systems, namely, an anthropomorphic bipedal robot and a "constrained" double pendulum. The process of developing and operating physical hybrid systems involves suitable feedback control mechanisms. Let us now take a brief overview on the development of hybrid dynamic systems and basics of feedback control.

1.1 Design-for-Validation

This is a design methodology wherein the mechanical system is designed such that it can be thoroughly tested. In order to measure all parameters that cannot be deduced from logical design, a detailed and precise reliability model would be

---

This thesis follows the style of *IEEE Transactions on Robotics*.

created for the system. During the design process, some tradeoffs are made to simplify the model by reducing the number of measureable parameters. This method allows analysis to ensure that there are no design flaws included in the reliability model [2]. Let us now look at the concept of functional modeling.

1.2 Functional Modeling

Clarity of function is vital to conceptual product design. Conceptual design revolves around *functional modeling* just as Computer-aided design (CAD) requires detailed geometric drawings to generate meaningful designs. Functional modeling

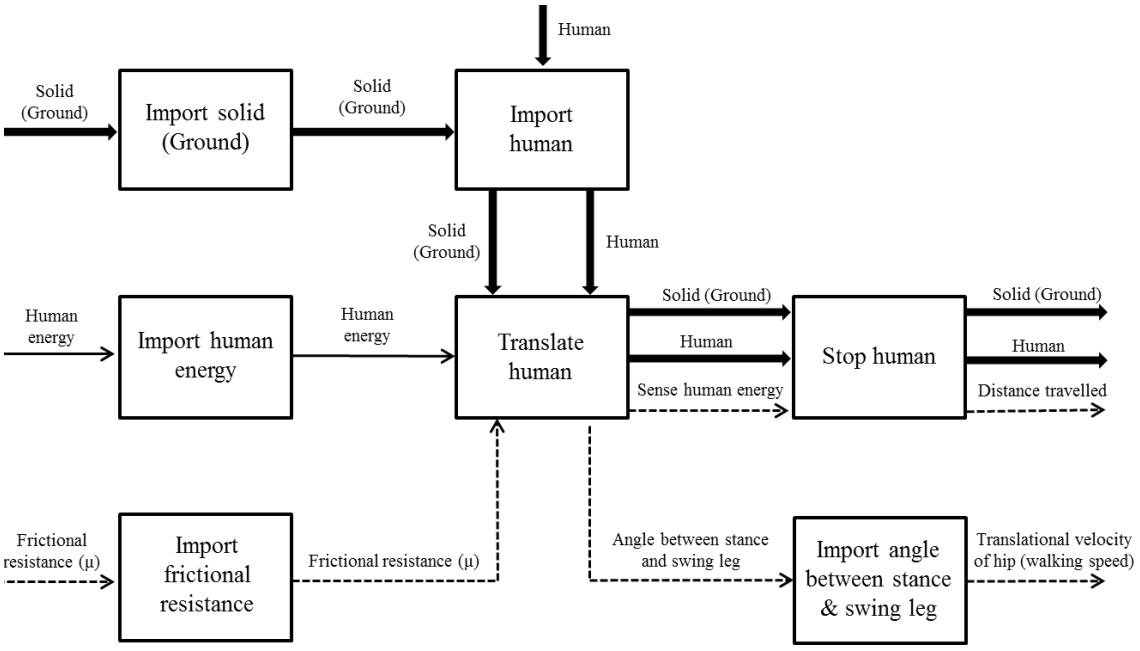

Figure 1: Simple functional model for the human "walking" function

simplifies a design problem by dividing it into solvable sub-problems. This allows us to obtain detailed information about each function as well as establish relationships between sub-functions. This results in the generation of the *functional model*, which allows us to verify the design and modify it if necessary [3]. This concept will be discussed in greater detail later as part of the design process. A simple functional model for the human "walking" function is illustrated in **Figure 1** (bold solid arrows signify material flow, normal solid arrows indicate energy flow and dashed arrows indicate the flow of information).

1.3 Hybrid Dynamical Systems

As explained by Newton's second law, continuous changes in velocities are observed in multi-body systems. However, instantaneous velocity and momentum changes are also observed in most dynamic systems due to impacts. Such systems which exhibit behaviors of both continuous-time and discrete-time systems can be considered as *hybrid dynamical systems* [4]. A bouncing ball (shown in **Figure 2**) is an example of a simple hybrid dynamic system.

1.3.1 Anthropomorphic Bipedal Walking Robot

Modeling a dynamic system such as a bipedal walking robot requires appropriate information on the walking gait and actuation mechanisms employed in conventional walkers. Primarily, we will understand the features of previously developed bipedal walkers by conducting an extensive literature review. Thereby, it will be possible to develop sufficient insight about the number of degrees of freedom (DOF), mass

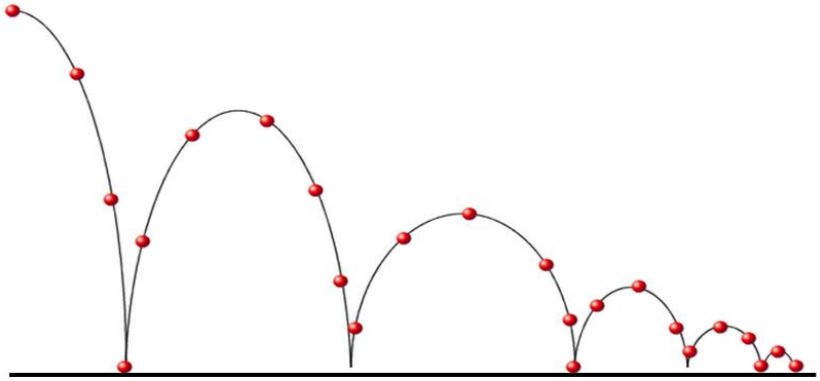

Figure 2: A bouncing ball is an example for a simple hybrid dynamic system

distribution and type of actuation required to model a anthropomorphic (or human-like) walking gait.

Researchers believe that legged robots have greater adaptability even in highly constrained environments. Also, anthropomorphic biped robots could work more efficiently on tasks involving maintenance and supervision due to the flexibility provided by their human walking gaits [5]. Due to the complicated nature of the bipedal walking robot in terms of the design and the control requirements, we will introduce a relatively simpler hybrid dynamic system: A "constrained" double pendulum model wherein the pendulum links are modeled similar to a human leg. Let us now look at the characteristics of this hybrid system.

1.3.2 Double Pendulum Model

The double pendulum model can be considered as a perfect case study that can provide for future research on biped robots. This system is proposed to consist of 2 rigid links of which only the top link can be actuated. The double pendulum model is treated as a Lagrangian hybrid system and will be designed with a mechanical stop which is

analogous to the human knee joint. As a result, it is possible to obtain a motion identical to human walking in this model.

We propose to implement *feedback PD control* for this model. The design and development of a physical setup of this model will be taken up in this thesis. The experiments performed on this setup form the basis for the results which will be analyzed in this thesis. We will attempt to establish the existence of *Zeno behavior* in the double pendulum model as well as achieve *Zeno periodic orbits* with the help of stable limit cycles and suitable phase portraits. We will introduce limit cycles and phase portraits in the following subsection. Zeno behavior and zeno periodic orbits will be discussed in greater technical detail in the later sections.

1.3.3 Limit Cycles and Phase Portraits

In a dynamical system, a *limit cycle* is defined as a closed trajectory which corresponds to a periodic solution of the system [6]. As time approaches infinity or negative infinity, one or more of the neighboring trajectories of the dynamical system tend to approach the limit cycle trajectory. If the neighboring trajectories of the dynamic system approach the limit cycle as time tends to infinity, then the limit cycle is defined to be *stable* or *attractive*. On the contrary, if the neighboring trajectories spiral towards the limit cycle as time approaches negative infinity, then the limit cycle is termed as *unstable* or *non-attractive*.

The trajectories of a dynamical system in a state space can be represented geometrically with the help of a *phase portrait*. These trajectories are known as phase curves, which essentially depict the solution of a set of equations of motion of the

dynamical system in the state space as a function of time. For a given system, the phase portrait varies with each set of initial conditions. The representation of the phase portrait graph of a typical dynamical system includes the system's trajectories (denoted by arrows), the stable steady states (illustrated by dots) and unstable steady states of the system (depicted by circles).

1.4 Feedback Control

As explained in Doyle et al. [7], the principle of *feedback control* requires that the controllable signal is compared with a desired reference signal and the difference is used to determine the appropriate control action.

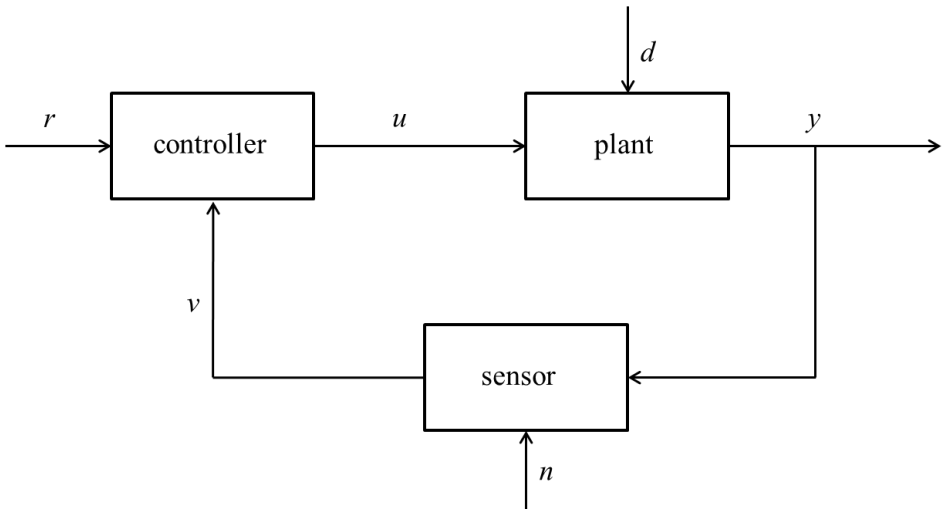

Figure 3: Building blocks of an elementary feedback control system [7]

As illustrated in the **Figure 3** [7], the elementary feedback control system consists of three components: a *plant* which is analogous to the controllable signal, a

sensor which can measure the output of the plant and a *controller* which modulates the plant's output. In the figure, r denotes the reference or command input, v is the sensor output, u is the actuating signal (plant input), d is an external disturbance, y is the measured signal (plant output) and n is the sensor noise.

2. LITERATURE REVIEW

The initial part of this literature review explains the systematic approach undertaken during the product design procedure. Also, several sources are explored in order to make suitable design decisions in creating the functional designs of the two hybrid systems considered. We will then move on to explain the theory of hybrid systems and feedback control as applied to a double pendulum model.

2.1 Approach to the Product Design Procedure

The degree of novelty in design varies for every product. Generally, any design can be classified into one of the three groups: original, adaptive or variant [1]. We try to propose *original* designs when new tasks and challenges need to tackled. In such designs, new solution principles are implemented although the technology is not necessarily firsthand. In case of *adaptive* designs, known solution principles are used. However, they are adapted according to the specific requirements of the product. *Variant* designs fundamentally use previously implemented product structures. Such designs only involve modifications in the geometry of certain components required for the specified product.

Making early decisions with conviction is crucial in engineering design. The initial stages of the design process are quite uncertain which renders quick decision making difficult. Also, the total cost of designing a model is roughly estimated during the preliminary stages of the design process. This indicates that imprecision is integral

to the design process [8]. However, this lack of clarity and imprecision in the initial design can be sorted out completely towards the end of the design process, with the exception of allowable dimensioning tolerances. This can be possible with a methodical design strategy which can be of assistance in generating an accurate model.

A systematic design approach helps structure the problem and design tasks. Also, the design and production methods can be justified better with such an approach. According to Pahl and Beitz [1], a *design methodology* should be applicable to design problems relevant to any specialist field. Simultaneously, it should allow the implementation of known design solutions to related tasks as well as encourage creativity.

Proper analysis and synthesis is necessary in solving complex design problems. The design procedure primarily involves four phases: *Product planning and clarifying the task, conceptual design, embodiment design* and *detail design* [1]. Let us discuss these vital steps in some detail in the following subsections.

2.1.1 Product Planning and Clarifying the Task

Product planning requires understanding and responding to the needs of the customer in an appropriate manner [1]. In case of mass production, the life cycle of each product is recognized depending on the type of product, the needs of the customer and the market situation. However, in case of a specific product, the precise functional requirements need to be met. After analyzing the nature of the product, search strategies are formulated by taking into account the market trends and needs. By identifying new product functions and working principles apart from the existing ones, the product ideas

are developed. A product idea is selected based on the available resources and goals to be attained. The functional requirements of the product are now described and formulated in a "solution-neutral" way.

While designing any product, the basic concept has to be developed based on the list of requirements, i.e., the design specifications. This forms an integral part of *clarifying the task*. At this point, solution fixation can be avoided by specifying only the required function with appropriate inputs and outputs and the task-specific constraints. The requirements list is vague and imprecise at this stage [9]. The next step in the design process (the *conceptual design* stage) is crucial to identifying the required technical specifications as well.

2.1.2 Conceptual Design

The necessity of the *conceptual design* stage is to obtain the solution principle for the desired product [1]. The essential functions for the design problem are identified and separated in order to establish suitable functional models. To satisfy these separate functions, suitable working principles are researched. The principles found during this search can be combined to form a working structure. However, these working principles are primarily aimed to satisfy the technical functions of the design which makes the model *qualitative*. To make it *quantitative*, certain general or task-specific constraints also need to be satisfied. According to Hubka [10], general constraints are categorized based on operational, ergonomic, aesthetic, distribution, delivery, planning, design, production and economic aspects. The theory behind *functional modeling* and building the *House of Quality (HOQ)* will be presented in further detail in following subsections.

2.1.2.1 Theory of Functional Modeling

Let us look into the theory underlying functional modeling. A mechanical system is divided into sub-systems such that a complex overall function can be broken down into *sub-functions* [11]. This simplifies the problem considerably. All the individual sub-functions are brought together to build a functional model which is a representation of the overall function.

A function is similar to a "black box" full of operations which are required to realize the objectives which are also known as sub-functions. The objective doesn't consider the performance level of the function. So, when the objectives to be achieved by the function are decided, the efficiency is not mentioned. Each of these objectives is a mission statement and does not include any information about the overall output of the function to be performed [11]. Each function is modified and represented in such a way that it can be associated with the actual physical model at the end of the design process. Proper anticipation, explanation and validation of the model are possible only with accurate knowledge of the functions to be performed [12]. Since the physical structure of the product is influenced by its functions, it is imperative that we have enough information about the behavior of the product. Deng et al. [3] have proposed the concept of Behavioral Scenario to explain how the working environment affects the product behavior.

In order to understand how each objective or sub function helps in obtaining the desired output and also to determine the efficiency level of each function, a House of

Quality (HOQ) diagram is created for the concerned model. The theory behind this concept will be considered in next subsection.

2.1.2.2 Quality Function Deployment (QFD) and Building the House of Quality (HOQ)

Ensuring the desired product quality is integral to the design process. Quality is vital during every phase of the design process and cannot be limited to the building and experimental stages. A quality policy is necessary to fulfill the product requirements. As explained during the planning stage, the initial requirements laid out are generally vague and need to be translated into clearly formatted and quantified requirements. This can be achieved using the *Quality Function Deployment (QFD)* approach [1].

The QFD approach was first introduced by Yoji Akao. According to Akao [13], Quality Function Deployment can be defined generally to be "the deployment of quality through deployment of quality functions". Thus, this approach is helpful in refining and completing the requirements list as well as improving the quality of the functions employed for the product.

Cross [9] summarizes the key steps to be followed as part of the QFD approach. First and foremost, the initial requirements need to be identified in terms of attributes of the product. The relative importance of the product attributes need to be established using techniques such as rank-ordering or points-allocation. In case of mass production, the attributes of competing products are compared with those of the current product based on the customer requirements. The effects of engineering characteristics on the product attributes need to be presented in terms of measurable units. Also, numbers or symbols can be used to express the relationship between engineering characteristics and product attributes. Finally, the target figures are to be fixed based on certain trial simulations.

The *House of Quality (HOQ)* is a tool defined as the complete set of tools required for quality assurance [1]. So, it is effectively a part of the QFD approach. A sample HOQ diagram is shown in **Figure 4**.

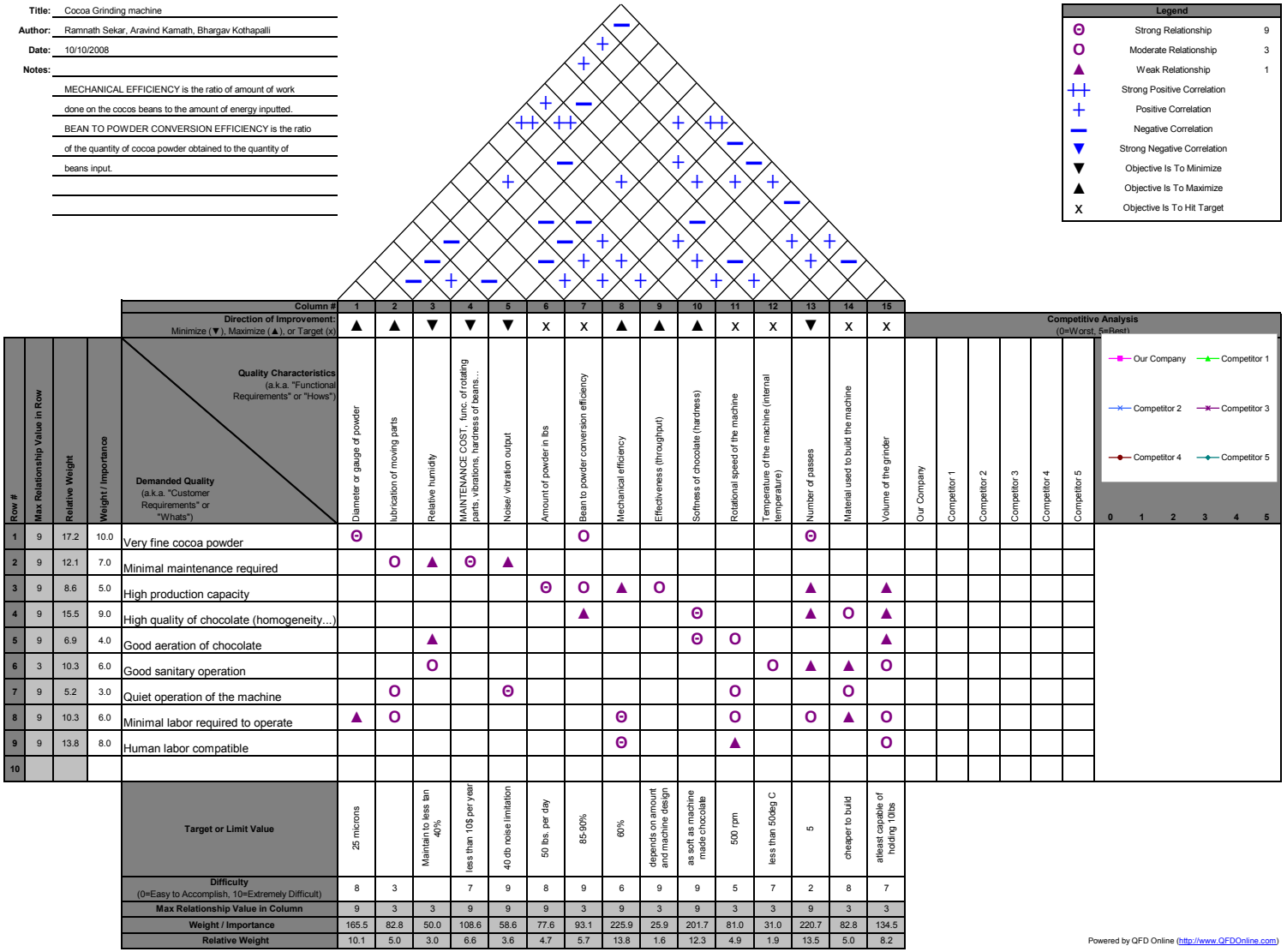

Figure 4: A sample House of Quality (HOQ) diagram

2.1.3 Embodiment Design

This stage of the design process is instrumental in determining the overall layout design, the preliminary form of the design, the production processes to be used and providing solutions for any secondary functions of the product [1, 9]. *Embodiment design* is a relatively difficult step in the design process. This is because it requires several corrective actions during which the search for solutions and their assessment should be carried out along with error identification and process optimization simultaneously. Also, any changes made to one area of the design would influence other areas too. The ultimate result expected out of this stage is a *definitive layout* wherein the product function, reliability, production, assembly, operation and costs involved can be verified beyond doubt. This stage comprises some crucial steps which are useful in proceeding from a qualitative to a quantitative standpoint as well as to allow for future verifications and corrections if needed. These steps will be discussed briefly in the following paragraphs.

There are three fundamental rules for embodiment design: fulfillment of the necessary technical functions, economic viability, personal and environmental safety. These are to be followed during every step of this design stage [1]. Initially, the requirements list is analyzed to identify the requirements which are influential to embodiment design. These include requirements pertaining to size, arrangement and material. Spatial restrictions are then determined by creating scale drawings of the product components. At this point, a rough layout is generated considering only the embodiment-determining assemblies and components which are necessary to carry out

the main functions of the product. Then, the preliminary layouts and form designs for these main function carriers must be produced with the necessary provisions for improvisation. Detailed layouts and form designs are then produced for the main function carriers while ensuring that compatibility with the secondary functions is addressed. Now, the important secondary functions (such as support, maintenance) are also identified. A similar procedure as narrated previously is followed to prepare detailed layouts and form designs for these functions.

At this point, the layouts prepared are evaluated for technical and economic feasibility [1]. The overall preliminary layout is now finalized and form designs for the corresponding layout are optimized and completed by eliminating any weak points which have been identified during the evaluation. After checking the layout design for any design faults in function and spatial constraints, the necessary improvements are made. The embodiment design phase is completed by making a preliminary parts list and preliminary production and assembly documents. Then the definitive layout design is decided and we can proceed to the *detail design* phase.

2.1.4 Detail Design

As described in Pahl and Beitz [1], during this phase of the design process, various key factors of the product such as the complete arrangement, geometry, forms and surface properties of all the individual parts are finalized. Additionally, the materials to be used are specified, production possibilities evaluated, costs estimated and all the part drawings and other production documents are prepared [9]. So, the ultimate result of the *detail design* phase is the *specification of production*.

Although this is the final stage of the design process, it is important to maintain proper attention to detail to avoid complications during the experimentation of the finished product. Certain improvements in the components and assemblies could also require that the previous design steps are repeated. However, this would not always mean that the final solution is altered considerably at this stage. The flow diagram shown in **Figure 5** [1, 9] gives a complete representation of the product design process.

This design phase involves the following important steps. The *definitive layout*, which consists of detailed drawings of individual components as well as the optimization of the forms, materials, surfaces and geometrical tolerances, is finalized. Then, the overall layout drawings, assembly drawings and parts lists are also integrated to ensure technical and economic viability. Finally, all the production documents which comprise production, assembly, transport and operating instructions for the product are completely prepared. It can be observed that each of the above steps influence each other.

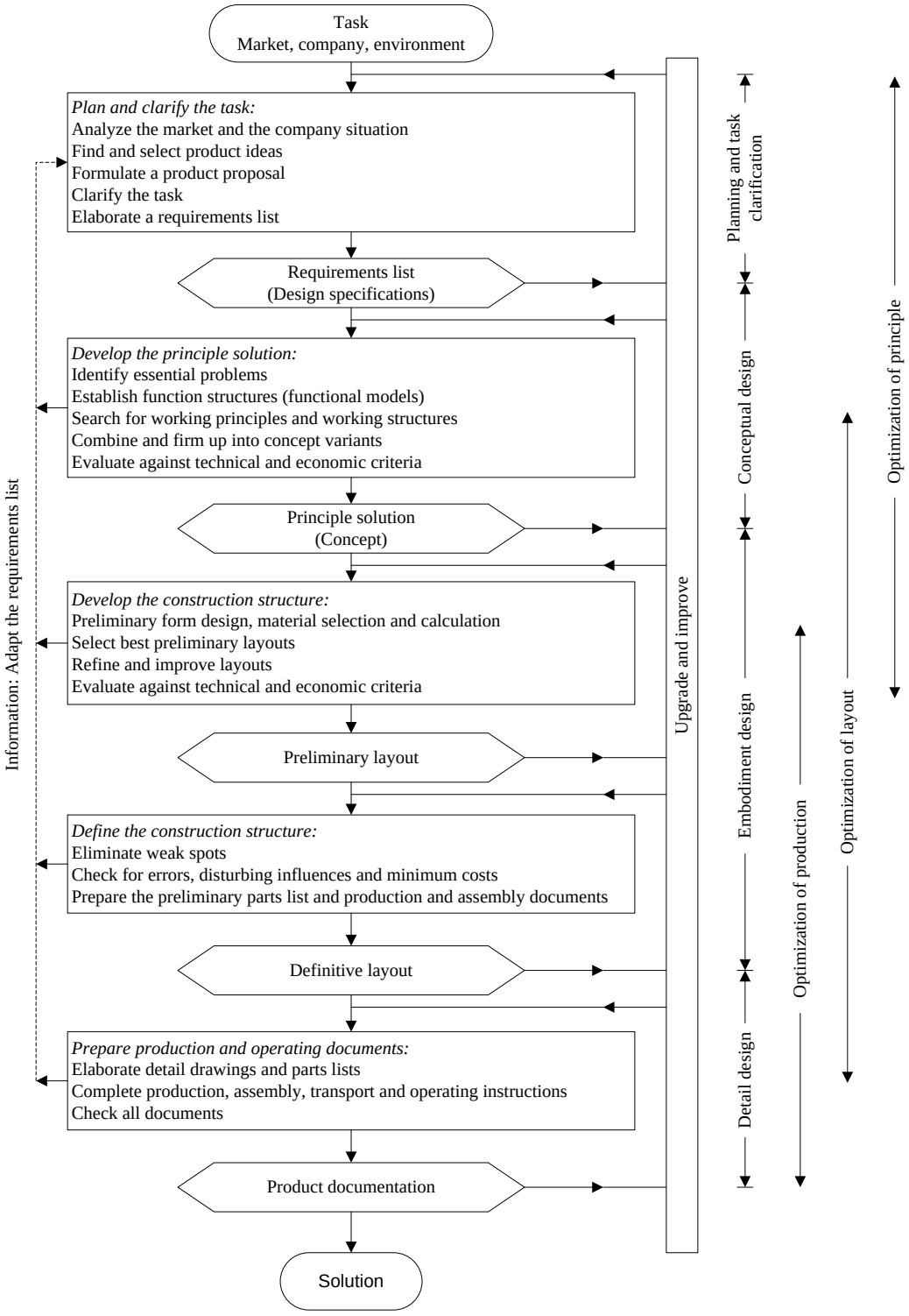

Figure 5: Pahl and Beitz [1] model of the design process

2.2 Theory of Bipedal Robot Locomotion

Legged robots are considered to adapt better to different types of ground and also move better in a highly constrained environment. Bipedal robots are a subclass of legged robots and an example of biomimetic design. The potential of using bipedal robots in various hazardous occupations as well as to design prosthetic devices gives ample motivation to pursue the design and control of bipedal robots [14]. However, designing a controller capable of generating closed-loop motions such as walking and running (with stable limit cycles) forms a major challenge in developing bipedal robots. Gait instability is another issue which has been observed even on level grounds [15]. Important aspects of designing an anthropomorphic bipedal robot will be discussed in the following subsections.

2.2.1 Fundamentals of Bipedal Robot Walking

First, let us look at some important terms to be understood in bipedal robot design. A biped is considered to be an "open kinematic chain" comprising two subchains which form the *legs* of the robot while an additional subchain, the *torso* is sometimes included. These are all connected at the *hip*. During the motion of walking or running, the leg which is in contact with the ground is referred to as the *stance leg* while the other is called the *swing leg* [14]. A sketch of the basic components comprising a bipedal robot is shown in **Figure 6**.

Three basic human reference planes are widely referred to while explaining bipedal robot locomotion, namely *sagittal*, *coronal* and *transverse* planes. The longitudinal plane that divides the body into right and left sections is known as the

sagittal plane. The *coronal plane*, also known as the frontal plane, is parallel to the long axis of the body and is perpendicular to the sagittal plane. This plane divides the body into anterior and posterior sections. The *transverse plane* is perpendicular to both the sagittal and coronal planes [16]. **Figure 7** [14] is an illustration of the human reference planes.

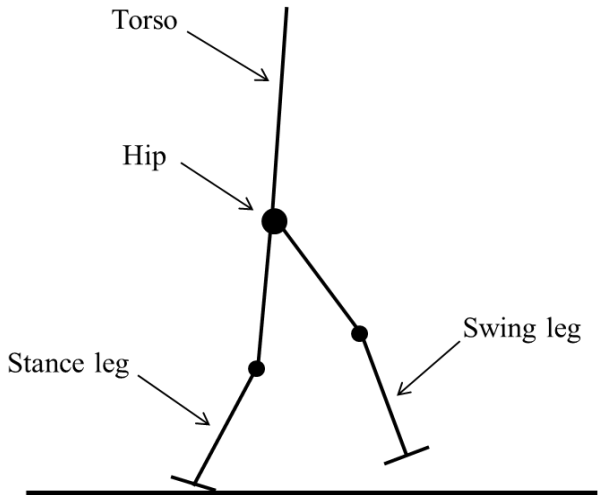

Figure 6: Sketch showing the basic components of a bipedal robot

2.2.2 Gait Modeling and Actuation Requirements

Human walking and bipedal robot walking are dynamically similar systems although human walking is far more complicated when compared to bipedal robot walking. However, bipedal robot locomotion can capture fundamental properties of human walking such as stability [17]. Let us now consider some bipedal robot models proposed in the past to understand the actuation methods implemented and their capabilities. In Grizzle et al. [18], a simple, planar biped robot has been considered to

explain walking stability. This "dynamic" robot model is designed to have a torso, hips, and two legs of equal length with no ankles and no knees. The masses of all the components are lumped as illustrated in **Figure 8** (along with its generalized coordinates). Effectively, this model has five degrees of freedom (DOF). Only two torque values are used for actuation between the torso and the legs for this model.

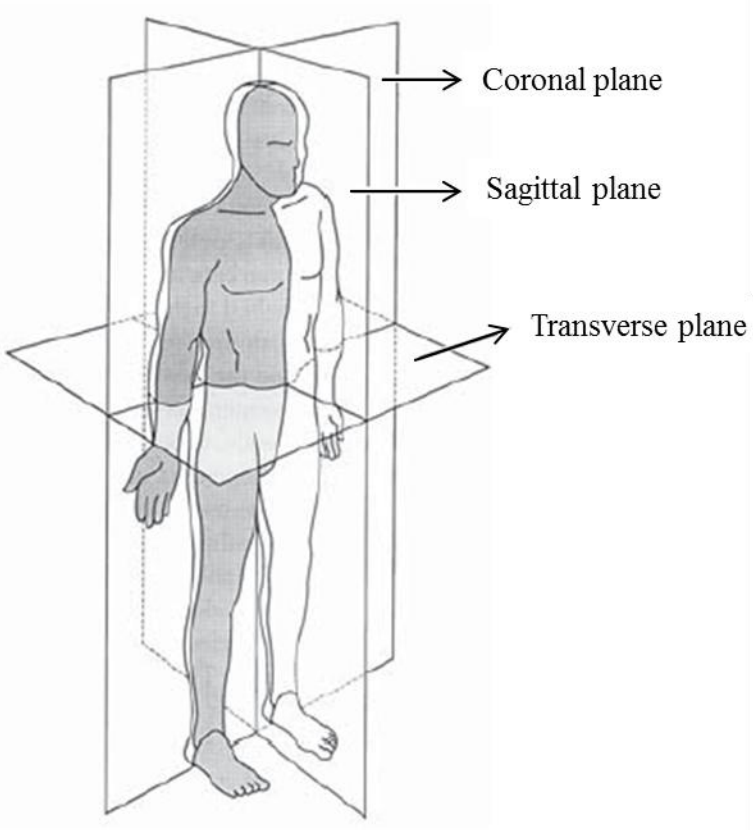

Figure 7: Basic human reference planes [14]

So, this is an under actuated model. The walking cycle for this robot occurs in the sagittal plane and on a level surface. While assuming that this walking cycle has

successive single support phases (one leg in contact with the ground), an infinitesimal amount of time is required for the switch to occur from one leg to the other. The mathematical model for bipedal robot locomotion will be discussed in detail in subsection 2.2.3.

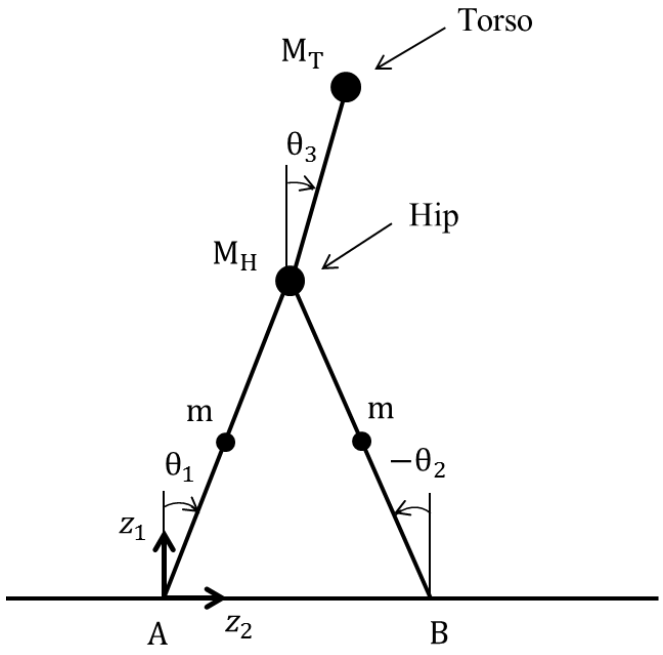

Figure 8: Planar dynamic bipedal robot model with 5 DOF, proposed by Grizzle et al. [18]

For the dynamic walking model described earlier, the stance leg is to be modeled as a pivot [18]. To avoid the possibility of *scuffing* (dragging the leg along the ground) until the intended moment of contact during the swing phase, the idea proposed by McGeer [19] can be implemented. This idea assumes that the swing leg switches from the sagittal plane (the plane of forward motion) into the coronal plane, thereby allowing a clearance between the leg and the ground. Also, the swing leg is assumed to re-enter

the sagittal plane when the stance leg is at a certain angular value (before it makes contact with the ground). This is achieved using retraction motors.

Adding knees to the aforementioned straight legged walking model is a significant advancement taken towards achieving a more anthropomorphic walking gait in biped robots. At the same time, knees present a more efficient way to avoid the problem of *scuffing* [20]. This is a "passive" walking model wherein four links make up the two legs for the model connected at the hip and a point mass attached at the hip represents the torso. The feet are designed to be semi-circular in shape. At the beginning of the first step, suitable speeds and angles are provided for this model to initiate walking along a shallow inclined plane as shown by the schematic drawing in **Figure 9**. The legs then swing passively along the slope till the point of heel strike in a perfectly natural style. During the swing phase, knee locking occurs before heel strike and both these collisions are assumed to be inelastic. These collisions result in a change in the link speeds and after heel strike, the speed comes down to the value given at the beginning of the first step. Cyclic motion can be consistently achieved in this manner for this model.

The two models described earlier do not exhibit lateral movement, i.e., the motion is purely in the sagittal plane. Kajita et al. [21] have proposed a purely "dynamic" bipedal walking robot consisting of 5 links and 4 DOF (**Figure 10**). This model consists of a pelvis and two legs with variable configurations. The pelvis is attached with two motors and speed-reducers. Also, it has passive feet which prevent the walker from falling. The total mass and height for this model is 2.5 kg and 0.4 m

respectively. The ratio of the mass of each leg to the total mass of this model is 18%. However, no lateral motion is exhibited by this model too.

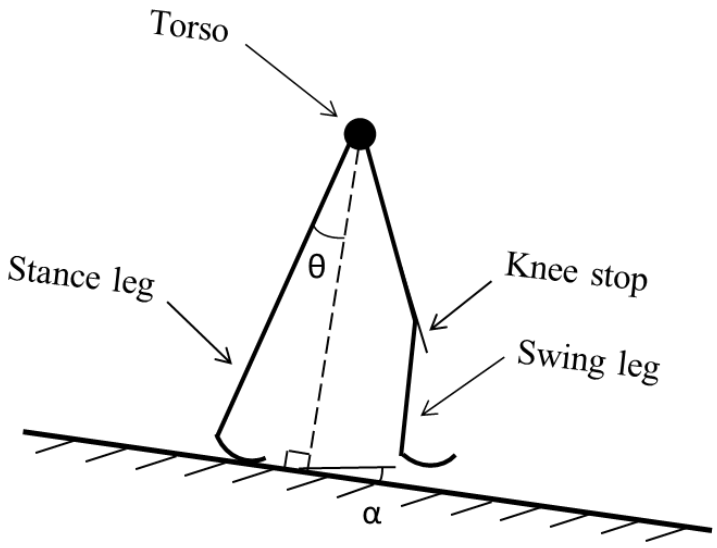

Figure 9: Passive walking model with knees (4 DOF) proposed by McGeer [20]

Miura et al. proposed another purely "dynamic" walking model named BIPER-3 consisting of a pelvis and two stiff legs connected at the hip. This model consists of 3 links and 4 DOF (**Figure 11** shows schematic drawings of the frontal and sagittal views). This model weighs 2 kg and has a height of 0.31 m respectively. The ratio of the mass of each leg to the total mass of this model is 32%. Lateral motion is facilitated in this model by providing a flexing-stretching freedom and an abduction-adduction (the movements of the legs pulling away from or coming together to the midline of the structure) freedom as explained in [22]. Lateral motion helps the robot in achieving lateral equilibrium during the single support phase and also prevents *scuffing*.

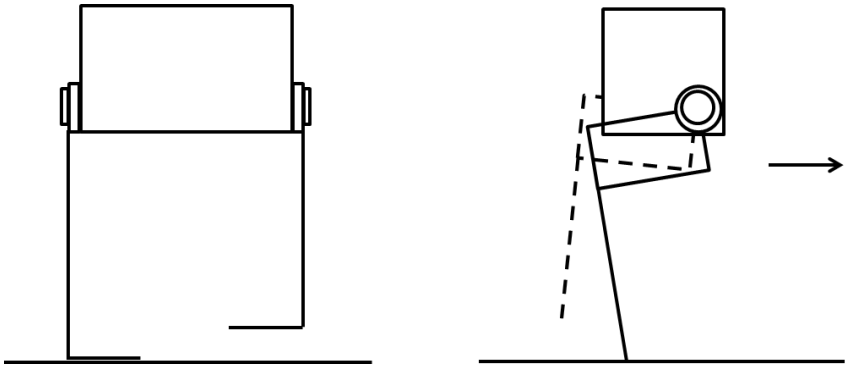

Figure 10: Purely "dynamic" biped model with 4 DOF, Kajita et al. [21]

Furusho et al. proposed another "dynamic" walking model with 8 DOF named BLR-G2 [23]. This model consists of a pelvis and two legs. The hip and knee joints have a single DOF each in flexing-stretching while the ankle joint comprises a flexing-

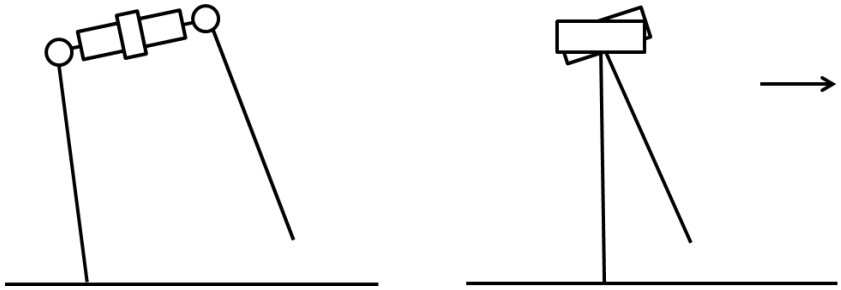

Figure 11: The purely "dynamic" model BIPER-3 with 4 DOF, Miura et al. [22]

stretching DOF as well as a DOF for lateral rotation. This model comprises a total of 7 links and 6 joints in the sagittal plane as shown in **Figure 12**. It weighs 25 kg and has a height of 1 m. The motors and speed reducers required for actuation are located on the pelvis and belts are used to transmit power to the joints. Due to these heavy components

attached to the pelvis, this model weighs 25 kg. It has a height of 1 m and the ratio of the mass of each leg to the total mass of the model is 30%. BLR-G2 is capable of walking in a straight line on level surfaces at a speed of 0.18 m/s.

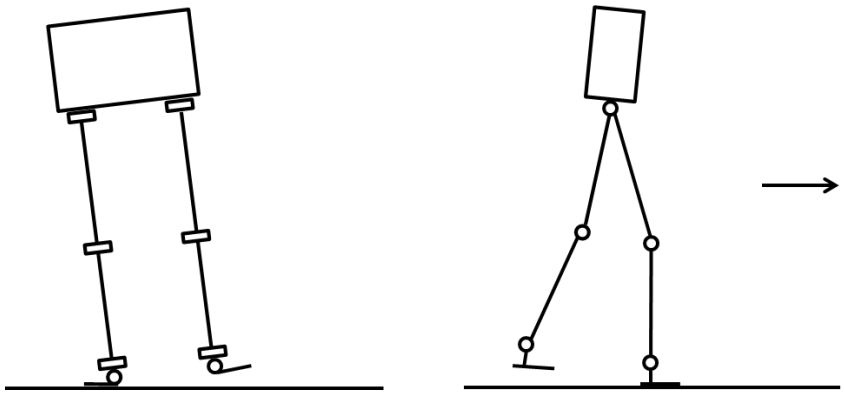

Figure 12: The dynamic walking model BLR-G2 with 8 DOF, Furusho et al. [23]

Another dynamic walking biped robot has been proposed by Gruver et al. [24] and it consists of a pelvis and two legs. This model has a total of 7 links and 12 DOF as shown in **Figure 13**. Each of the hips is provided with 3 DOF while each knee and ankle has 1 DOF and 2 DOF respectively. Lateral motion in this model is made possible by 5 links with 4 DOF while sagittal motion requires 7 links and 6 DOF. The remaining 2 DOF about the vertical direction are provided at the hips and assist the robot in changing directions when required. The actuation required for this model is provided by motors and geared speed-reducers which are placed in the axis of each joint. This model weighs 57 kg and is 0.92 m tall. The mass ratio of each leg to that of the entire model is

shown to be 37%. This model is capable of achieving considerable lateral movement. It moves in a straight line on level surfaces and can attain a speed of 0.71 m/s.

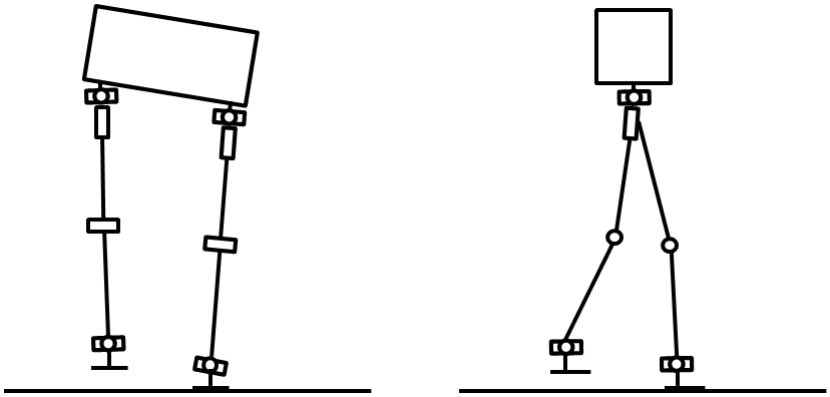

Figure 13: Dynamic walking model with 12 DOF, Gruver et al [24]

Let us consider another dynamic walking biped model named BIP. This is a joint project proposed and developed by Espiau [25] and Sardain et al. [5] named BIP . Of all the cases considered till this point, BIP has the closest anthropomorphic walking gait, mainly due to the 15 DOF provided. So, let us study this model in greater detail. According to the authors, the two major issues of concern during the single support phase are – passive lateral instability and impact at moment of heel-strike when the swing foot lands on the ground.

Sardain et al. [5] explains that the problem of lateral instability primarily deals with the time gap between the state of equilibrium and the state of imbalance due to the shift of the center of mass of the body. To understand the effect of this time gap, a simple problem of vertically balancing a stick on one finger is considered in this paper.

This experiment suggests that it is easier to adjust for lateral instability in case of a longer stick because the time gap between the equilibrium and unstable states is longer. However, this effect is verified mathematically by considering the biped to be standing on a single leg, thereby rendering it to be unstable. Denoting the initial angle between the center of mass *G* with the vertical axis as θ_0 and the final angle as θ_1 (shown in **Figure 14** [5]), the time gap between the two angular positions is found to be,

$$\Delta t \equiv t(\theta_1) - t(\theta_0) = \sqrt{\frac{1}{2mga}} \int_{\theta_0}^{\theta_1} \frac{d\theta}{\sqrt{\cos\theta_0 - \cos\theta_1}} \tag{1}$$

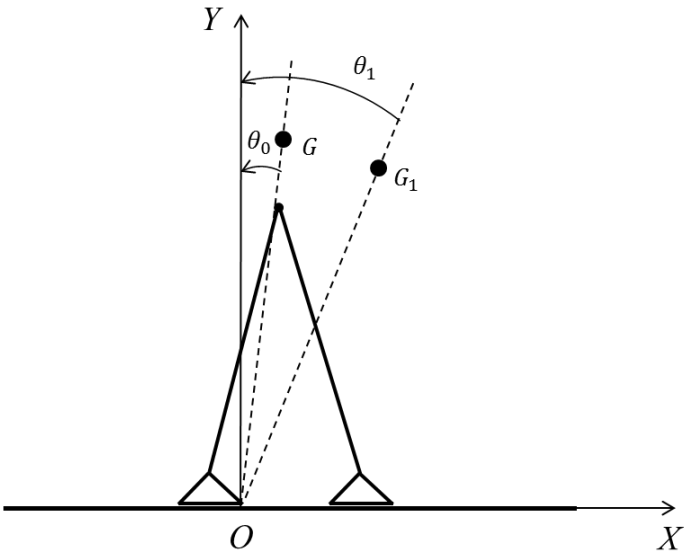

Figure 14: Lateral angular positions θ_0 and θ_1 of the center of mass of a biped for calculating the time gap during swing phase [5]

It needs to be ascertained whether the swing phase of the BIP virtually conserves the mechanical energy of the system. In the past, McMahon [26] studied the dynamics of the swing phase and suggested that the swing phase of human walking gait can be

considered as “ballistic”. This means that the double support phase possesses enough momentum to ensure continued motion during the single support phase. Also, it is identified that the mechanical energy of the biped does not vary much during the swing phase of walking. McGeer [20] also supported this observation using his idea of passive walking on an inclined plane. Also, McMahon remarked that the human walking gait during the swing phase to be similar to a double pendulum.

Sardain et al. takes inspiration from McMahon’s observations to form the basis for understanding the swing phase of bipedal robot locomotion. The initial and final constraint conditions as well as the corresponding optimization problem for the BIP have been defined in [5]. Also, it is determined that the distribution of mass along the leg affects the passive dynamic behavior of the robot. Pendular walking gait is more obvious when the concentration of mass is higher in the upper portion of the thigh or the calf (shin).

As mentioned earlier, the BIP has 15 DOF and 7 links consisting of one pelvis-trunk combination, two hips, two knees and 2 ankles. Schematic drawings of the sagittal and frontal views of the BIP are shown in **Figure 15** [5]. In order to facilitate the flexing-stretching motion, a total of 6 DOF (2 at the hips, 2 at the knees and 2 at the ankles) are provided. 5 DOF are added in the direction of walking of the model to ensure lateral equilibrium in the frontal plane. Also, a degree of freedom is provided between the pelvis and the trunk to provide flexibility between the two components during lateral movement. The actuators for this model were chosen based on the estimated values of torques and angular velocities required at each joint.

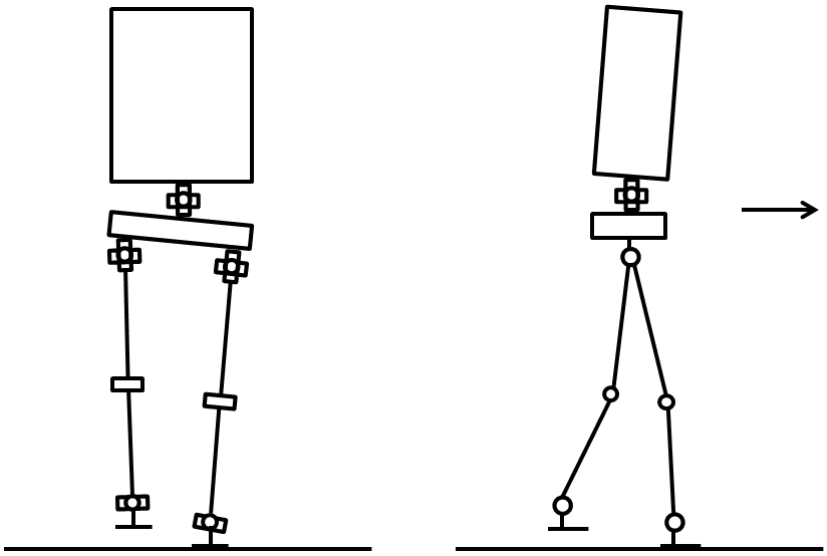

Figure 15: The Dynamic walking model BIP with 15 DOF, Sardain et al [5]

In order to provide a better idea of the actuation arrangements for each leg of the BIP, a left-side sectional view of the leg and a closer view of the actuation on the calf and ankle of the actual model have been shown in **Figure 16 (a)** and **(b)** respectively. It is made sure that the mass of the actuators is concentrated in the upper portion of each leg. This makes it easier to achieve controlled motion for the swing leg during the single support phase [5]. Also, all the motors and transmitters used for the model have their axes parallel to links, thereby reducing their inertia about the vertical axis. The two perpendicular rotations at the ankle joint were achieved by using special "motor screw-nut rod-crank" arrangements. The BIP weighs approximately 95 kg and has a height of 1.70 m. The ratio of the mass of each leg to the total mass of the model is found to be 18% while the corresponding parameter for the trunk (which weighs 42 kg without the pelvis) is about 44%.

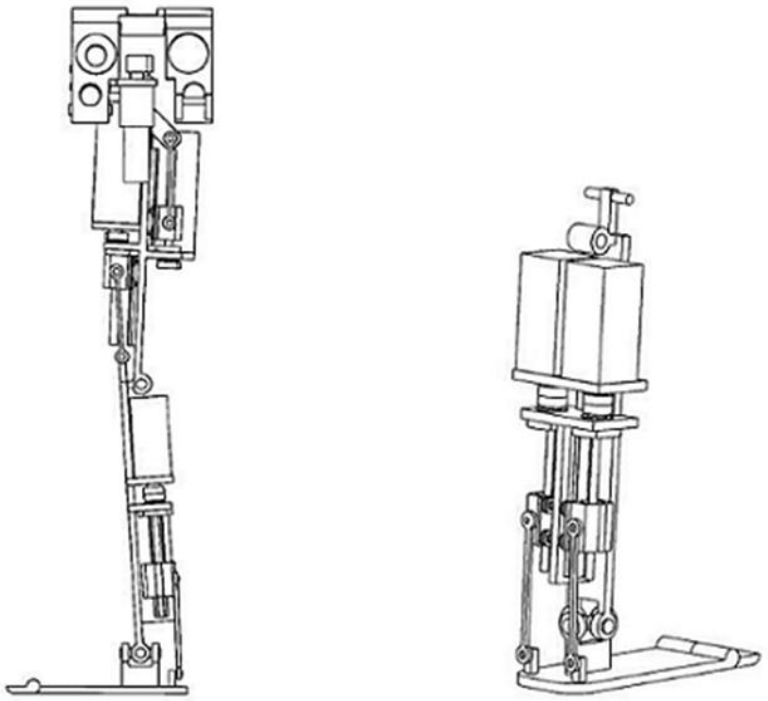

Figure 16: (a) Left-side sectional view of the leg of the BIP (b) Actuation arrangements provided for the calf (shin) and ankle [5]

2.2.3 Mathematical Model for Bipedal Robot Walking

Bipedal robots can be considered as hybrid dynamic systems due to the existence of continuous and discrete changes in velocity as well as unilateral constraints (resulting from the impact forces between the swing leg and the ground). So, Grizzle et al. [27] have considered a bipedal robot model with point feet (as shown in **Figure 17**) to develop the mathematical model. The robot is assumed to consist of *N* rigid links (where $N >= 2$). The links are assumed to be connected to each other by means of rigid and frictionless revolute joints. The total structure is assumed to be a kinematic chain in

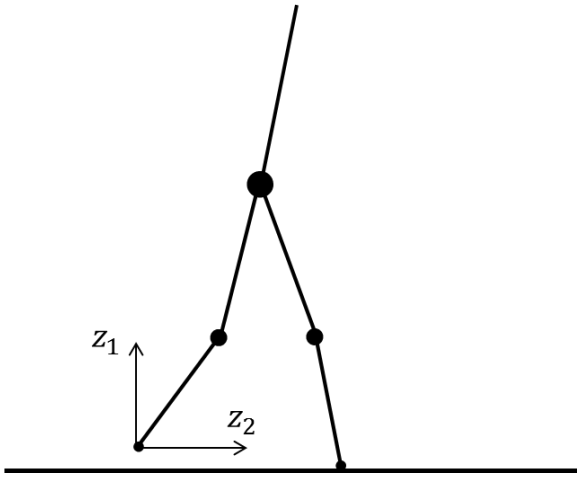

Figure 17: Typical planar bipedal robot with point feet [27]

a plane, consisting of 2 similar sub-chains (legs) connected to a third sub-chain (hip). It is assumed that motion occurs in the sagittal plane only and consists of successive *single support* (stance leg on the ground and swing leg in the air) and *double support* (both the legs on the ground) phases. An appropriate control system is designed to ensure that alternative contact of the legs with the ground occurs.

The mathematical model of bipedal robot walking consists of two parts: i) equations of motion to explain the swing phase dynamics and ii) an impact model for the contact event of the robot's leg with the ground. Grizzle et al. [27] have combined these two mathematical models to obtain a hybrid model. These will be explained in following subsections.

2.2.3.1 Dynamic Model of the Swing Phase

During this phase, it is assumed that the gait pattern is symmetrical. Considering the stance leg to be acting as a pivot and *Q* as the *n*-dimensional configuration manifold

for the robot, let $q := (q_1; ....; q_n) \in Q$ is a set of generalized coordinates and the potential and kinetic energies are $V(q)$ and $K(q, \dot{q}) = \frac{1}{2}\dot{q}'M(q)\dot{q}$ respectively. Here *M* is the (positive definite) inertial matrix. By using Lagrange's method, the dynamic model is obtained as [27],

$$M(q)\ddot{q} + C(q, \dot{q})\dot{q} + N(q) = B(q)u \tag{2}$$

Here, $C(q, \dot{q})$ denotes the vector combining the centripetal and Coriolis forces,

$N(q) = \frac{\partial V}{\partial q}(q)$, $u = (u_1; ....; u_{n-1}) \in \mathbb{R}^{(n-1)}$ where u_i is the torque applied between two links connected by a joint-*i*.

If $x(q, \dot{q})$ defines the state of the dynamic system, the above dynamic model can be presented in state space form as follows,

$$\dot{x} = \begin{bmatrix} \dot{q} \\ M^{-1}(q)[-C(q, \dot{q})\dot{q} - N(q) + B(q)u] \end{bmatrix} \tag{3}$$

$$=: f(x) + g(x)u \tag{4}$$

The state space of the model is defined as $\chi = TQ$. For each $x \in \chi$, *g(x)* is a (*2n)* x *(n-1)* matrix and its *i*-th column is denoted by g_i.

2.2.3.2 Impact Model

To explain the impact model, Grizzle et al. have considered the bipedal robot model presented in [24] as this model involves a perfectly inelastic impact of the swing leg with the ground. This model has been illustrated earlier in **Figure 13**. In this model, each impact is collapsed to an instant in time and is represented by an impulse. Every impact results in a disturbance in the velocity component of the robot's motion. Also,

by assuming a symmetric walking gait, two impact models (one for each leg during its corresponding swing phase) can be avoided. This is made possible by *relabeling* the generalized coordinates for each leg when the roles of the legs switch alternatively.

A matrix denoted by *R* is used to represent the relabeling of the generalized coordinates. Also, *R* is a circular matrix acting on *q*, i.e., *RR* = *I*. The impact at the end of the swing phase and the relabeling of states results in the expression,

$$x^+ = \Delta(x^-) \tag{5}$$

Here $x^+ := (q^+; \dot{q}^+)$ is the state value immediately after impact while $x^- := (q^-; \dot{q}^-)$ is the state value just before impact. Also,

$$\Delta(x^-) := \begin{bmatrix} \Delta_q q^- \\ \Delta_q(q^-)\dot{q}^- \end{bmatrix} \tag{6}$$

The hybrid zero dynamics of the swing phase are presented in greater detail in [28].

2.2.3.3 Overall Hybrid Model

The hybrid model for walking can be obtained by combining both the swing phase model and the impact model. If the trajectories of the swing phase model are assumed to have finite left and right limits denoted by $x^-(t) := \lim_{\tau \to t} x(\tau)$ and $x^+(t) := \lim_{\tau \to t} x(\tau)$ respectively, the hybrid model is given by,

$$\Sigma : \begin{cases} \dot{x} = f(x) + g(x)u, x^- \notin S \\ x^+ = \Delta(x^-), x^- \notin S \end{cases} \tag{7}$$

where *S* is the switching set represented as,

$$S := \{(q, \dot{q}) \in TQ \mid z_1(q) = 0, z_2(q) > 0\} \tag{8}$$

So, it can be said that the hybrid model trajectory is governed by the swing phase model until an impact occurs. The set *S* represents a walking surface and impacts occur when the state value "attains" this set [27]. The final result of the impact model is a new initial condition from which the next swing phase model starts and progresses until the next impact.

2.3 Hybrid Dynamical Systems and Understanding of Zeno Equilibria

Dynamical systems which exhibit both continuous-time and discrete-time dynamic behavior are known as hybrid dynamical systems [4]. Hybrid systems are capable of modeling a wide range of phenomena and this results in their increased complexity [29]. The next subsection provides a brief theory on hybrid dynamical systems. In the later subsections, we introduce the concept of Zeno behavior and Zeno periodic orbits in Lagrangian hybrid systems. Also, we discuss an example of a Lagrangian hybrid system, namely a constrained double pendulum model (as explained in Or and Ames [30]) in order to understand how Zeno behavior affects such systems.

2.3.1 Theory of Hybrid Dynamical Systems

In hybrid dynamical systems, a state is continuous for a certain amount of time while jumps are observed at other times. Due to this reason, any hybrid dynamical system is generally represented by two functions *f* and *g,* and two sets *C* and *D* [31]. The function *f* is used to specify variables that are continuous while function *g* is used to specify variable that exhibit jumps. The state space where continuous variables may

occur is represented by the set *C* while the set *D* denotes the state space where jumps may occur.

A typical hybrid system can be represented by a tuple $\boldsymbol{H}$ = (*D, G, R, f*) where *D* represents a smooth manifold also called the *domain*, *G* is an embedded submanifold also known as the *guard*, *R* is known as the *reset map* ($R : G \to D$) and *f* is a *vector field* on the domain *D*. Similarly, a simple *Lagrangian* hybrid system is represented by the tuple **L** = (*Q, L, h*) where *Q* denotes the *configuration space* (this is assumed to be identical to $\mathbb{R}^n$), *L* is a *hyperregular Lagrangian* ($L : TQ \to \mathbb{R}$) and *h* provides a *unilateral constraint* ($h : Q \to \mathbb{R}$) in the configuration space [30]. The Lagrangian *L* describes the mechanical system and can be represented as,

$$L(q, \dot{q}) = \frac{1}{2} \dot{q}^T M(q) \dot{q} - V(q) \tag{9}$$

where *M* (*q*) is the positive definite inertial matrix, $\frac{1}{2} \dot{q}^T M(q) \dot{q}$ is the kinetic energy and *V*(*q*) is the potential energy of the system. By using the Euler-Lagrangian method, the unconstrained equations of motion of the system [32] can be obtained as,

$$M(q)\ddot{q} + C(q, \dot{q}) + N(q) = 0 \tag{10}$$

The terms of equation (10) are similarly defined as those in equation (2). If we consider a *control law* $u(q, \dot{q})$ such that $u : \mathbb{R}^n \to \mathbb{R}$ is a smooth function, the equations of motion for the unconstrained and controlled mechanical system [30] can be expressed as,

$$M(q)\ddot{q} + C(q, \dot{q}) + N(q) = u(q, \dot{q}) \tag{11}$$

Considering $x = (q, \dot{q})$ as the state of the system, the Lagrangian vector field associated with *L* is given by,

$$\dot{x} = f_L = \begin{bmatrix} \dot{q} \\ M(q)^{-1}(-C(q,\dot{q}) - N(q) + u(q,\dot{q})) \end{bmatrix} \tag{12}$$

According to Or and Ames [30], the Lagrangian hybrid system related to the tuple **L** is a simple hybrid system defined as $\boldsymbol{H}_{\mathbf{L}} = (D_{\mathbf{L}}, G_{\mathbf{L}}, R_{\mathbf{L}}, f_{\mathbf{L}})$. Here,

$$D_{\mathbf{L}} = \{(q,\dot{q}) \in TQ : h(q) \geq 0\} \tag{13}$$

$$G_{\mathbf{L}} = \{(q,\dot{q}) \in TQ : h(q) = 0 \text{ and } dh(q)\dot{q} \leq 0\} \tag{14}$$

In equation (14), $dh(q) = \left[\frac{\partial h}{\partial q}(q)\right]^T = \left[\frac{\partial h}{\partial q_1}(q) \ldots \frac{\partial h}{\partial q_n}(q)\right]$. The reset map equation is given by $R_{\mathbf{L}}(q,\dot{q}) = (q, P_{\mathbf{L}}(q,\dot{q}))$. The *impact equation* for the hybrid system can be derived as,

$$P_{\mathbf{L}}(q,\dot{q}) = \dot{q} - (1+e)\frac{dh(q)\dot{q}}{dh(q)M(q)^{-1}dh(q)^T} M(q)^{-1} dh(q)^T \tag{15}$$

In equation (15), *e* is known as the *coefficient of restitution* and it can vary between 0 and 1. The value of *e* is an indicator of the energy dissipation occurring at impact. The

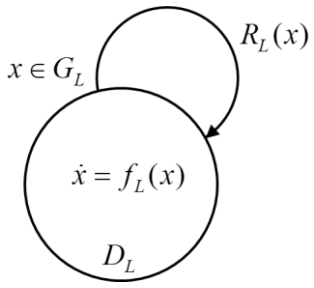

Figure 18: Graphical representation of a simple hybrid system

Lagrangian vector field associated with **L** is $f_{\mathbf{L}} = f_L$ associated with the Lagrangian L. A graphical representation of a simple hybrid system is shown in **Figure 18**.

If $D_{\mathbf{L}}$ is considered to be a holonomically constrained hybrid system associated with the hybrid Lagrangian **L**, the equations of motion for the constrained system can be obtained from the equation (11) which provided the equations for an unconstrained dynamic system [30]. The constrained equations of motion are as follows,

$$M(q)\ddot{q} + C(q,\dot{q}) + N(q) = dh(q)^T \lambda + u(q,\dot{q}) \tag{16}$$

where λ is the Lagrange multiplier and represents the contact force. In the following subsection, we will discuss Zeno behavior and the sufficient conditions necessary for its existence.

2.3.2 Explanation of Zeno Behavior in Lagrangian Hybrid Systems

Zeno behavior (also known as chattering) is a unique characteristic of hybrid dynamical systems. This behavior comprises an infinite number of impacts or discrete transitions taking place in a finite amount of time. A bouncing ball is a traditional example of Zeno behavior and is considered to be in the class of Lagrangian hybrid systems. Till recently, Zeno behavior had remained largely unexplored. However, sufficient conditions for the occurrence of Zeno have been laid down in various works for different classes of hybrid systems from a mathematical perspective. Heymann et al. [33] have explained the conditions for existence of Zeno in constant-rate and regular hybrid systems while Ames et al. [34] have considered diagonal first quadrant (DFQ) hybrid systems. Also, Ames et al. [35] have explained the requirements for existence of Zeno in non-linear hybrid systems. Lamperski and Ames [36] have explained the

conditions for Zeno existence in case of Lagrangian hybrid systems, i.e., hybrid dynamical systems involving impacts.

According to [29], the existence of Zeno behavior indicates that a type of convergence set can be obtained for the dynamic system considered. This convergence set is also known as *Zeno equilibria*. Lamperski and Ames [36] also suggest that Zeno equilibria are subsets of continuous domains of a hybrid system that are fixed points of discrete dynamics but not continuous dynamics. In the following subsection, we will define Zeno behavior and present the sufficient conditions for existence of Zeno in Lagrangian hybrid systems.

2.3.2.1 Sufficient Conditions for Existence of Zeno in Lagrangian Hybrid Systems

A hybrid execution χ^H is considered to be Zeno when $\Lambda = \mathbb{N}$ and $\lim_{i\to\infty} t_i = t_\infty < \infty$. Here Λ is an indexing set while t_∞ is called the *Zeno time*. If χ^{H_L} is a Zeno execution of a Lagrangian hybrid system $\boldsymbol{H}_\mathbf{L}$, then the *Zeno point* is defined as in [32],

$$c_\infty = (q_\infty, \dot{q}_\infty) = \lim_{i\to\infty} c_i(t_i) = \lim_{i\to\infty} (q_i(t_i), \dot{q}_i(t_i)) \tag{17}$$

These limit points are intricately related to unique type of equilibrium points relevant to hybrid systems – Zeno equilibria.

Now let us understand how Zeno equilibria are characterized for Lagrangian hybrid systems. If $\boldsymbol{H}_\mathbf{L}$ is considered as the Lagrangian hybrid system, it is found that the Zeno equilibria are represented by the point $z = \{(\theta^*, \dot{\theta}^*)\}$ if $\dot{\theta}^* = P(\theta^*, \dot{\theta}^*)$. Here impact equation P is obtained from equation (15) by substituting q with θ,

$$P = (\theta, \dot{\theta}) = \dot{\theta} - (1+e)\frac{dh(\theta)\dot{\theta}}{dh(\theta)M(\theta)^{-1}dh(\theta)^{T}} M(\theta)^{-1}dh(\theta)^{T} \tag{18}$$

This special form of *P* holds if $dh(\theta^*)\dot{\theta}^* = 0$. So the set of all Zeno equilibria for Lagrangian hybrid systems is given as,

$$Z = \left\{(\theta, \dot{\theta}) \in G_h : dh(\theta)\dot{\theta} = 0\right\} \tag{19}$$

Here G_h can be obtained from equation (14) while substituting *q* with θ,

$$G_h = \left\{(\theta, \dot{\theta}) \in TQ : h(\theta) = 0,\ dh(\theta)\dot{\theta} \le 0\right\} \tag{20}$$

The following theorem explains the sufficient conditions for existence of Zeno in Lagrangian hybrid systems.

Theorem 1: *Considering* $\mathbf{H_L}$ *to be a Lagrangian hybrid system,* $z = \{(\theta^*, \dot{\theta}^*)\}$ *to be a Zeno equilibria for* $\mathbf{H_L}$*, if 0 < e < 1 and*

$$\ddot{h}(\theta^*, \dot{\theta}^*) = (\dot{\theta}^*)^T H(h(\theta^*))\dot{\theta}^* + dh(\theta^*)M(\theta^*)^{-1}(-C(\theta^*, \dot{\theta}^*)\dot{\theta}^* - N(\theta^*)) < 0 \tag{21}$$

where $H(h(\theta^*))$ *is the Hessian of h at* θ^**, there is a neighborhood* $W \subset D_h$ *of* $(\theta^*, \dot{\theta}^*)$ *such that for every* $(\theta^*, \dot{\theta}^*) \in W$*, there exists a unique Zeno execution* χ *of* $\mathbf{H_L}$ *with* $c_0(\tau_0) = (\theta^*, \dot{\theta}^*)$.

Based on the set of Zeno equilibria presented in equation (19) and the above theorem, two different examples of Lagrangian hybrid system models, (*a ball bouncing on a sinusoidal surface* and *a pendulum on a cart*) have been analyzed in [36] to demonstrate that for every Zeno equilibria of these systems, there exists a neighborhood such that every execution with an initial condition within that neighborhood is Zeno.

2.3.3 Introduction of the Double Pendulum Problem

As mentioned earlier, Or and Ames [30] have simulated Zeno behavior by implementing the theoretical results on a constrained double pendulum model. This model consists of two rigid links with uniform mass distribution, which are attached by revolute joints. The masses of the top and bottom links are m_1, m_2 respectively while their corresponding lengths are L_1 and L_2. A mechanical stop is used to restrict the swing motion of the bottom link. A torque u_1 is provided to actuate the upper joint while the lower joint is passive. A sketch of this model is shown in **Figure 19**.

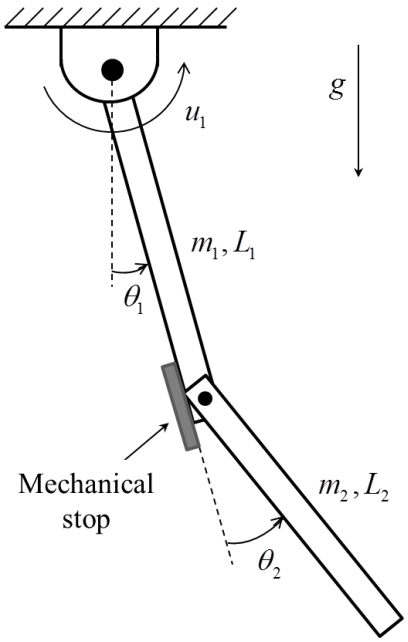

Figure 19: Sketch of the constrained double pendulum model [30]

The constrained double pendulum model resembles a passive knee with a knee stop. The basic configuration of this system is given by $q = (\theta_1, \theta_2)$ while the

mechanical stop represents a constraint $h(q) = \theta_2 \geq 0$. The Lagrangian of this dynamical system is given by,

$$L(q, \dot{q}) = \tfrac{1}{2} \dot{q}^T M(q) \dot{q} + (\tfrac{1}{2} m_1 L_1 + m_2 L_1) g \cos\theta_1 + \tfrac{1}{2} m_2 L_2 g \cos(\theta_1 + \theta_2) \quad (22)$$

and the elements of the 2x2 inertia matrix $M(q)$ are expressed as,

$M_{11} = \tfrac{1}{3} m_1 L_1^2 + m_2 (L_1^2 + \tfrac{1}{3} L_2^2 + L_1 L_2 \cos\theta_2)$, $M_{12} = M_{21} = \tfrac{1}{6} m_2 (3 L_1 L_2 \cos\theta_2 + 2 L_2^2)$, $M_{22} = \tfrac{1}{3} m_2 L_2^2$. For the purpose of simulations, the values of all parameters had been chosen as $m_1 = m_2 = L_1 = L_2 = g = 1$ by Or and Ames [30].

The initial conditions chosen for the simulations are $q(0) = (-0.08, 0)$ and $\dot{q}(0) = (0, 0)$. Initially, the *uncontrolled* swing motion of the double pendulum is determined under *plastic collisions* at the mechanical stop, i.e., torque $u_1 = 0$ and coefficient of restitution at the mechanical stop, $e = 0$. In this simulation, two plastic collisions are observed per cycle and the double pendulum displays a slightly decaying periodic-like motion (the reader is advised to refer to [30] to view the plots generated during simulation). It is also observed that immediately after the first plastic collision, the force λ necessary to maintain the constraint $\theta_2 = 0$ is negative. As a result, the bottom link goes into unconstrained motion momentarily before the second plastic collision occurs. After this collision, the constrained phase of motion is observed as the bottom link locks, i.e., $\theta_2 = 0$ is achieved and the constraint force becomes positive ($\lambda > 0$).

Or and Ames have also simulated the controlled motion of the double pendulum model with *non-plastic impacts* by using feedback PD (proportional-derivative) control.

The PD control law for certain torque u_1 is given by, $u_1(\theta_1, \dot{\theta}_1) = -K_p(\theta_1 - \theta_{1e}) - K_d\dot{\theta}_1$. The control parameters have been chosen as follows: proportional constant, $K_p = 0.5$, $\theta_{1e} = \pi/9$ and derivative constant, $K_d = -0.01$. The sketch of the basic feedback control loop has been shown earlier in **Figure 3**. The processes of designing a control system and establishing control objectives to obtain the desired output have been well documented in several works such as [7, 14, 37].

In the latter part of this thesis, we will discuss the development and experimentation of a physical model of the double pendulum problem considered by Or and Ames. The objective of the experiments on the physical model is to expand the results presented for point masses in [30] to a real-time environment comprising real masses. We will attempt to observe Zeno behavior and achieve Zeno periodic orbits in the practical model of this hybrid system by introducing non-plastic impacts of varying degrees. The mathematical model considered by Or and Ames will be used as the basis for determining the simulation results for the current double pendulum problem in Section 5 of this thesis.

3. RESEARCH APPROACH: DESIGN OF THE BIPEDAL WALKING ROBOT

In Section 2, the product design methodology and the theory behind the locomotion of bipedal walking robots have been explored in detail. Now, we proceed to focus on my research approach. This section explains the first part of the approach. This includes the process of designing an anthropomorphic bipedal walking robot while applying the previously explained design concepts.

3.1 Initiation of the Design Procedure

While designing the bipedal walking robot model, we implement the "*design by function*" approach. This approach calls for identification of all the functions needed to be performed by the product (in this case, the bipedal robot), based on which appropriate design decisions can be made.

Firstly, we identify the basic functions involved in human walking. As discussed previously, the walking motion in human beings occurs in the *sagittal, coronal* and *transverse* planes. The pelvis, hip bones and legs are the key body parts required to achieve walking. Based on these facts and past research, we have determined that all the functions of walking can be performed successfully with the help of 7 connected links. These include 1 link which serves as a pelvis (which includes the hip bones), 2 links acting as thigh bones (femurs), 2 as shin bones (tibia) and 2 as feet. Also, it is proposed that a total of 10 degrees of freedom are provided for this model. The mass distribution data of an average human being are used to determine the proportional masses of the

links which are used to build the robot. The basic functions of walking have to be replicated as closely as possible in our proposed walking robot model to ensure that it is anthropomorphic (human-like).

Based on these product requirements, we have created a House of Quality (HOQ) diagram where the following factors are focused upon – *product fidelity with the real system, repeatability of walking motion, speed of walking to be achieved* (this is dependent on the robustness of control law)*, reliability, ergonomics, biocompatibility* and *cost of production*. In the HOQ diagram shown in **Figure 20**, the requirements of the product are enlisted as quality characteristics and the level of importance as well as quality targets for each of each characteristic are identified. This simplifies the design problem to a great extent. Let us now look into the computer-aided modeling of our bipedal walking robot model.

Title: Design of a Bipedal Robot
Author: Bhargav Kothapalli
Date:
Notes: The simplicity of the product could determine how aesthetically appealing the product could be. However this may not always be the case.

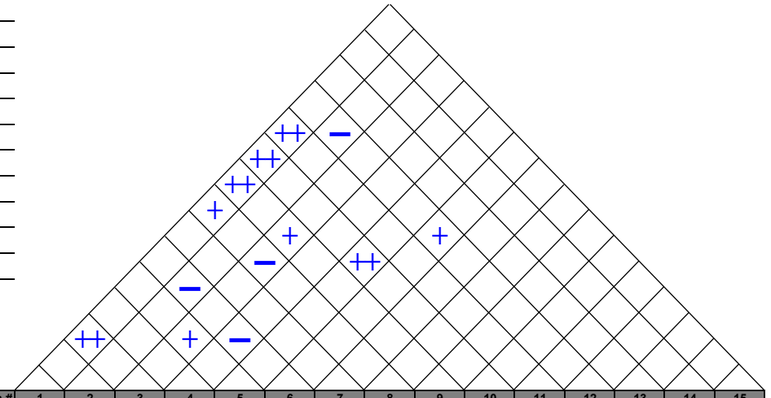

Legend		
⊙	Strong Relationship	9
O	Moderate Relationship	3
▲	Weak Relationship	1
++	Strong Positive Correlation	
+	Positive Correlation	
−	Negative Correlation	
▼	Strong Negative Correlation	
▼	Objective Is To Minimize	
▲	Objective Is To Maximize	
X	Objective Is To Hit Target	

Column #		1	2	3	4	5	6	7	8	9	10	11	12	13	14	15
Direction of Improvement: Minimize (▼), Maximize (▲), or Target (x)			x		x		▼	▲	▼	x	x	▲	▲			
Row #	Demanded Quality (a.k.a. "Customer Requirements" or "Whats")	Product fidelity when compared with the real system	Life cycle of the Biped	Ergonomics	Typical achievable speed of walking	Load bearing capability of each leg	Noise / vibration level	Biocompatibility of material used	Cost of production and maintenance	Customized anthropomorphic height	Anthropomorphic mass	Repeatability / consistency of motion of biped	Processing speed			
1	What is the cost of the product?	⊙							⊙				⊙			
2	What is its reliability?	⊙	⊙	O									▲			
3	Durability		⊙		▲	⊙		⊙	O							
4	What is the comfort level during usage?			⊙			O				O					
5	Ease in using the controls			⊙							O					
6	Is it a customized product or one type fits all?					⊙				O						
7	Attractiveness								▲							
8	How fast is it?		O		⊙							⊙	⊙			
9																
10																

Row #	Max Relationship Value in Row	Relative Weight	Weight / Importance
1	9	12.6	8.5
2	9	11.9	8.0
3	9	13.3	9.0
4	9	13.3	9.0
5	9	13.3	9.0
6	9	11.9	8.0
7	1	10.4	7.0
8	9	13.3	9.0
9			
10			

Competitive Analysis (0=Worst, 5=Best)	Our Company	Competitor 1	Competitor 2	Competitor 3	Competitor 4	Competitor 5

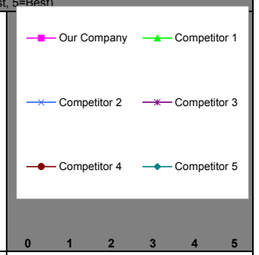

	Target or Limit Value	Closest to human movement	20 hours		Close to avg. human speed =		Not moe than 30-40 decibels	Eco-friendly in agreement with standard	No estimate decided	Typical person height = 167 cm	For avg. human = 63.5 kg	Around 20 minutes per cycle				
	Difficulty (0=Easy to Accomplish, 10=Extremely Difficult)	10				8	8	8	9	8	8	10	9			
	Max Relationship Value in Column	9	9	9	9	9	3	9	9	3	3	9	9			
	Weight / Importance	220.0	266.7	275.6	133.3	226.7	40.0	120.0	163.7	35.6	80.0	120.0	245.2			
	Relative Weight	11.4	13.8	14.3	6.9	11.8	2.1	6.2	8.5	1.8	4.2	6.2	12.7			

Powered by QFD Online (http://www.QFDOnline.com)

Figure 20: HOQ diagram created for the bipedal walking robot model

3.2 Computer-aided Modeling of the Bipedal Walking Robot Model

We will use the computer-aided design software *SolidWorks* in modeling our bipedal robot. As decided earlier, a total of 10 DOF will be provided for this model. The key design decisions to be made while designing this model include: the mass distribution of each link and actuation mechanisms provided at each degree of freedom for the robot model.

Based on the findings of [38, 39], the total length and mass of an average human being has been assumed to be approximately 170 *cm* and 67 *kg* respectively. The mass distribution ratio in an average human being is such that the ratio of the thigh section to the calf section is about 2.309 [40]. The following subsections are intended to explain the individual components of the robot assembly as well as to analyze the actuation mechanisms provided at each DOF of the robot.

3.2.1 Actuation Mechanism at the Hip Joints

As mentioned earlier, our bipedal robot model is proposed to consist of a link which acts like a pelvis with two hip joints. Each hip joint consists of 2 DOF. One DOF facilitates motion in the sagittal plane while the other allows motion in the coronal plane. At each of the hip joints, actuation in the sagittal plane is provided by a rotary actuator. It is attached to a bevel gear assembly with a gear ratio of 1:3 by means of a flexible coupling (as shown in the CAD model in **Figure 21**). The gear assemblies at both the hip joints are attached to the top end of the thigh sections as illustrated in the CAD model. The rotary actuator is positioned along the thigh link such that a majority of its mass is concentrated along the upper portion of the thigh. This will ensure that the

mass distribution along each thigh link is anthropomorphic (In human beings, the upper half of the thigh is bulkier compared to the lower half). The other degree of freedom is not actuated as it requires a very small torque during the walking motion.

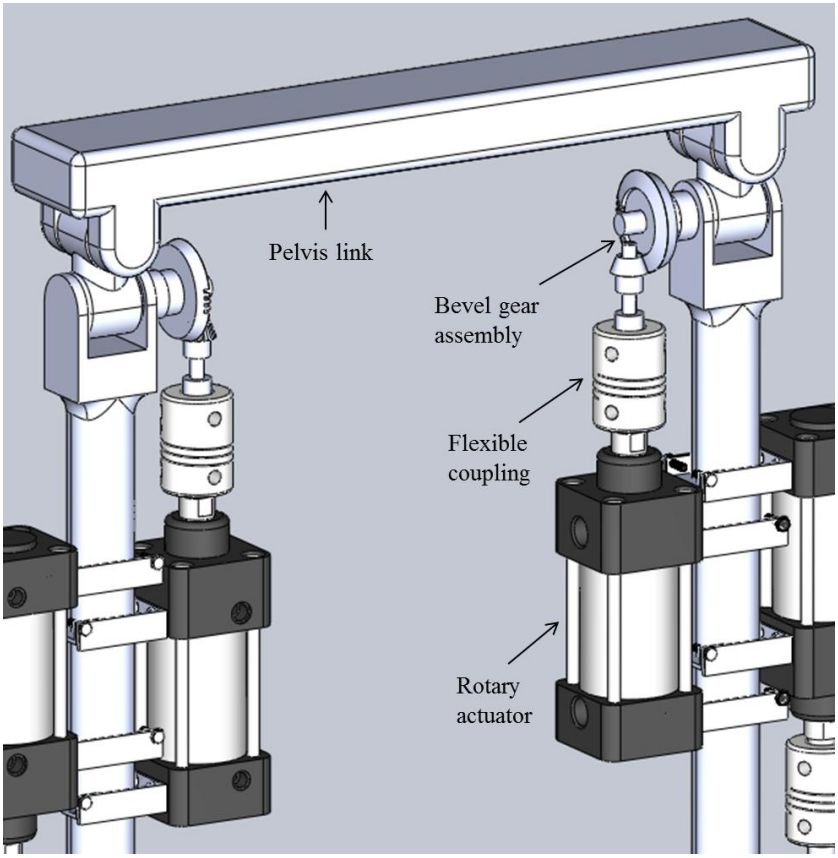

Figure 21: Actuation provided at the hip joints (shown with brackets and fasteners)

3.2.2 The Thigh Links and Actuation Mechanism at the Knee Joints

One end of each thigh link is attached to their corresponding hip joint as discussed earlier. The other end includes a knee stop and it connects to one end of the calf link to form the knee joint. This joint has 1 DOF which allows motion in the

sagittal plane. It is actuated by employing a similar actuation mechanism as that used for the hip joint. The rotary actuator is again aligned along the thigh link such that the mass is primarily concentrated along the upper portion of the thigh. This actuation setup is shown in **Figure 22**.

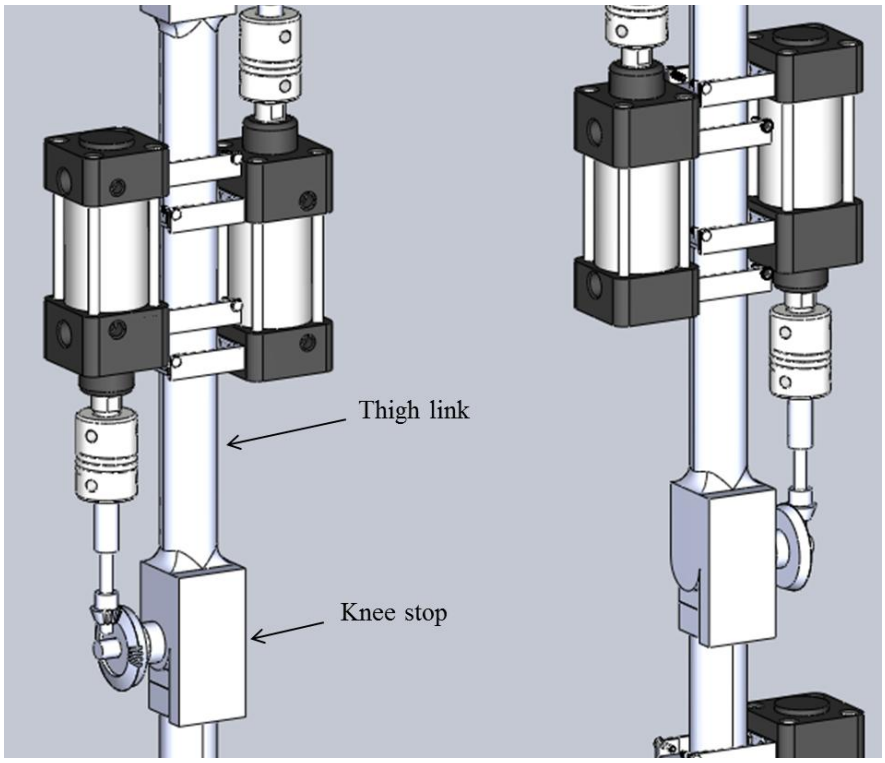

Figure 22: Actuation provided at the knee joints

3.2.3 The Calf Links and Actuation Mechanism at the Ankle Joints

One end of each calf link is attached to their corresponding knee joint as explained previously. The other end is attached to their respective foot link by means of an ankle joint. Choosing the actuation mechanism for the ankle joints is the trickiest

part of our biped robot model as this joint has 2 DOF which must be actuated. One of them enables rotation in the sagittal plane while the other allows rotation in the coronal plane.

The ankle joint has a design constraint which requires that one of the actuation mechanisms has to be flexible enough to bend to a certain extent (while ensuring that it does not disengage from the joint during the robot's motion). So, we analyze the dynamics at the ankle joint and conclude that the extent of rotation which occurs in the coronal plane is much lesser compared to that in the sagittal plane. Due to this reason,

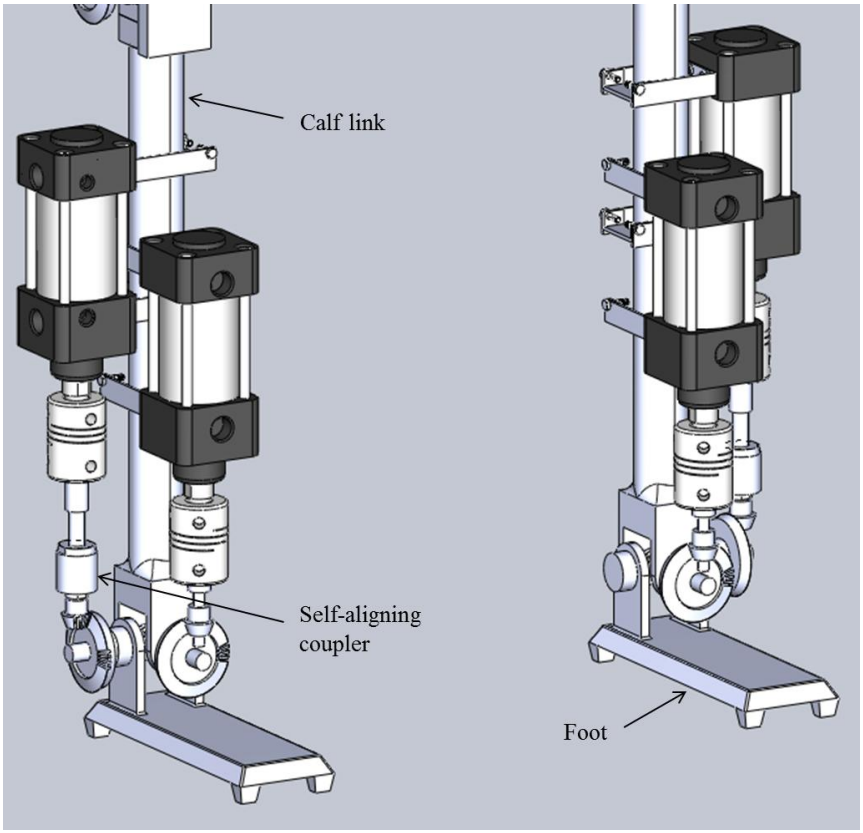

Figure 23: Actuation mechanisms provided at the ankle joints

we allow complete rotation in the sagittal plane by providing a rigid actuation mechanism which is identical to that employed at the hip and knee joints. These actuators would be aligned along the calf link such that the mass concentration is in the upper portion of the calf.

To allow for sufficient flexibility at the ankle joint, we propose that a *self-aligning coupler* could be used at the other DOF such that it forms a connection between the actuator shaft and the bevel gear assembly (as shown in **Figure 23**). According to [41], the self-aligning coupler is capable of a misalignment of about 5 degrees which is found to be sufficient to provide the necessary sideways motion (in the coronal plane) at the ankle joint.

3.2.4 Final CAD Model of the Bipedal Robot Assembly and Complicated Nature of Fabrication

By using the components and actuation mechanisms explained earlier, we have finally developed a CAD model of the bipedal robot assembly. **Figure 24** shows a rendered image (generated using PhotoWorks) of the complete robot assembly during motion.

Although we intend to build a physical model of the bipedal robot assembly, it is relatively complicated and would require a considerable amount of time and manual labor to get the robot to work in the desired manner. Also, we do not have a precise control circuit designed for the model. So, it would be ideal to perform some experiments on simpler models to get some valuable inputs for building the bipedal robot assembly. This forms the motivation for the development of the idea of the double

pendulum model. The design process and fabrication of this model as well as the purpose of experimentation will be discussed in the forthcoming sections.

Figure 24: Rendered version of the final CAD model of the bipedal robot assembly

4. RESEARCH APPROACH: DESIGN PROCESS AND FABRICATION PROCEDURE OF THE DOUBLE PENDULUM

The modeling of the bipedal robot assembly has been explained in detail in the previous section. However, due to the complicated nature of the model as well as the highly robust control mechanism required, we feel that it would be wise to obtain sufficient insight into building this model beforehand. This provides us with the necessary motivation to work on a double pendulum model which is conceptually similar yet physically simpler.

4.1 Proposed Design of the Double Pendulum Model

The purpose of considering the idea of the double pendulum is to build a physical model of a hybrid dynamic system for experimentation. This model is effectively a case study which helps in demonstrating that functional modeling and control theory can be successfully implemented on a simplified hybrid dynamic model. The functional model and House of Quality diagrams developed for the double pendulum model are shown in **Figures 25** and **26** respectively.

This double pendulum model is intended to simulate the impacts occurring at the knee joint in humans. So, this model will be designed similar to a human leg, comprising two rigid links with uniform mass distribution along with a mechanical stop (as proposed by Or and Ames [32]). Both the links of the double pendulum model

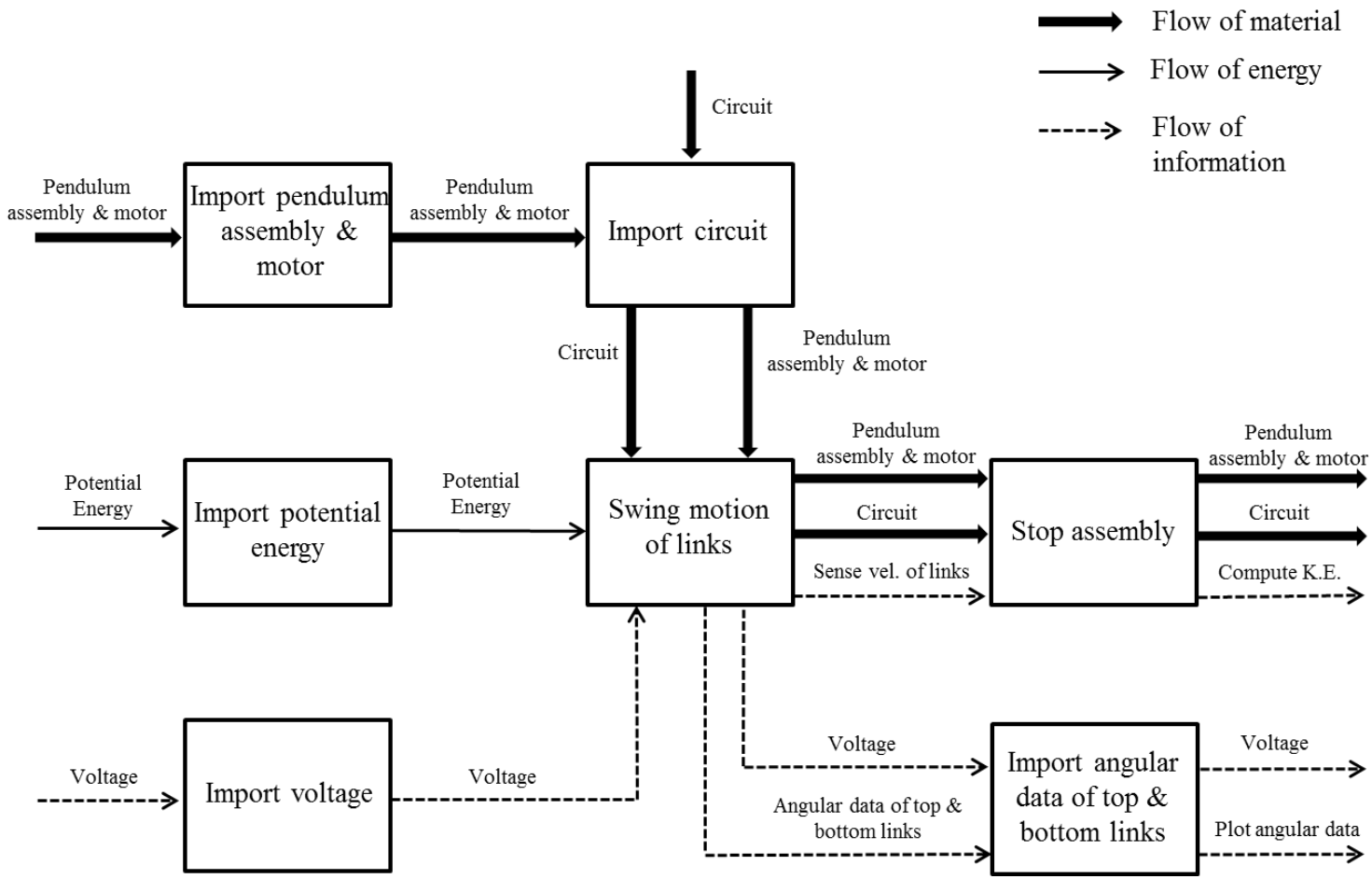

Figure 25: Functional model created for the double pendulum

Title: Design of a double pendulum with a mechanical stop

Author: Bhargav Kothapalli

Date:

Notes: The simplicity of the product could determine how aesthetically appealing the product could be. However this may not always be the case.

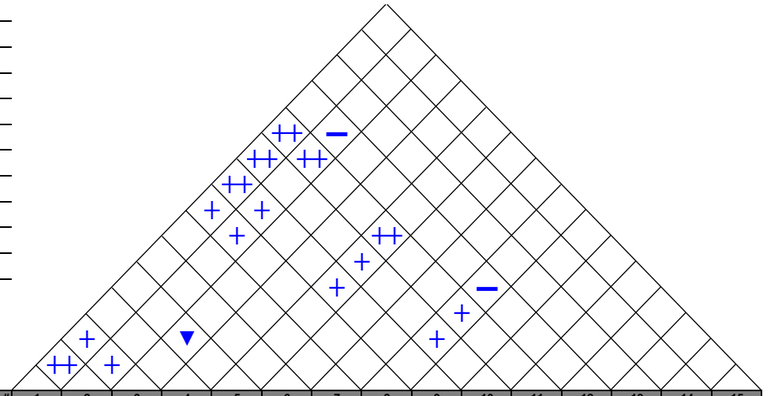

Legend		
⊖	Strong Relationship	9
O	Moderate Relationship	3
▲	Weak Relationship	1
++	Strong Positive Correlation	
+	Positive Correlation	
−	Negative Correlation	
▼	Strong Negative Correlation	
▼	Objective Is To Minimize	
▲	Objective Is To Maximize	
X	Objective Is To Hit Target	

Row #	Max Relationship Value in Row	Relative Weight	Weight / Importance	Demanded Quality (a.k.a. "Customer Requirements" or "Whats") \ Quality Characteristics (a.k.a. "Functional Requirements" or "Hows")	1 How similar is this model to the bipedal robot	2 Similarity to swing motion of human leg	3 Masses of links and the supports	4 Is it better to weld or attach the components of the assembly using fasteners	5 Stability of the total setup during operation	6 Speed of operaton	7 Similarity of physical setup to the CAD model	8 Level of complexity in building the circuit	9 Type of control implemented	10 Robustness of control law	11 Repeatability / consistencey of motion achieved	12 Optimization of cost of building the setup	13	14	15	Our Company	Competitor 1	Competitor 2	Competitor 3	Competitor 4	Competitor 5
				Direction of Improvement: Minimize (▼), Maximize (▲), or Target (x)		x		x		▼	▲	▼	x	x	▲	▲				**Competitive Analysis** (0=Worst, 5=Best)					
1	9	11.3	8.0	Cost of building the assembly	O					O		⊖				⊖								
2	9	12.8	9.0	What is its reliability?	⊖	▲	O							▲		▲								
3	9	12.1	8.5	Is the model portable?				⊖	⊖		⊖	O												
4	3	12.8	9.0	What are the time constraints?										O	O									
5	9	12.8	9.0	Ease of implementation of control			⊖						O	⊖										
6	3	9.9	7.0	Is the product aesthetically appealing?												O								
7	9	14.2	10.0	At what speed does it need to operate?		⊖				⊖		▲												
8	9	14.2	10.0	What are we trying to measure/observe?		⊖							O		⊖									
9																								
10																								
				Target or Limit Value	Closest to human movement	Similar in terms of the impacts observed		Components should be attached using fasteners	Vibrations should be minimal	Depends on simulation data	Same geometry should be used		Feedback PD control	Should be as accurate as possible	Repeatability is most important	$2,000									
				Difficulty (0=Easy to Accomplish, 10=Extremely Difficult)	9	9	7	7	9	8	7	9	6	9	10	5									
				Max Relationship Value in Column	9	9	9	9	9	9	9	9	3	9	9	9									
				Weight / Importance	148.9	268.1	153.2	108.5	108.5	161.7	108.5	152.5	80.9	166.0	166.0	144.7									
				Relative Weight	8.4	15.2	8.7	6.1	6.1	9.1	6.1	8.6	4.6	9.4	9.4	8.2									

Powered by QFD Online (http://www.QFDOnline.com)

Figure 26: HOQ diagram created for the double pendulum

would be attached using two revolute joints. As a result, this model will consist of 2 DOF. While the degree of freedom corresponding to the top link would be actuated by a motor, the bottom link will remain unactuated. The mechanical stop will restrict the swing motion of the bottom link in one direction. This would introduce impacts in this system at the mechanical stop. Balls with different coefficients of restitution will be included in the mechanical stop to ensure that the impacts occurring at the stop are *non-plastic*.

The objective of our experiments is to validate the product design process by establishing the existence of Zeno and obtaining Zeno periodic orbits in the physical model of the double pendulum.

4.2 Computer-aided Modeling of the Double Pendulum Model

To create the CAD model of the double pendulum, I follow a design procedure identical to that implemented for the bipedal robot model. As explained earlier, I focus on observing impacts at the knee joint by achieving human leg motion using this model. In order to obtain accurate results, it is extremely important that the model experiences minimal vibration, i.e., stability has to be ensured during experimentation. This forms an essential design consideration while developing the CAD model.

The development of the CAD model of the double pendulum involves several design iterations. During each of these design iterations, the setup will be analyzed and improved to ensure that the basic design requirements are fulfilled. In the *first design iteration*, the setup is proposed to be comprised of a rigid vertical support fixed to a base

plate as shown in **Figure 27 (a)**. A BN28 Silencer series 72V brushless DC motor (with optional encoder) [42] is attached at the top of this support and the motor shaft drives the

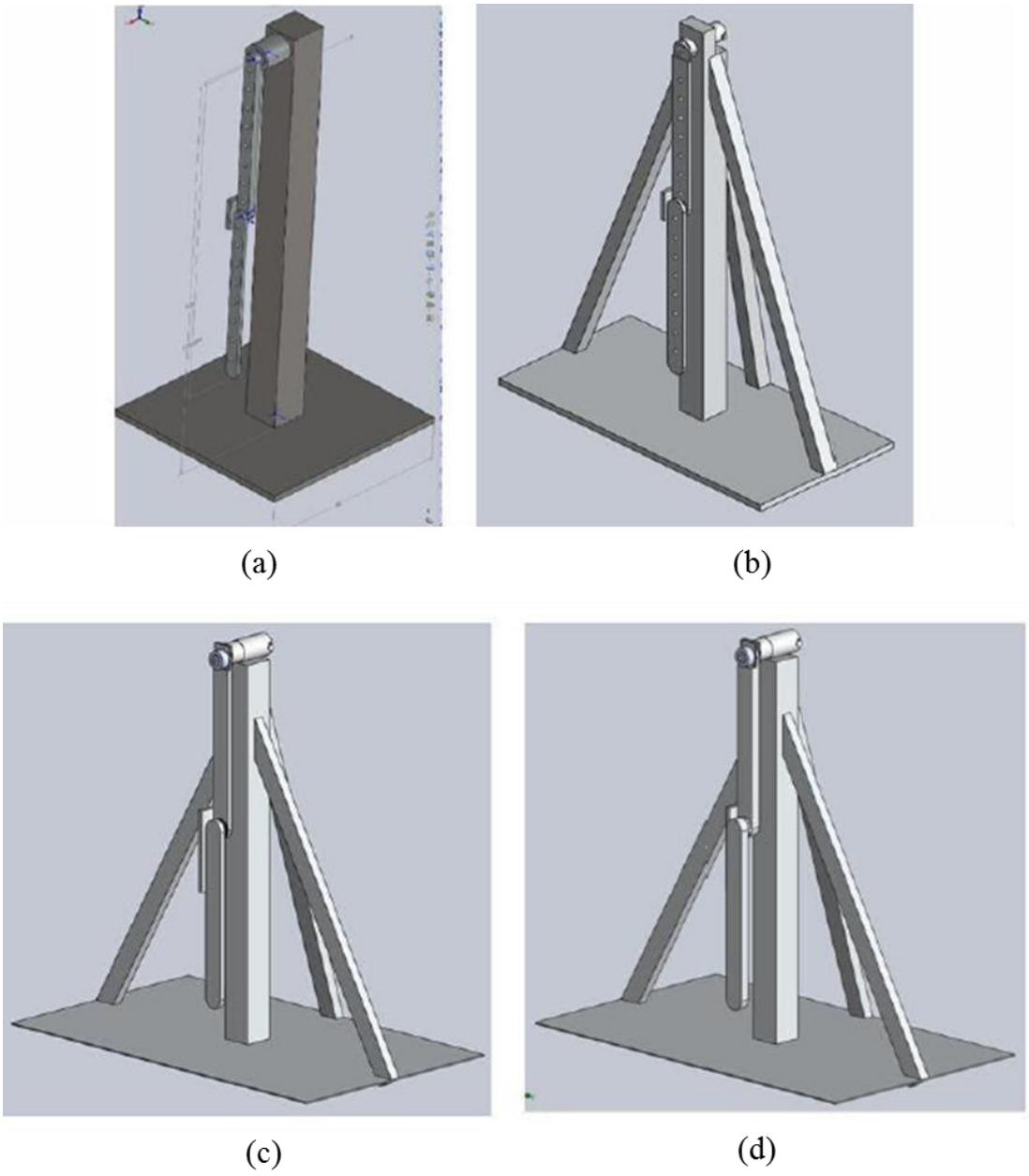

Figure 27: Four Design iterations of the double pendulum CAD model (shown in order from (a) to (d))

top link of the pendulum using a small coupling as shown. The bottom link is attached to the top link using a ball and roller bearing. Both the pendulum links have dimensions of 18" x 2" x 0.5" each. However, as this model uses only a single central support, the swinging motion of the solid pendulum links would generate considerable sideways momentum during experimentation and destabilize the model.

To solve this issue, a *second design iteration* is proposed wherein two side supports and a back support are attached to the main support to make the model sturdier (as illustrated in **Figure 27 (b)**). The length of the base plate is increased to accommodate the two side supports which are attached to either side of the central vertical support at an angle of 60 degrees to the base.

In the *third design iteration*, the positions of the side and back supports are lowered. Also, the motor is mounted on the top of the vertical support unlike in the previous iteration (as shown in **Figure 27 (c)**). These modifications would reinforce the lower portion of the setup, thereby making it more stable.

As the pendulum is expected to imitate the functioning of a human leg, the pendulum links should be heavier to obtain better experimental results. So, in order to increase the mass of each link, we propose a *fourth design iteration* to double their existing thickness (**Figure 27 (d)**).

Due to the increased mass of the links, we realize that the existing motor would not be able to provide sufficient torque for operating the setup at different speeds. So, a *fifth design iteration* is proposed to include a Leeson 0.5 hp, 90 VDC gearmotor to drive the top link. The motor will be accommodated in the assembly with the help of an

aluminum support plate which will be mounted on top of the central vertical support. Additionally, two incremental encoders, one at each DOF, will be utilized for obtaining the angular position data during experimentation. All design considerations have been taken care of at this point and we have finalized this CAD model as the basis for building the physical model. **Figure 28** shows the rendered version (generated using SolidWorks) of the final CAD model.

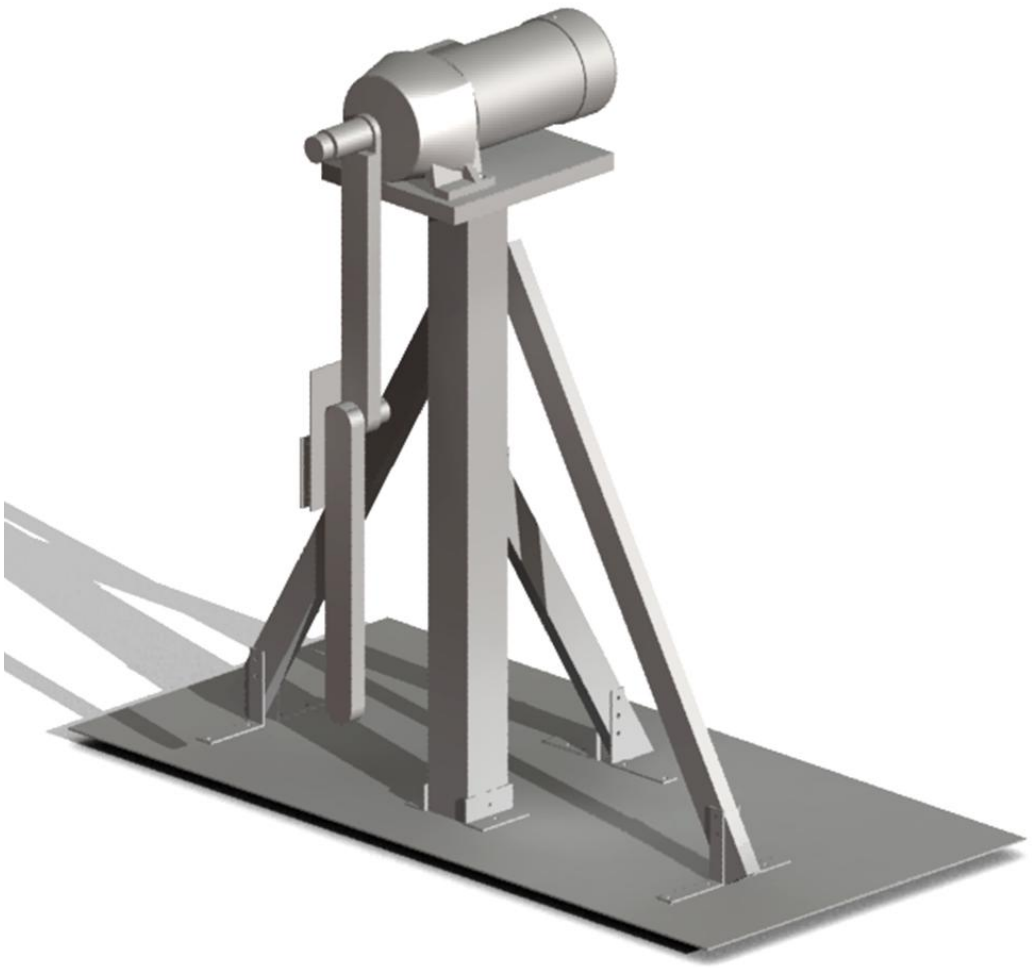

Figure 28: Rendered image of the final CAD model of the double pendulum

4.3 Fabrication of the Physical Model of the Double Pendulum (Including Electrical Circuit)

Suitable materials are to be identified and utilized to fabricate each individual component in the double pendulum assembly in the desired manner. A steel plate measuring 24” x 48” x 0.125” is bolted to a 24” x 48” x 1” medium density fiber (MDF) board to form a sturdy base for the model. An aluminum metal stock of dimensions 3” x 3” x 36” is suitably machined to form the main support of this assembly while the 2 side supports and the back support are machined out of 3 separate pieces of aluminum metal stock measuring 1" x 2" x 36" each. The main support is bolted to the base using angle iron brackets while suitable L-brackets are used to attach the other supports to the base and the main support to form the *support assembly* for the model.

However, it is observed that the side supports exert high pulling stresses on the base, causing it to warp. This would affect the stability of the model during experimentation. In order to tackle this problem, additional support is provided by fixing several wooden blocks, each measuring 11.5” x 3.5” x 1.5”, to the base. **Figure 29** shows a snapshot of the physical setup of the double pendulum (mounted on a wooden platform to reduce vibrations during experimentation). It has been ensured that the physical setup resembles the CAD model as closely as possible (in terms of structure and dimensions without compromising on sturdiness). This can be clearly observed by comparing **Figures 25** and **26**.

Anodized aluminum is used to fabricate the two pendulum links, each measuring 18” x 2” x 1”. As mentioned previously, a Leeson 90 VDC motor is used to actuate the

top link. The motor is supported by an aluminum plate of dimensions 10" x 12" x 1" and is mounted on top of the main support. The assembly also includes two encoders which are fixed at the two revolute joints in the assembly. These encoders form a part of the electrical circuit for the model and they will record the angular position data of each link during experimentation.

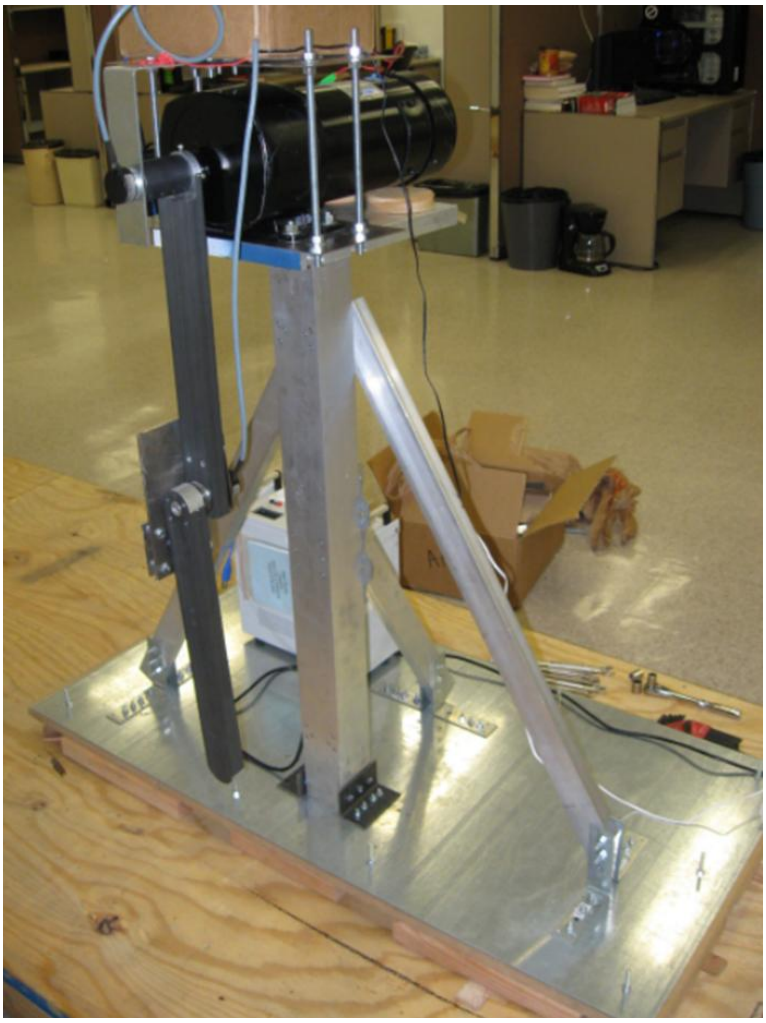

Figure 29: Snapshot of the physical setup of the double pendulum

Finally, the mechanical stop assembly is fabricated with the help of two steel plates of dimensions 4” x 8” x 0.125” and 4” x 3” x 0.125” respectively. These plates are used to sandwich a ball measuring 1” in diameter. A provision is made such that a portion of the ball protrudes out of one side of the mechanical stop. This ensures that non-plastic impacts occur at the stop. We will use 2 balls with different coefficients of restitution for experimentation to observe how the change in the non-plasticity of impacts affects Zeno behavior. **Figure 30** shows a closer view of the mechanical stop. A complete list of the Bill of Materials (BOM) used for building the double pendulum assembly has been provided in **Table 1** (**Appendix – A**).

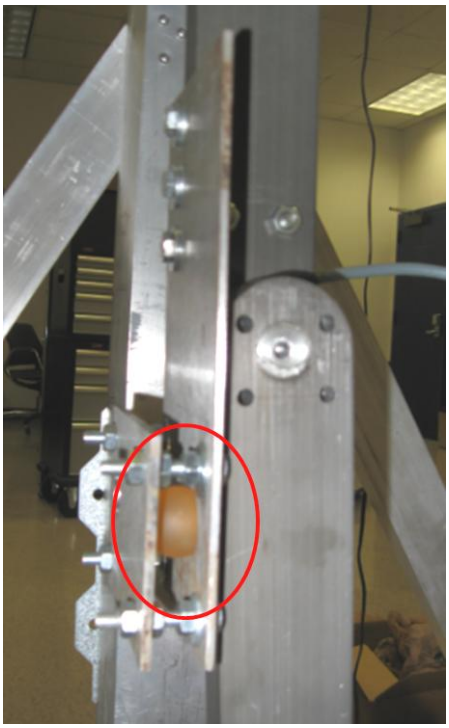

Figure 30: Snapshot showing a closer view of the mechanical stop (red ellipse highlights the 1” polyurethane ball fitted in the stop)

The electrical circuit board for operating motor has been prepared using the components listed in **Table 2** (**Appendix – A)**. A snapshot of the circuit board has been shown in **Figure 31**.

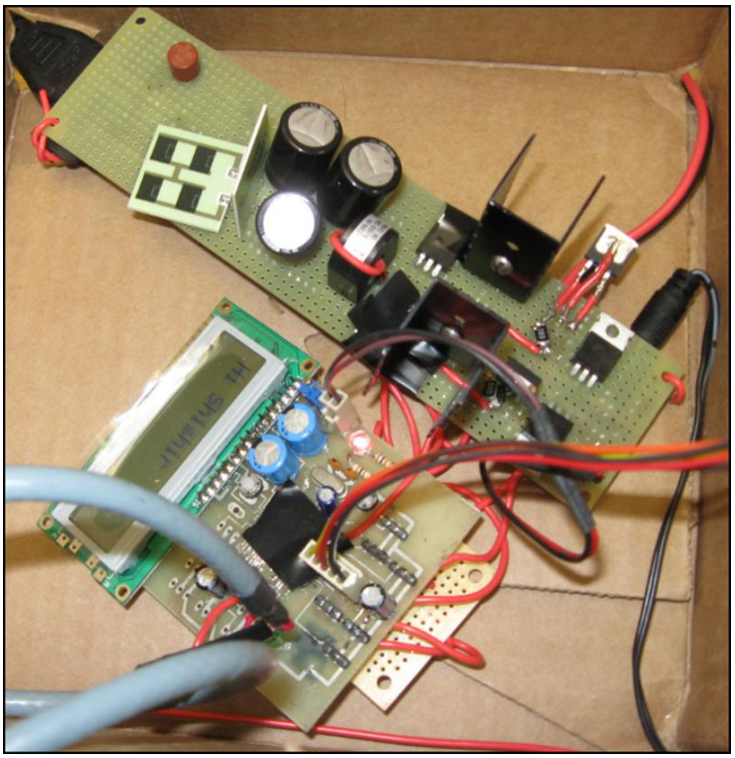

Figure 31: Snapshot of the electrical circuit used for operating the motor

5. RESULTS, ANALYSIS AND CONCLUSIONS

In this section, the results obtained by theoretical simulation as well as experimentation will be discussed and compared. We will then analyze the results to understand their significance towards achieving our objective, i.e., establishing the existence of Zeno behavior and Zeno periodic orbits.

5.1 Simulation of the Double Pendulum Model

Apart from the aforementioned objectives, the double pendulum model is intended to provide some insight into the phenomena of *knee-lock* and *knee-bounce* in bipedal walking. These phenomena have been discussed in various sources [43-45]. The theoretical simulation of the double pendulum will include a mathematical model which is based on the model presented by Or and Ames [30, 46].

The mathematical model for this hybrid system primarily involves the following computations: development of the inertia values of the links and the motor, the impact equations including the reset map, development of the control law and the Lagrangian multiplier. The model will also accommodate the physical parameters used in the experimental setup in order to facilitate the comparison of the results obtained from simulation with the experimental results. The parameters of the physical setup would include the actual masses and moments of inertia of the rotating parts, coefficients of restitution of the balls used in the mechanical stop, control parameters and motor constants. A feedback PD control law is applied to implement control in this hybrid

dynamic system. In the following subsection, the procedure for formal and practical completion of hybrid systems and determining Zeno stability will be explained. These explanations will facilitate a better interpretation of the results from numerical simulation of the double pendulum and relate them with the results obtained from the experimental setup.

5.1.1 Formal Completion of Lagrangian Hybrid Systems

We will now formally define a completed Lagrangian hybrid system. As explained in [32], a Zeno point c_∞ is not a physical equilibrium point as it satisfies the condition, $f_{\mathrm{L}}(c_\infty) \neq 0$ and involves non-zero velocity. This forms the motivation to complete hybrid systems. Let us now look at the Lagrangian equations of motion for holonomically constrained dynamic systems.

$$M(q)\ddot{q} + C(q,\dot{q}) + N(q) = dh(q)^T \lambda \tag{23}$$

The solution for Lagrange multiplier λ is given as,

$$\lambda(q,\dot{q}) = (dh(q)M(q)^{-1}dh(q^T))^{-1}[dh(q)M(q)^{-1}(C(q,\dot{q})\dot{q} + N(q)) - \dot{q}^T H(q)\dot{q})] \tag{24}$$

where $H(q)$ is the Hessian of h at q. So, we obtain the following vector field from the constrained equations of motion.

$$\begin{aligned} \dot{x} &= f_{\mathrm{L}}^{\lambda}(x) \\ &= \begin{bmatrix} \dot{q} \\ -M(q)^{-1}(C(q,\dot{q})\dot{q} + N(q) - dh(q)^T \lambda(q,\dot{q})) \end{bmatrix} \end{aligned} \tag{25}$$

In the above equation, f_{L}^{λ} is a vector field on the manifold $TQ|_{h^{-1}(0)}$, from which we determine the dynamic system $D_{\mathrm{L}} = (TQ|_{h^{-1}(0)}, f_{\mathrm{L}}^{\lambda})$. For this dynamic system, $q(t)$ slides along the surface $h^{-1}(0)$ for a positive constraint force λ.

Let us now recall the definition of Zeno (Section 2). A hybrid execution χ^{H} is considered to be Zeno when $\Lambda = \mathbb{N}$ and $\lim_{i\to\infty} t_i = t_\infty < \infty$. Here Λ is an indexing set while t_∞ is called the *Zeno time*. If $\chi^{H_{\mathrm{L}}}$ is a Zeno execution of a Lagrangian hybrid system $\boldsymbol{H}_{\mathbf{L}}$, then the *Zeno point* is defined as,

$$c_\infty = (q_\infty, \dot{q}_\infty) = \lim_{i\to\infty} c_i(t_i) = \lim_{i\to\infty} (q_i(t_i), \dot{q}_i(t_i)) \tag{26}$$

These limit points are intricately related to unique type of equilibrium points relevant to hybrid systems – Zeno equilibria. For a dynamic system D_{L}, a constrained execution $\tilde{\chi}$ is a pair $(\tilde{I}, \tilde{c})$ where $\tilde{I} = (\tilde{t}_0, \tilde{t}_f) \subset \mathbb{R}$ if $\tilde{t}_f = \infty$ and zeno point is defined as $\tilde{c} : I \to TQ$. The solution for equation (23) is given by $\tilde{c}(t) = (q(t), \dot{q}(t))$ which satisfies the following properties:

(i) $h(q(\tilde{t}_o)) = 0,$

(ii) $dh(q(\tilde{t}_o), \dot{q}(\tilde{t}_o)) = 0,$

(iii) $\lambda(q(\tilde{t}_o), \dot{q}(\tilde{t}_o)) > 0,$

(iv) $\tilde{t}_f = \min\{t \in \tilde{I} : \lambda(q(t_o), \dot{q}(t_o)) = 0\}.$

We will now present the notion of a completed hybrid system. If **L** is a hybrid Lagrangian and $\boldsymbol{H}_{\mathbf{L}}$ is the corresponding Lagrangian hybrid system, the definition of the *completed Lagrangian hybrid system* is,

$$\overline{\boldsymbol{H}}_{\mathbf{L}} := \begin{cases} D_{\mathrm{L}} & \text{if} \quad h(q)=0,\ dh(q)\dot{q}=0,\ \lambda(q,\dot{q})>0 \\ \boldsymbol{H}_{\mathbf{L}} & \text{otherwise.} \end{cases} \tag{27}$$

The transition from the hybrid system $\boldsymbol{H}_{\mathbf{L}}$ to the constrained system D_{L} can be made only when a specific Zeno execution reaches its Zeno point while the transition from D_{L} to $\boldsymbol{H}_{\mathbf{L}}$ occurs when the constraint force λ crosses zero. The completed hybrid system $\overline{\boldsymbol{H}}_{\mathbf{L}}$ can be represented graphically as shown in **Figure 32** [32].

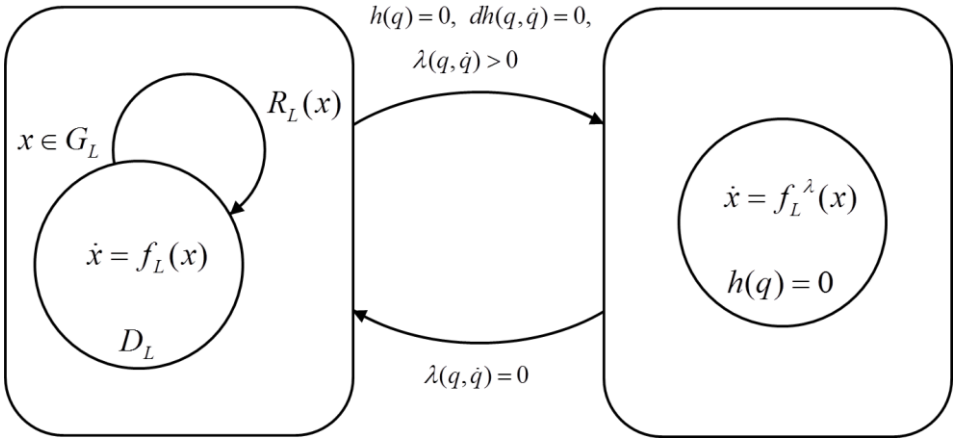

Figure 32: A graphical representation of the completed hybrid system [32]

According to [47], the acceleration of $h(q(t))$ in unconstrained dynamics (equations of motion presented in (10)) can be expressed as,

$$\ddot{h}(q,\dot{q}) = \dot{q}^T H(q)\dot{q} - dh(q)M(q)^{-1}(C(q,\dot{q})\dot{q}+N(q)) \tag{28}$$

By examining the expressions for $\lambda(q,\dot{q})$ and $\ddot{h}(q,\dot{q})$, it can be said that $\ddot{h}=0$ and $\lambda>0$ correspond to constrained motion while the conditions $\ddot{h}>0$ and $\lambda=0$ correspond to the system leaving the constraint surface $h^{-1}(0)$ and switching back to hybrid dynamics. This satisfies the definition of the completed Lagrangian hybrid system.

Let us now consider the notion of a *completed execution* of a completed hybrid system. For a simple hybrid Lagrangian **L** and its corresponding completed hybrid system $\overline{\boldsymbol{H}}_{\mathbf{L}}$, a completed execution $\overline{\chi}$ is defined as an infinite ordered sequence of alternating hybrid and constrained executions and is given as,

$$\overline{\chi}=\{\chi^{(1)},\ \tilde{\chi}^{(2)},\ \chi^{(3)},\ \tilde{\chi}^{(4)},\ ...\}$$

which satisfies the conditions given below:

(i) For each pair $\chi^{(i)}$ and $\tilde{\chi}^{(i+1)}$,
$t_{\infty}^{(i)}=\tilde{t}_0^{(i+1)}$ and $c_{\infty}^{(i)}=\tilde{c}_0^{(i+1)}(\tilde{t}_0^{(i+1)})$.

(ii) For each pair $\tilde{\chi}^{(i)}$ and $\chi^{(i+1)}$,
$\tilde{t}_f^{(i)}=t_0^{(i+1)}$ and $\tilde{c}_{\infty}^{(i)}(\tilde{t}_f^{(i)})=c_0^{(i+1)}(t_0^{(i+1)})$.

Here the subscript (i) indicates values corresponding to the i-th execution in $\overline{\chi}$, and $t_{\infty}^{(i)}$, $c_{\infty}^{(i)}$ denote the Zeno time and Zeno point associated with the i-th hybrid execution $\chi^{(i)}$.

5.1.2 Practical Completion of Hybrid Systems and Stability of Zeno Equilibria

Zeno behavior and zeno equilibria as well as the sufficient conditions required for its existence have been discussed in Section 2. We will now look at the procedure

for completing hybrid systems in practice and understand the conditions for stability of Zeno equilibria.

According to Or and Ames [32, 47], the notion of completed hybrid system explained earlier cannot be applied in practice unless we have a accurate knowledge of Zeno executions. Due to the infinite number of discrete executions required to be computed, it is essential to develop a practical method for completing hybrid systems which is in agreement with the numerical simulation. This would require a finite truncation of the infinite sequence of the discrete transitions. So, in order to ensure accuracy of numerical approximation after the finite truncation of Zeno executions, a notion for practical completion of hybrid systems is necessary.

In order to simulate Zeno executions accurately, it is necessary to handle two problems which could affect its reliability [32]. Firstly, one should ensure the approximate Zeno behavior replicates the true behavior and does not show an aliasing affect due to truncations. Secondly, as part of the completion process, the numerical simulation needs to generate an approximate Zeno point which serves as the initial condition for the next phase of constrained dynamics. So, to generate a reliable simulation, one needs to guarantee that the approximated Zeno point lies in an arbitrarily close neighborhood of the exact Zeno limit point (which cannot be computed analytically). The aforementioned problems can be addresses by utilizing the results pertaining to sufficient conditions for existence of Zeno and for stability of Zeno equilibria. The sufficient conditions necessary for existence of Zeno executions are given by the following theorem [32, 36]:

Theorem 2: *Let* $\boldsymbol{H}_{\mathrm{L}}$ *is a simple Lagrangian hybrid system and let* $x^* = (q^*, \dot{q}^*)$ *be a Zeno equilibrium point of* $\boldsymbol{H}_{\mathrm{L}}$. *If* $e < 1$ *and* $\ddot{h}(q^*, \dot{q}^*) < 0$, *there exists a neighborhood* $W \subset D_{\mathrm{L}}$ *of* x^* *such that for every* $x_0 \in W$, *there is a unique Zeno execution* $\chi^{\boldsymbol{H}_{\mathrm{L}}}$ *with* $c_0(t_0) = x_0 = (q_0, \dot{q}_0)$.

This theorem is useful in detecting potential Zeno limit points, such that it is possible to truncate an execution in their vicinity and switch to a constrained system while preserving the qualitative behavior of the exact solution. However, the above theorem does not provide a measure how close to the limit point one should truncate or how large the resulting error is from the approximation. Due to this reason, the definition of stability of Zeno equilibria has been provided as follows:

Let $x^* = (q^*, \dot{q}^*)$ be a Zeno equilibrium point in a simple Lagrangian hybrid system $\boldsymbol{H}_{\mathrm{L}}$. Then x^* is defined as a *bounded-time locally stable* (BTLS) if for each open neighborhood $U \subseteq TQ$ of x^* and $\varepsilon_t > 0$, there exists another open neighborhood W of x^*, such that for every initial condition $c_0(t_0) \in W \cap D_{\mathrm{L}}$, the corresponding hybrid execution $\chi^{\boldsymbol{H}_{\mathrm{L}}}$ is Zeno, and satisfies $c_i(t) \in U$ for all $t \in I_i$ and $i \in \Lambda$, while its Zeno time satisfies $t_\infty - t_0 < \varepsilon_t$. This definition is identical to the notion of *uniform Zeno stability*. Let us now look at another theorem which establishes the conditions for BTLS of Zeno equilibria for a simple Lagrangian hybrid system.

Theorem 3: *Let* $x^* = (q^*, \dot{q}^*)$ *be a Zeno equilibrium point of a simple Lagrangian hybrid system* $\boldsymbol{H}_{\mathrm{L}}$. *Then the following 2 conditions hold:*

(i) *If* $e < 1 \text{ and } \ddot{h}(q^*, \dot{q}^*) < 0$, *then* x^* *is* BTLS

(ii) *If* $\ddot{h}(q^*, \dot{q}^*) > 0$, *then* x^* *is not* BTLS

The above theorem indicates that the theorem presented earlier to provide sufficient conditions for Zeno executions is also sufficient for bounded-time local stability. This theorem has been proved in [47] and provides an explicit construction of the neighborhood W for a given neighborhood U, which is essential for practical completion of hybrid systems. In the next subsection, we will look at the mathematical model of the numerical simulation undertaken for the double pendulum model. This model will provide us with the practical results of Zeno equilibrium points and Zeno stability for the double pendulum.

5.1.3 Mathematical Model of the Double Pendulum Problem

As explained in [30], a simple Lagrangian hybrid system can be represented by the tuple, **L** = (*Q*, *L*, *h*). The configuration of the double pendulum can be defined by $q = (\theta_1, \theta_2, \dot{\theta}_1, \dot{\theta}_2)$ and its equations of motion can be represented by the Lagrangian *L*. The mechanical stop represents a unilateral constraint, $h = \theta_2 \geq 0$.

Let us consider the evaluation of the moments of inertia of the moving parts of the double pendulum, i.e., the rotating parts of the motor, the top link and the bottom link. In this computation, the masses of the first link and the rotating parts of the motor (armature and gear train) are included together and denoted as m_1 while the mass of the second link is denoted as m_2. The coefficient of restitution of the ball is denoted as e.

The parameters chosen for simulating the mathematical model are (in IPS units) as follows: $m_1 = 13.25\ lbs$, $m_2 = 3.55\ lbs$, $L_1 = L_2 = 18\ in$ and x.

These values along with the coefficient of restitution e (for each ball considered) form the constant substitutions while the generalized coordinates (θ_1, θ_2) and velocities $(\dot{\theta}_1, \dot{\theta}_2)$ as well as the input current to the 90 VDC gearmotor (i_M) are included as the state substitutions in the mathematical model. The moment of inertia for the motor (I_M) is evaluated as follows:

$$I_M = I_A G_R^2 + m_M x_M^2 \tag{29}$$

Here I_A is the inertia of the armature ($7.2\ lb-in^2$) and G_R is the gear ratio of the motor (53 : 1). The numerical values mentioned are listed in the motor specifications. The inertia of the top link (I_t) is given by the following matrix,

$$I_t = \begin{bmatrix} m_t & 0 & 0 & 0 & 0 & 0 \\ 0 & m_t & 0 & 0 & 0 & 0 \\ 0 & 0 & m_t & 0 & 0 & 0 \\ 0 & 0 & 0 & \left(\frac{1}{12} m_l (L_l^2 + w_l^2) + m_l x_l^2\right) + \left(\frac{1}{2} m_c r_c^2 + m_c x_c^2\right) & 0 & 0 \\ & & & + \left(\frac{1}{12} m_{p_1} (L_{p_1}^2 + w_{p_1}^2) + m_{p_1} x_{p_1}^2\right) & & \\ & & & + \left(\frac{1}{12} m_{p_2} (L_{p_2}^2 + w_{p_2}^2) + m_{p_2} x_{p_2}^2\right) & & \\ 0 & 0 & 0 & 0 & 0 & 0 \\ 0 & 0 & 0 & 0 & 0 & 0 \end{bmatrix} \tag{30}$$

Here, for ease of representation, we have considered that the mass of the top link (m_t) includes the masses of the anodized aluminum portion (m_l), the clamp-on shaft coupling

(m_c) as well as the front and back plates (m_{p_1}, m_{p_2}) of the mechanical stop. The inertia of the bottom link (I_b) is given by the following matrix,

$$I_b = \begin{bmatrix} m_2 & 0 & 0 & 0 & 0 & 0 \\ 0 & m_2 & 0 & 0 & 0 & 0 \\ 0 & 0 & m_2 & 0 & 0 & 0 \\ 0 & 0 & 0 & \left(\frac{1}{12} m_2 (L_2^2 + w_2^2)\right) & 0 & 0 \\ 0 & 0 & 0 & 0 & \left(\frac{1}{12} m_2 (L_2^2 + t_2^2)\right) & 0 \\ 0 & 0 & 0 & 0 & 0 & m_2 \end{bmatrix} \quad (31)$$

In the above equation, the mass, length, width and thickness of the second link have been denoted by m_2, L_2, w_2 and t_2 respectively. It should be noted that all the moments of inertia have been evaluated about the respective center of mass values of the moving parts.

After including the mass and inertia parameters of the motor, we have computed the mass matrices for the double pendulum model to be,

$$M_{11} = 20820 + \frac{-3288120\, L_1 + L_1^2 (138701 + 7500\, m_1)}{134832} + \frac{1}{3}\left(1 + 3L_1^2 + 3L_1 L_2 \cos\theta_2 + L_2^2\right)$$
$$= 21385.46 + 324 \cos\theta_2$$

$$M_{12} = \frac{1}{6} m_2 \left(2 + 3L_1 L_2 \cos\theta_2 + 2L_2^2\right) = M_{21}$$
$$= 384.58 + 162 \cos\theta_2$$

$$M_{22} = \frac{1}{3} m_2 \left(1 + L_2^2\right)$$
$$= 384.58$$

Since, we have shown that the double pendulum model is a Lagrangian hybrid system, the new Lagrangian vector field (f_P) will include an extra state $\dot{i}_M$, where i_M is the input current to the DC motor.

$$\begin{pmatrix} \dot{x} \\ \dot{i}_M \end{pmatrix} = f_P(x) = \begin{bmatrix} \dot{q} \\ M(q)^{-1}(-C(q,\dot{q})\dot{q} - N(q) + u(i)) \\ \left(\dfrac{V_{in}(q,\dot{q}) - K_e\dot{\theta}_1 - R_M i_M}{L_M} \right) \end{bmatrix} \tag{32}$$

Here $V_{in}(q,\dot{q})$ is the input voltage to the motor, K_e is the motor's voltage constant, R_M is the motor winding resistance and L_M is the motor winding inductance. In the above equation, the motor torque has been denoted as $u(i)$ instead of $u(q,\dot{q})$ because the torque can now be expressed as a function of the motor input current as,

$$u(i) = K_\varphi i_M \tag{33}$$

where K_φ denotes the motor's torque constant. It should be noted that the configuration space of the double pendulum is spanned by $\mathbb{R}^5$ and is given by, $(\theta_1, \theta_2, \dot{\theta}_1, \dot{\theta}_2, i_M)$.

The new hybrid system including the motor is now defined as, $\boldsymbol{H_{LP}} = (D_P, G_P, R_P, f_P)$. The set of Zeno equilibria for the double pendulum system are now given by, $Z_P = \{(\theta_1, \theta_2, \dot{\theta}_1, \dot{\theta}_2, i_M) \in D_P : \theta_2 = 0, \dot{\theta}_2 = 0\}$. That is, the set of Zeno equilibria are the set of points where the bottom link is "locked" with the top link. Also note that during impacts and during constrained motion of the double pendulum, the equation for $\dot{i}_M$

remains unaffected. So, the reset map (defined in Section 2) for this hybrid system will be,

$$R_P(q,\ \dot{q},\ i_M) = \begin{bmatrix} q \\ \dot{q} - (1+e)\dfrac{dh(q)\dot{q}}{dh(q)M(q)^{-1}dh(q)^T} M(q)^{-1}dh(q)^T \\ i_M \end{bmatrix} \tag{34}$$

The feedback PD control law used for the simulation is now modified to,

$$V_{in}(q,\dot{q}) = -K_p(\theta_1 - \theta_{1e}) - K_d\dot{\theta}_1 \tag{35}$$

Here K_p and K_d are the proportional and derivative control constants respectively. The control values used in our numerical simulation are $K_p = 3$ and $K_d = -1$. Due to the negative value used for the derivative control constant, the control law is effectively considered to be P (minus D). The following motor constants have been used in the both the numerical simulation of the system: $R_M = 0.45\ Ohms$, $K_\varphi = 4.6\ lb-in/Amp$, $K_e = 0.561\ V/(rad/s)$ and $L_M = 8\ mH$.

It is now important to understand the fact that the existence of *Zeno periodic orbits* must be formally proved with the motor included in the model.

5.1.4 Formally Verifying Zeno Behavior

In this section, we will verify that the hybrid system model for the double pendulum with a mechanical stop displays Zeno behavior. In order to ensure that the completed execution $\overline{\chi}$ is unique if the conditions of Theorem 2 are satisfied. Let us consider the unilateral constraint,

$$h(q,\ \dot{q},\ i_M) = \theta_2(t) \tag{36}$$

By taking the double derivative of $h(q, \dot{q}, i_M)$, we get,

$$\ddot{h}(q, \dot{q}, i_M) = \ddot{\theta}_2(t) \tag{37}$$

Therefore, as long as $\ddot{\theta}_2(t) < 0$ immediately after every impact, Theorem 2 says that the system is *Zeno stable*. And $\ddot{\theta}_2(t)$ can be obtained from the fourth row of the vector field given in equation (32).

$$\ddot{\theta}_2(t) = f_P^{\lambda}(x)_{\ddot{\theta}_2} \tag{38}$$

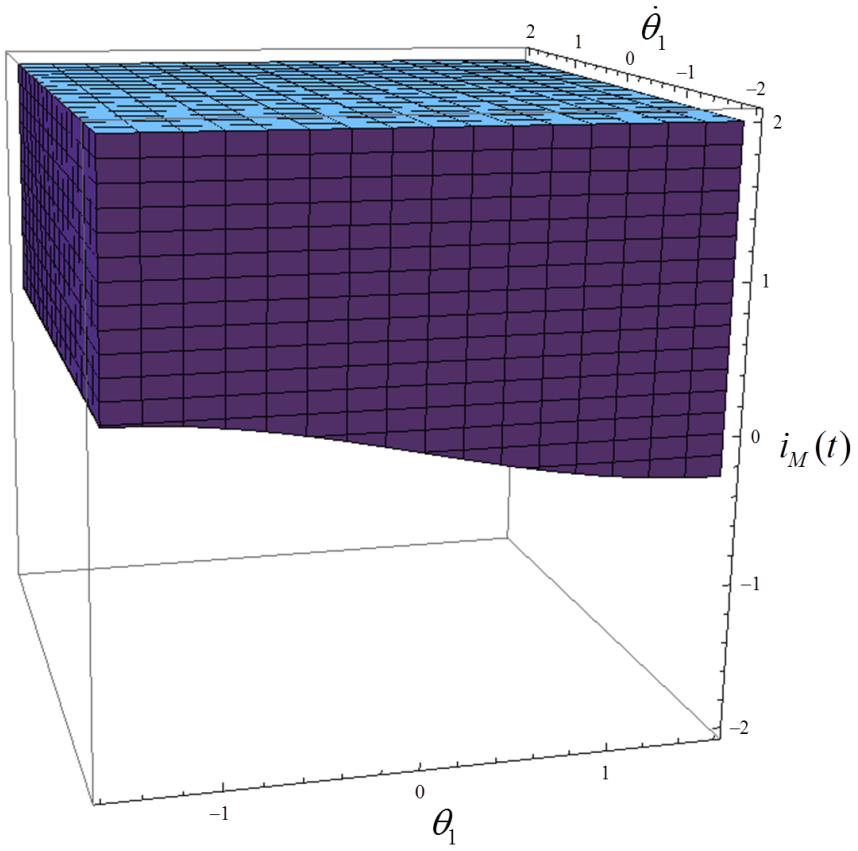

Figure 33: 3D plot of the variation of $\ddot{h}$ versus the state variables (the dark violet region indicates $\ddot{h} < 0$ which corresponds to the location of Zeno equilibrium points)

A 3D plot of the variation of $\ddot{h}$ versus the state variables for the double pendulum considered for the experiments has been shown in **Figure 33**. The dark violet region indicates $\ddot{h}$. It can be essentially inferred that stable Zeno equilibria will be seen for any value of θ_1 and $\dot{\theta}_1$ as long as the current is positive. Therefore, the stable equilibria of the system are the points where the state variable $i_M(t) > 0$, and it is irrespective of the sign of $\theta_2(t)$. Therefore, the existence of *Zeno periodic orbits* is validated.

In addition, this analysis motivates the introduction of completed hybrid systems since we will have Zeno behavior at a large collection of points. Now that the existence of *Zeno equilibrium* points is proven, the system can be taken past the *Zeno point* to define a vector field for the constrained system which is given by,

$$\begin{pmatrix} \dot{x} \\ \dot{i}_M \end{pmatrix} = f_P^{\lambda}(x) = f_P(x) + \begin{bmatrix} 0 \\ M(q)^{-1} dh(q)^T \lambda(q, \dot{q}) \\ 0 \end{bmatrix} \tag{39}$$

This completes the execution of *Zeno periodic orbits* in a hybrid system. The complete mathematical model including the calculations of the Lagrangian multiplier λ as well as the Langrangian vectors for the double pendulum problem is provided in **Appendix – B**. Also, in **Appendix – B**, we have shown the expression of $\ddot{h}$ from the mathematical model and represented the 3D plot of $\ddot{h}$ versus the state variables.

5.2 Experimentation of the Double Pendulum Model

Let us now look at the experimental procedure for the double pendulum. As explained in the previous section, the electrical circuit, primarily comprising a DC gearmotor, a circuit board and two encoders, is connected to the two solid links of the pendulum. In order to ensure safety during the operation of the setup, we will use an autotransformer to transfer power from the main AC power source to the board. The transformer helps in stepping down the source voltage from 110 V to 60 V which is sent to the full bridge rectifier built on the circuit board. This rectified voltage is sent in the form of input pulses to the motor. The motor is operated at a 90% duty cycle.

As mentioned previously, two balls (made of *high strength multipurpose neoprene rubber* and *polyurethane* materials) with different coefficients of restitution e are used in the mechanical stop to introduce non-plastic impacts in the system. In the following experiments, we have considered two cases:

Case 1: Experiments are conducted on the existing physical setup illustrated previously without any modifications.

Case 2: For this case, we have included a small design variation wherein an extra mass is added to the second link in the existing setup.

We will now examine the results obtained by using both the balls specified in each of the aforementioned cases.

5.2.1 Case 1: Existing Physical Setup

i) Ball-1 (High Strength Multipurpose Neoprene Rubber, $e = 0.15$): This experiment has been conducted on the existing physical setup which was explained in

the previous section (**Figure 29**). The coefficient of restitution, *e* for this ball has been determined to be 0.65. However, due to the energy dissipation at the gear train of the motor during impacts, we have approximated the value of *e* to 0.15. The proportional and derivative control parameters used in this case are the same as those used in the numerical simulation, i.e., $K_p = 3$ and $K_d = -1$.

The comparison of the time plots obtained from experimentation and simulation for Case 1 ($e = 0.15$) has been shown in **Figure 34**. The top half of the figure shows the plots for the angular position data for the top link ($\theta_1(t)$) while the bottom half shows the angular position data for the bottom link ($\theta_2(t)$) during the to-and-fro motion of the pendulum.

In case of the plot for $\theta_1(t)$, the waveform colored in *magenta* indicates the experimental data while the simulation data is indicated by different colors: *red squares*, *blue solid lines* and *black dotted lines*. The *red squares* indicate the impacts (or discrete transitions) occurring at the mechanical stop during each cycle of the pendulum motion. The "constrained" phase during each cycle of simulation is indicated by the *blue solid lines* while the *black dotted lines* until the occurrence of impacts indicate the "unconstrained" phase. In the plot for $\theta_2(t)$, the waveform colored in *magenta* shows the experimental data while the *black dotted lines* show the simulation data. It can be observed that the two sinusoidal waveforms are initially non-uniform and but soon attain a similar amplitude and frequency (stable periodic orbits), thereby giving us a good

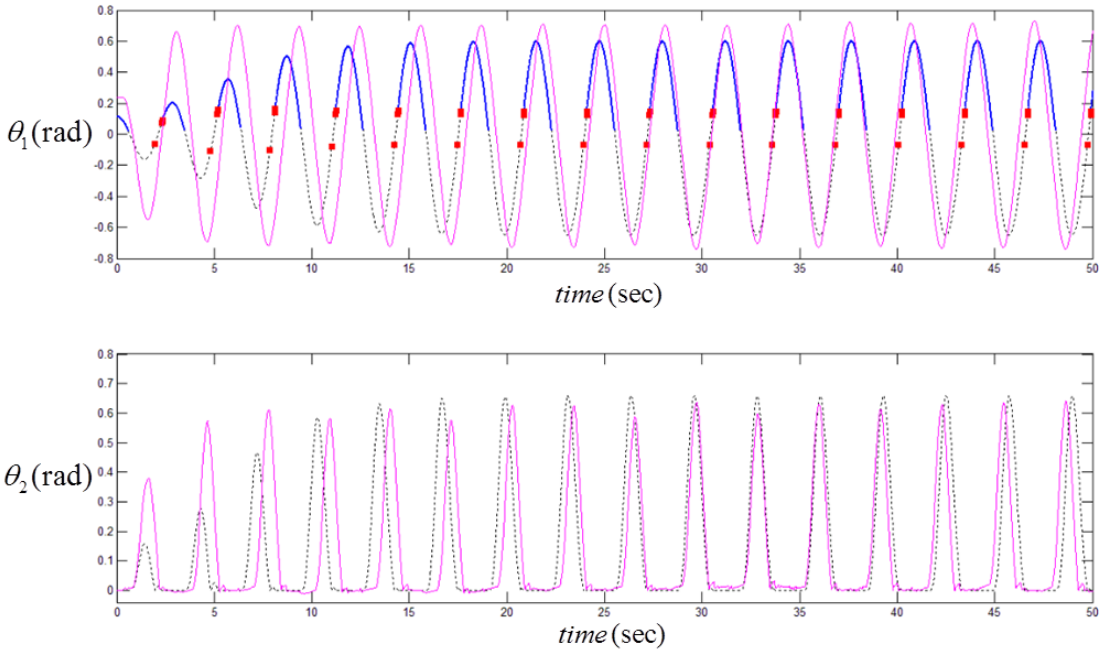

Figure 34: Comparison of the time plots of $\theta_1(t)$ and $\theta_2(t)$ for Case 1 ($e = 0.15$)

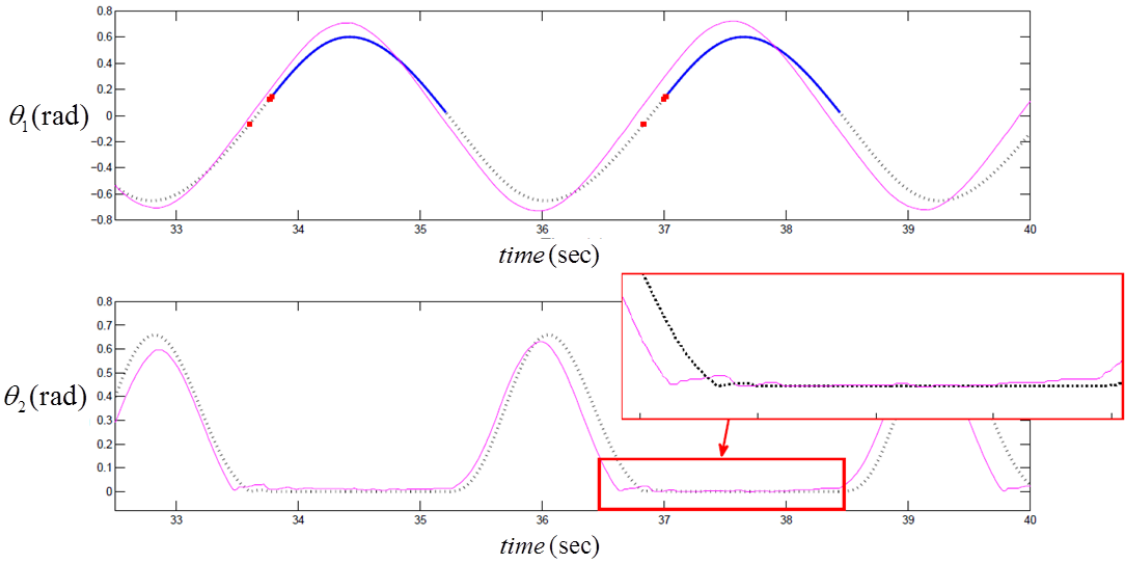

Figure 35: Closer view for comparison of observed impacts for Case 1 ($e = 0.15$)

match. A closer view of the impacts observed at the mechanical stop for Case 1 ($e = 0.15$) has been shown in **Figure 35**. It can be noticed that the bumps due to impacts at the mechanical stop and the subsequent constrained phase are closely matched in both the experiment and the simulation results. The simulation results presented here are comparable to those shown in [30].

We now present the phase portraits for the periodic orbits shown previously. **Figure 36 (a)** illustrates the phase portraits in the $(\theta_1, \dot{\theta}_1)$ plane. The *green* colored curve indicates the experimental data while the *blue* colored curve indicates the simulation data. Similarly, **Figure 36 (b)** shows the phase portraits in the $(\theta_2, \dot{\theta}_2)$ plane. Here, the experimental data is indicated by the *red dotted* curve while the *blue dotted* curve shows the simulation data. It can be noticed from the figure that the phase portraits in the $(\theta_1, \dot{\theta}_1)$ plane are *attractors* but do not match well at the corners. However, we are interested in Zeno behavior and impacts occurring at the mechanical stop at the second link. Also, the phase portraits in the $(\theta_2, \dot{\theta}_2)$ plane are *attractors* and match relatively well. This is particularly due to presence of time delay in inversion of the motor terminals which cannot be avoided. When the control input changes sign, then it fundamentally means that the voltage input given to the motor is inverted. But, there are some practical limits on achieving inversion of terminals immediately. One reason can be attributed to the time delays in switching of the MOSFETs. The other reason is the intentional 100ms delay which is being forced upon in order to protect the circuit from high energy inductance spikes coming from motor winding. Nevertheless,

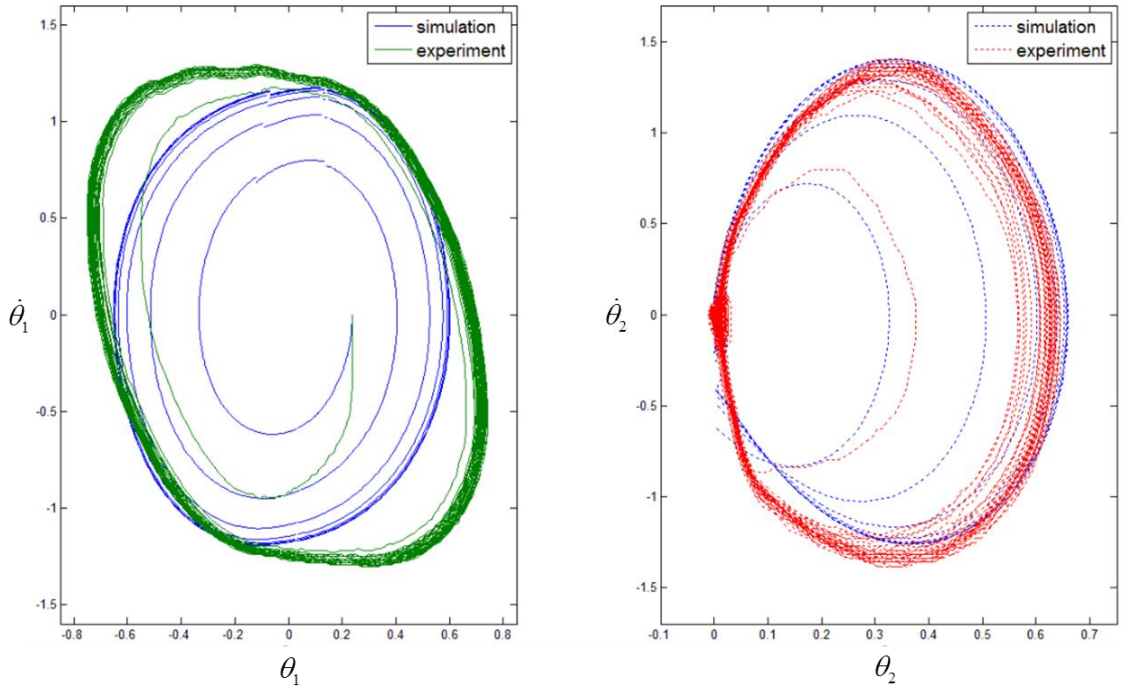

Figure 36: Phase portraits for periodic orbits in (a) $(\theta_1, \dot{\theta}_1)$ plane and (b) $(\theta_2, \dot{\theta}_2)$ plane for Case 1 (e = 0.15)

the differences in the behavior of top link, owing to time delay at the extreme ends, do not have any effect on the bottom link. This is primarily because $\theta_2 \approx 0$ when the top at the extreme ends. This ascertains the fact that we are able to achieve sustained Zeno behavior as well as stable periodic orbits with zeno in both experimentation and simulation.

ii) Ball-2 (Polyurethane, $e = 0.2$): The coefficient of restitution, e for this ball has been determined to be 0.7. However, due to the energy dissipation at the gear train of the motor during impacts, we have approximated the value of e to 0.2. The proportional

and derivative control parameters used here are the same as those used in the numerical simulation, i.e., $K_p = 3$ and $K_d = -1$.

The comparison of the time plots obtained from experimentation and simulation for Case 1 ($e = 0.2$) has been shown in **Figure 37**. The legends of the plots obtained can be understood in a similar fashion to those obtained with the previous ball for Case 1. A closer view of the impacts observed at the mechanical stop for Case 1 ($e = 0.2$) has

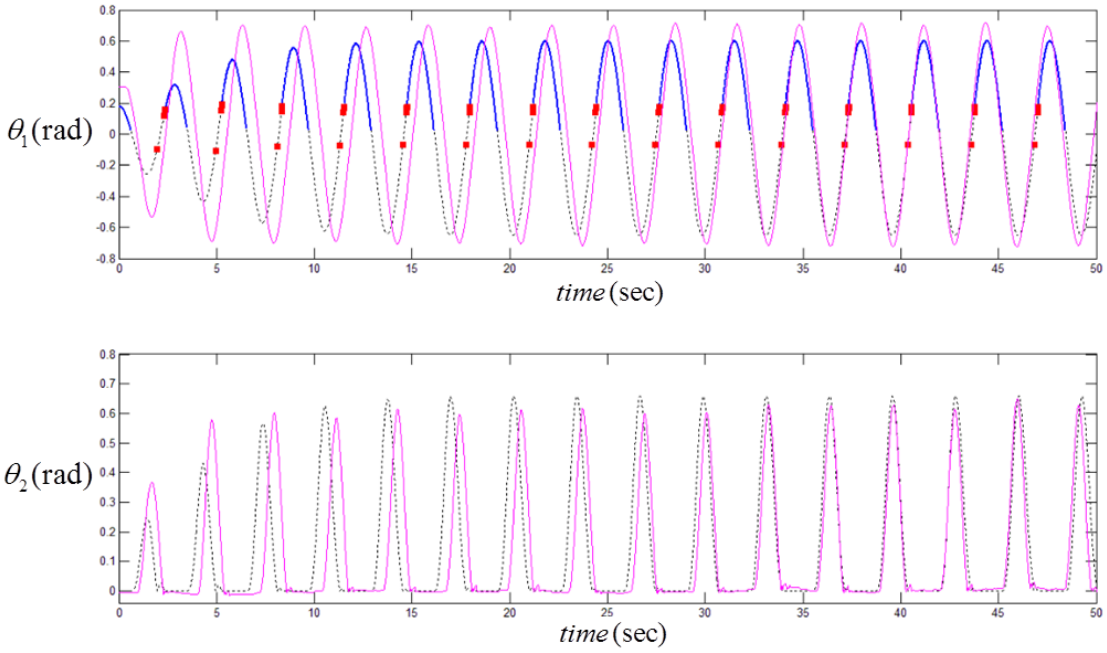

Figure 37: Comparison of the time plots of $\theta_1(t)$ and $\theta_2(t)$ for Case 1 ($e = 0.2$)

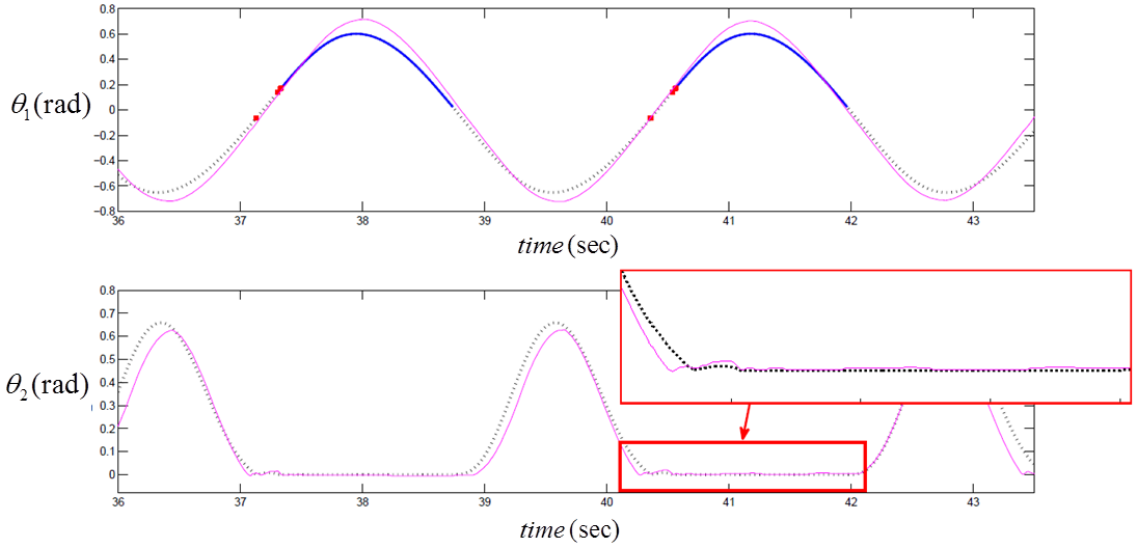

Figure 38: Closer view for comparison of observed impacts for Case 1 (e = 0.2)

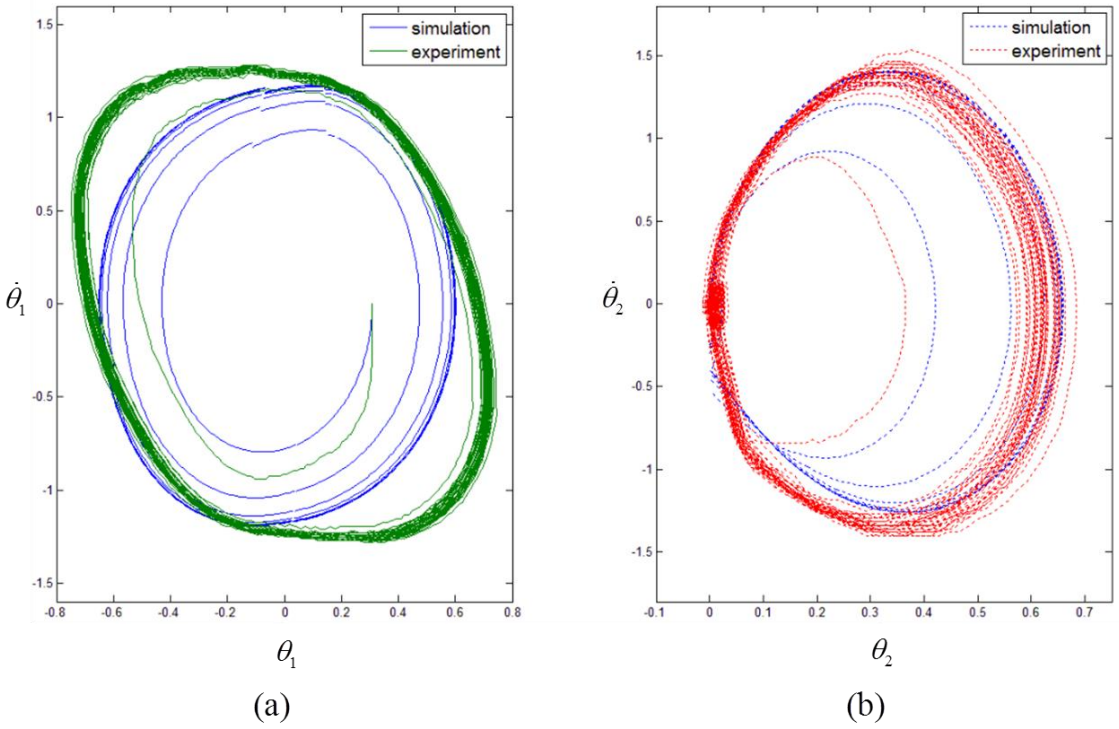

Figure 39: Phase portraits for periodic orbits in (a) $(\theta_1, \dot{\theta}_1)$ plane and (b) $(\theta_2, \dot{\theta}_2)$ plane for Case 1 (e = 0.2)

been shown in **Figure 38**. Since we are using a ball with a higher coefficient of restitution, the bumps at the mechanical stop are slightly more prominent in this case. Also, the constrained phase for both the simulation and the experiment are in good agreement with each other.

Let us now look at the phase portraits for the periodic orbits obtained using this ball (**Figure 39 (a)** and **(b)**). It has been ensured that similar initial conditions have been taken during both experimentation and simulation to get accurate phase portraits. Similar to what was observed in the case of the previous ball, although the phase portraits in the $(\theta_1, \dot{\theta}_1)$ plane do not match at the corners, the phase portraits in the $(\theta_2, \dot{\theta}_2)$ plane are in good agreement with each other.

In the next subsection, we will discuss the experimental results obtained with the modified physical setup while using the same balls which were used in the mechanical stop in Case 1.

5.2.2 Case 2: Extra Mass Added to the Second Link in the Physical Setup

i) Ball-1 (High Strength Multipurpose Neoprene Rubber, $e = 0.15$): This experiment has been conducted after attaching an extra mass to the physical setup. By doing so, we expect to observe pronounced zeno behavior while achieving stable periodic orbits. **Figure 40** shows the modified physical setup.

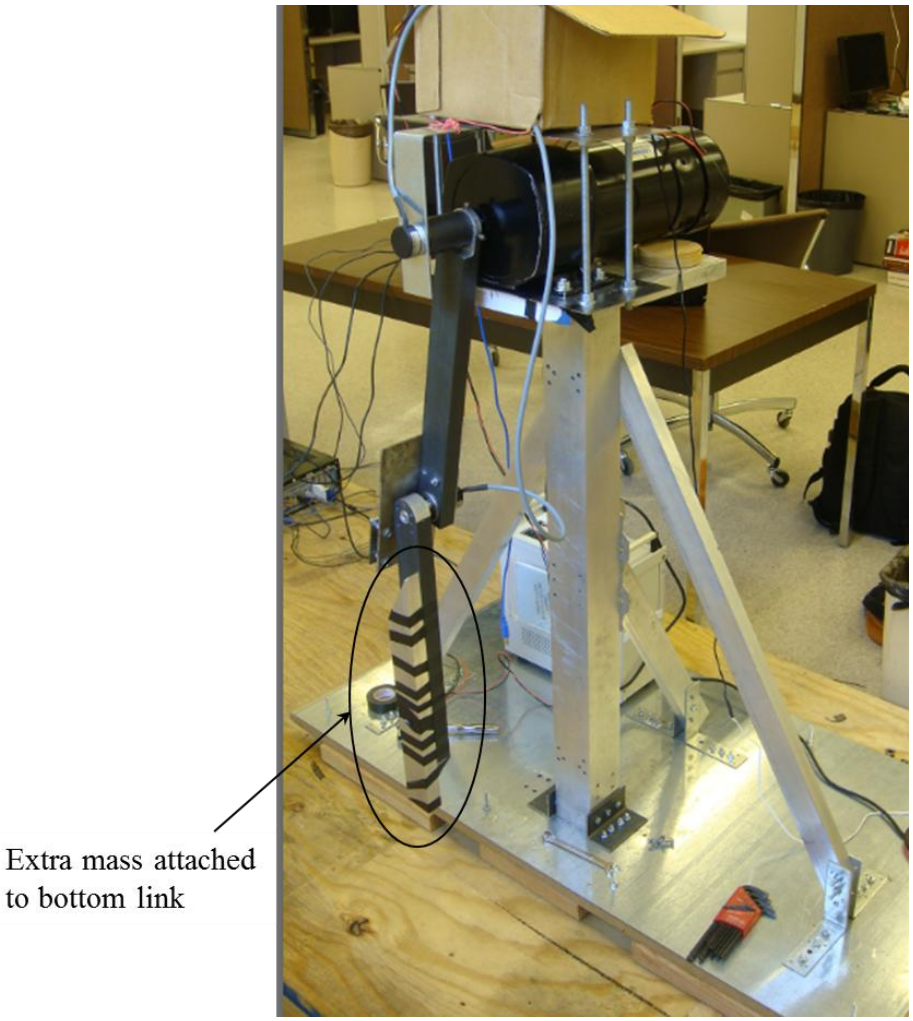

Figure 40: Modified physical setup of the double pendulum including the extra attached mass to the bottom link

The control parameters used for this case are kept the same as those used in Case 1, i.e., $K_p = 3$ and $K_d = -1$. The comparison of the time plots obtained from experimentation and simulation for Case 2 ($e = 0.15$) has been shown in **Figure 41**. The legends of the plots obtained can be understood in a similar fashion to those obtained with the previous ball for Case 1. A closer view of the impacts observed at the mechanical stop for this case has been shown in **Figure 42**. From this figure, it is clear that there is a noticeable variation in the bumps observed due to the non-plastic impacts occurring at the mechanical stop. This is due to the fact that the total inertia of the second link has increased due to the added mass resulting in pronounced impacts.

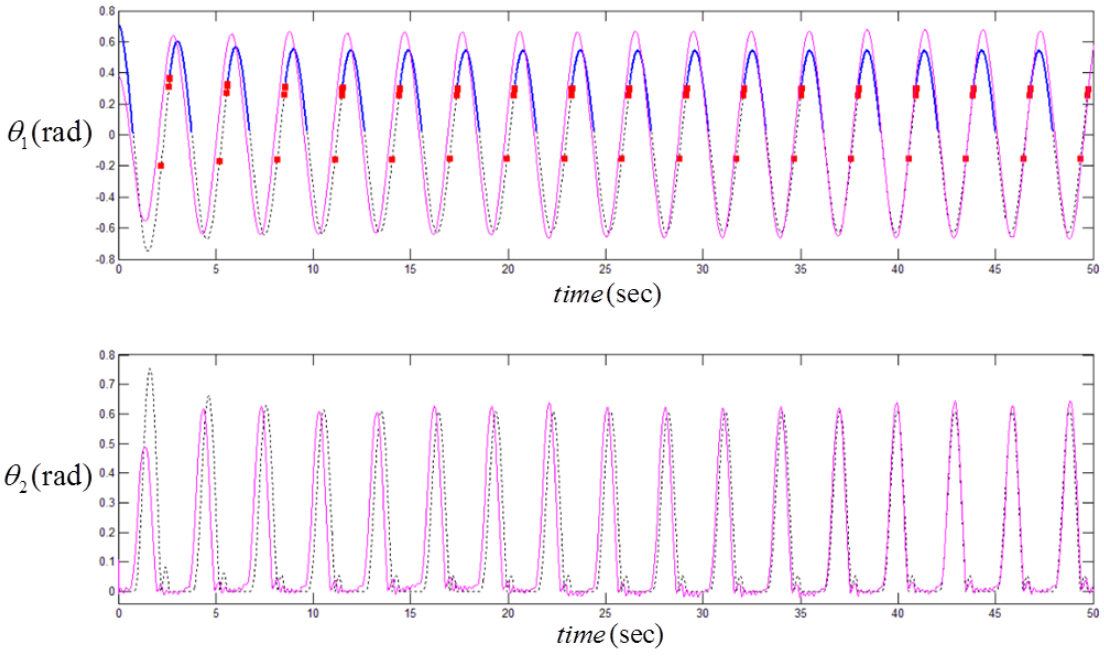

Figure 41: Comparison of the time plots of $\theta_1(t)$ and $\theta_2(t)$ for Case 2 ($e = 0.15$)

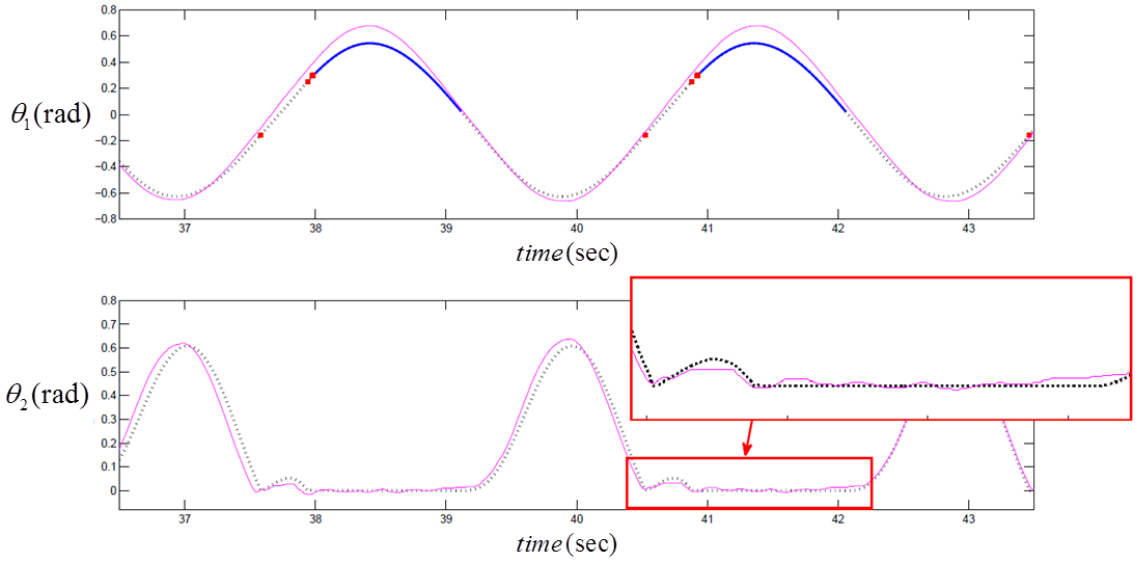

Figure 42: Closer view for comparison of observed impacts for Case 2 (e = 0.15)

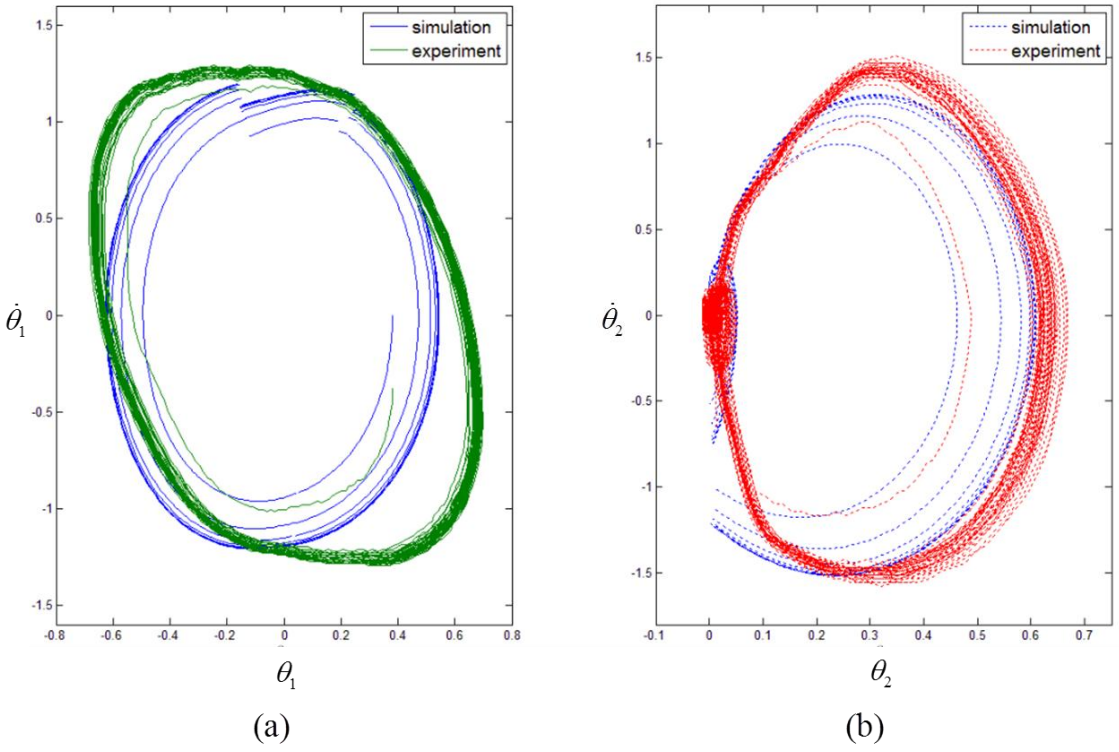

Figure 43: Phase portraits for periodic orbits in (a) $(\theta_1, \dot{\theta}_1)$ plane and (b) $(\theta_2, \dot{\theta}_2)$ plane for Case 2 (e = 0.15)

The phase portraits for the periodic orbits obtained in this case are shown in **Figure 43 (a)** and **(b)**. Although the phase portraits in the $(\theta_1, \dot{\theta}_1)$ plane do not match at the corners, the phase portraits in the $(\theta_2, \dot{\theta}_2)$ plane are in reasonably good agreement with each other.

ii) Ball-2 (Polyurethane, $e = 0.2$): In this case, a ball with a higher coefficient of restitution is used in the setup. As a result, we expect to achieve more pronounced impacts at the mechanical stop when compared with the impacts obtained with the previous ball. The comparison of the time plots obtained from experimentation and simulation for Case 2 ($e = 0.15$) has been shown in **Figure 44**. A closer view of the impacts observed at the mechanical stop for this case has been shown in **Figure 45**.

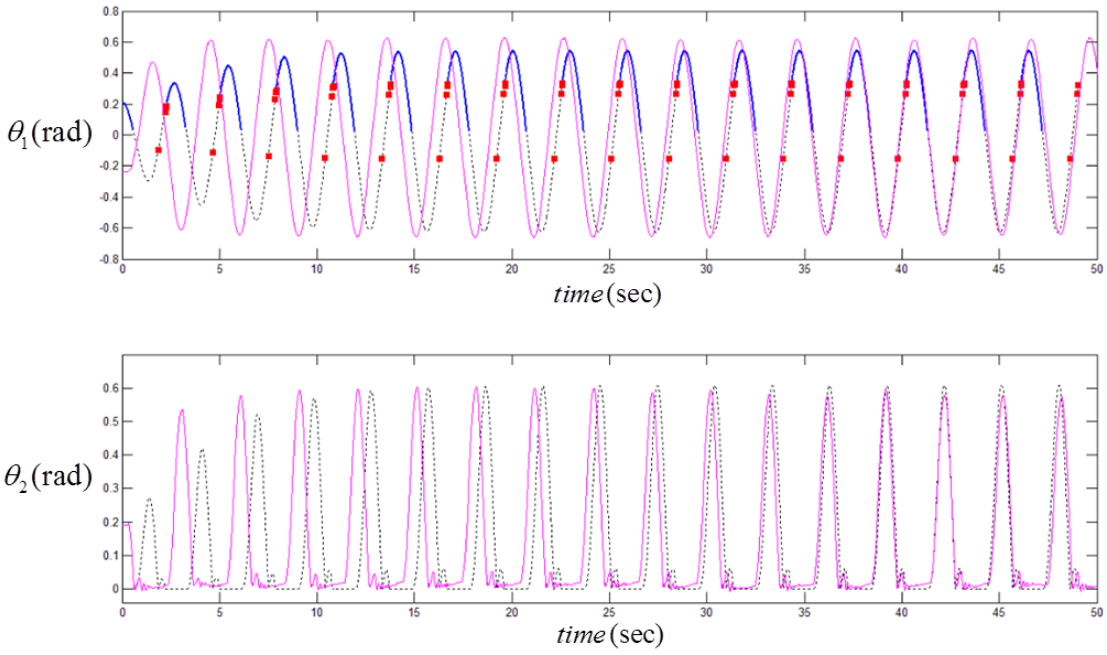

Figure 44: Comparison of the time plots of $\theta_1(t)$ and $\theta_2(t)$ for Case 2 ($e = 0.2$)

From this figure, it is clear that the bumps observed due to the impacts occurring at the mechanical stop are more pronounced compared to the previous cases. This is the result of the increased total inertia of the second link (due to the added mass).

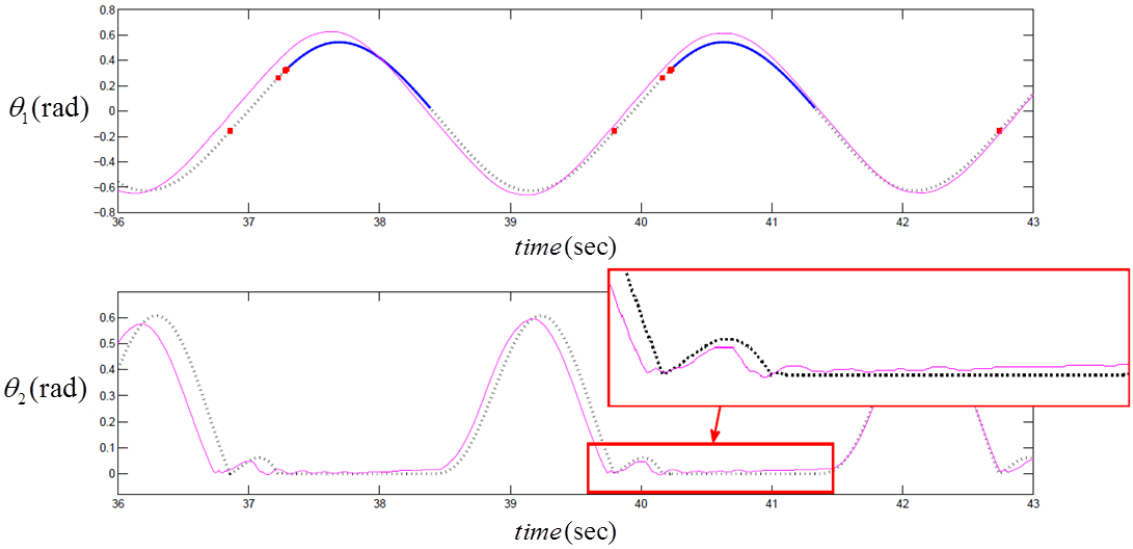

Figure 45: Closer view for comparison of observed impacts for Case 2 (e = 0.2)

The phase portraits for the periodic orbits obtained in this case are shown in **Figure 46 (a)** and **(b)**. Although the phase portraits in the $(\theta_1, \dot{\theta}_1)$ plane do not match at the corners, the phase portraits in the $(\theta_2, \dot{\theta}_2)$ plane are in reasonably good agreement with each other. An important observation to be noted is that the phase portrait obtained from simulation for Case 2 in the $(\theta_1, \dot{\theta}_1)$ plane (for both the balls used) shows evident discontinuities. This is due to the effect of pronounced impacts (or discrete transitions) occurring at the mechanical stop. On the contrary, the phase portrait obtained from experimentation looks smooth because it is averaged out several times.

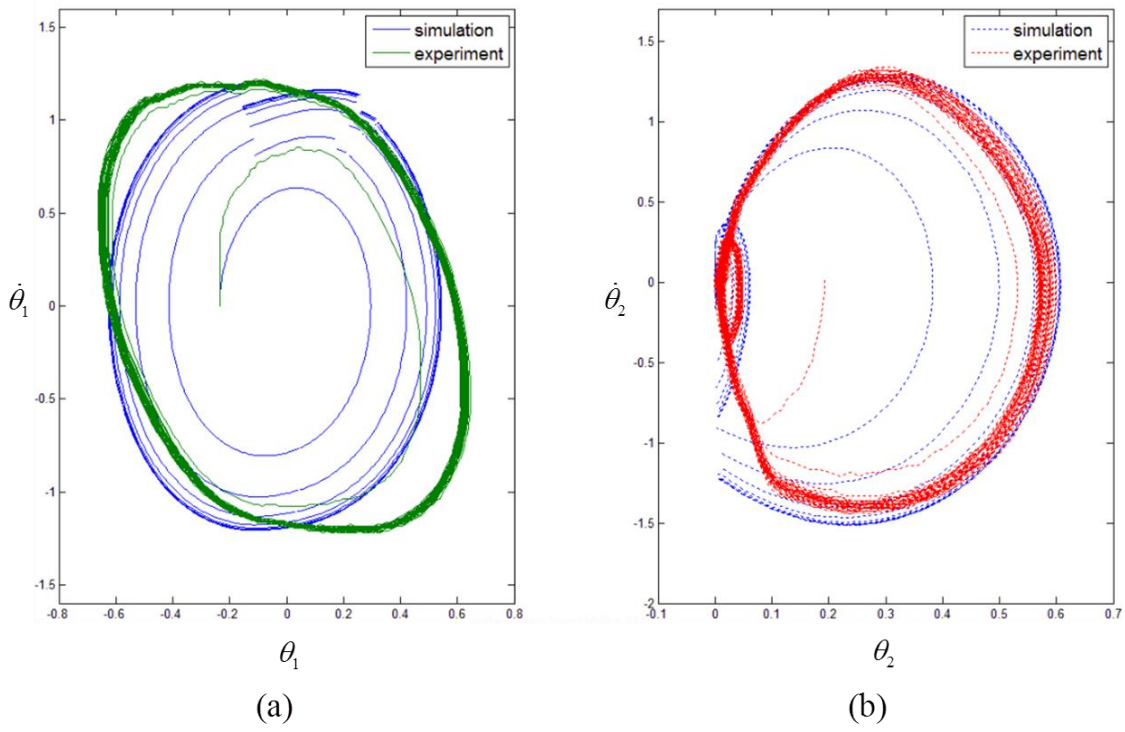

Figure 46: Phase portraits for periodic orbits in (a) $(\theta_1, \dot{\theta}_1)$ plane and (b) $(\theta_2, \dot{\theta}_2)$ plane for Case 2 (e = 0.2)

5.3 Conclusions

Two design problems of varying complexity – the walking bipedal robot and the double pendulum – have been considered in this thesis. The *design-by-function* concept has been implemented to determine the functionalities of each product during the design process. In the case of the walking bipedal robot, the walking gait and suitable actuation mechanisms have been established with the help of a detailed study on the walking gaits and actuation styles of earlier walking robots.

The constrained double pendulum problem has been provided as a suitable example of a Lagrangian hybrid system comprising both continuous-time and discrete-time dynamic behavior. We have explained the definitions and sufficient conditions necessary to achieve zeno behavior and zeno executions. Also, we have presented the procedure to formally and practically complete a hybrid system by a finite truncation of an infinite number of zeno executions without affecting the quality of the solutions.

The stability of a Zeno equilibrium point $(q^*, \dot{q}^*)$ can also be perceived as stability of the *unilaterally constrained* motion on the surface $h^{-1}(0)$ under small perturbations that violate the constraint, with guaranteed finite-time convergence back to the constraint surface via a Zeno hybrid execution with an infinite number of collisions. The equivalence of the conditions $\ddot{h}(q^*, \dot{q}^*) < 0$ and $\lambda(q^*, \dot{q}^*) > 0$ implies that the constrained motion is proven to be stable at a zeno point $x^* = (q^*, \dot{q}^*)$, if and only if the constrained dynamical system is consistent at x^*, i.e., it satisfies $\lambda(q^*, \dot{q}^*) > 0$.

In order to prove the existence of zeno in hybrid systems and to achieve zeno periodic orbits, we have developed a numerical simulation and a physical setup of the double pendulum with a mechanical stop to introduce non-plastic impacts. The mathematical model used for the numerical simulation has modeled all the parameters of the physical setup of the double pendulum. Also, it models the guard, impact equations and the corresponding reset map, thereby facilitating simulation of Zeno behavior in Lagrangian hybrid systems.

The physical setup of the double pendulum is similar to a bipedal robot as the "constrained" phase during pendulum motion is similar to the *knee-lock* phenomenon in robots while the occurrence of multiple impacts during each cycle of motion is analogous to *knee-bounce*. Two balls of different coefficients of restitution have been used in the mechanical stop to vary the degree of non-plasticity of impacts. The resulting effect on zeno behavior has also been observed in the double pendulum setup. Ultimately, we have been able to achieve closely comparable results using both, the mathematical model and the physical setup. This determines the fact it is possible to observe stable Zeno executions in practice. Thereby, we have essentially established the similarity between Zeno behavior as observed in hybrid systems and the phenomena of *knee-lock* and *knee-bounce* in bipedal walking robots.

The product design procedure and *design-for-validation* methodologies have been implemented successfully for both these design problems with equal effectiveness. Also, we have been able to integrate both product design and control theory in the process of developing and conducting experiments on the double pendulum.

REFERENCES

[1] G. Pahl and W. Beitz, *Engineering Design: A systematic Approach*, 2nd ed. London, UK: Springer-Verlag, 1996.

[2] S. C. Johnson and R. W. Butler, "Design for Validation," NASA Langley Technical Report Server 2003.

[3] Y.-M. Deng, S. B. Tor, and G. A. Britton, "A Computerized Design Environment for Functional Modeling of Mechanical Products," in *Proc. 5th ACM Symposium on Solid Modeling and Applications*. Ann Arbor, MI, 1999, pp. 1-12.

[4] R. Goebel, R. Sanfelice, and A. Teel, "Hybrid Dynamical Systems," *IEEE Control Systems Magazine*, vol. 29, pp. 28-93, 2009.

[5] P. Sardain, M. Rostami, and G. Bessonnet, "An Anthropomorphic Biped Robot: Dynamic Concepts and Technological Design," *IEEE Transactions on Systems, Man and Cybernetics, Part A: Systems and Humans*, vol. 28, pp. 823-838, 1998.

[6] L. Perko, *Differential Equations and Dynamical Systems*, 3rd ed. New York: Springer-Verlag, 2006.

[7] J. Doyle, B. Francis, and A. Tannenbaum, *Feedback Control Theory*. New York: Macmillan Publishing Company, 1990.

[8] E. K. Antonsson and K. N. Otto, "Imprecision in Engineering Design," *Journal of Vibration and Acoustics*, vol. 117, pp. 25-32, 1995.

[9] N. Cross, *Engineering Design Methods - Strategies for Product Design*, 3rd ed. Chichester, UK: John Wiley & Sons, 2000.

[10] V. Hubka, *Theory of Technical Systems: A Total Concept Theory for Engineering Design*. Berlin: Springer-Verlag, 1988.

[11] E. N. Baylin, *Functional Modeling of Systems*. New York: Gordon and Breach Science Publishers, Inc., 1990.

[12] Y. Iwasaki, M. Vescovi, R. Fikes, and B. Chandrasekaran, "Causal Functional Representation Language with Behavior-based Semantics," *Applied Artificial Intelligence: An International Journal*, vol. 9, pp. 5-31, 1995.

[13] Y. Akao, *Quality Function Deployment: Integrating Customer Requirements into Product Design*. Cambridge, MA: Productivity Press, 1990.

[14] E. R. Westervelt, J. W. Grizzle, C. Chevallereau, J. H. Choi, and B. Morris, *Feedback Control of Dynamic Bipedal Robot Locomotion*, 1st ed. New York: Taylor & Francis Group, LLC, 2007.

[15] V. V. Madadi and S. Tosunoglu, "Design and Development of a Biped Robot," in *Proc. International Symposium on Computational Intelligence in Robotics and Automation (CIRA)*. Jacksonville, FL, 2007, pp. 243-247.

[16] T. D. White and P. A. Folkens, *The Human Bone Manual*. London, UK: Elsevier Academic Press, 2005.

[17] H. Tingshu, L. Zongli, F. A. Mark, and E. A. Paul, "Human Gait Modeling: Dealing with Holonomic Constraints," in *Proc. American Control Conference*, vol. 3. Boston, MA, 2008, pp. 2296-2301.

[18] J. W. Grizzle, G. Abba, and F. Plestan, "Asymptotically Stable Walking for Biped Robots: Analysis via Systems with Impulse Effects," *IEEE Transactions on Automatic Control*, vol. 46, pp. 51-64, 2001.

[19] T. McGeer, "Passive Dynamic Walking," *The International Journal of Robotics Research*, vol. 9, pp. 62-82, 1990.

[20] T. McGeer, "Passive Walking with Knees," in *Proc. IEEE International Conference on Robotics and Automation*. Cincinnati, OH, 1990, vol. 3, pp. 1640-1645.

[21] S. Kajita, T. Yamaura, and A. Kobayashi, "Dynamic Walking Control of a Biped Robot Along a Potential Energy Conserving Orbit," *IEEE Transactions on Robotics and Automation*, vol. 8, pp. 431-438, 1992.

[22] H. Miura and I. Shimoyama, "Dynamic Walk of a Biped," *The International Journal of Robotics Research*, vol. 3, pp. 60-74, 1984.

[23] J. Furusho and A. Sano, "Sensor-Based Control of a Nine-Link Biped," *The International Journal of Robotics Research*, vol. 9, pp. 83-98, 1990.

[24] C.-L. Shih, W. A. Gruver, and T.-T. Lee, "Inverse Kinematics and Inverse Dynamics for Control of a Biped Walking Machine," *Journal of Robotic Systems*, vol. 10, pp. 531-555, 1993.

[25] B. Espiau, "BIP: A Joint Project for the Development of an Anthropomorphic Biped Robot," in *Proc. 8th International Conference on Advanced Robotics (ICAR)*. Monterey, CA, 1997, pp. 267-272.

[26] T. A. McMahon, "Mechanics of Locomotion," *The International Journal of Robotics Research*, vol. 3, pp. 4-28, 1984.

[27] J. W. Grizzle and E. R. Westervelt, "Hybrid Zero Dynamics of Planar Bipedal Walking," 2010.

[28] E. R. Westervelt, J. W. Grizzle, and D. E. Koditschek, "Hybrid Zero Dynamics of Planar Biped Walkers," *IEEE Transactions on Automatic Control*, vol. 48, pp. 42-56, 2003.

[29] A. D. Ames, "A Categorical Theory of Hybrid Systems," Ph. D. dissertation, University of California, Berkeley, CA, 2006.

[30] Y. Or and A. Ames, "Existence of Periodic Orbits with Zeno Behavior in Completed Lagrangian Hybrid Systems," in *Proc. Hybrid Systems: Computation and Control*, R. Majumdar and P. Tabuada, Eds.: Springer Berlin, 2009, vol. 5469, pp. 291-305.

[31] G. Rafal, H. Joao, R. T. Andrew, C. Chaohong, and S. Ricardo, "Hybrid Systems: Generalized Solutions and Robust Stability," in *Proc. IFAC Symposium on Nonlinear Control Systems*. Stuttgart, Germany, 2004, pp. 1-12.

[32] Y. Or and A. D. Ames, "Formal and Practical Completion of Lagrangian Hybrid Systems," in *Proc. American Control Conference (ACC)*. St. Louis, MO, 2009, pp. 3624-3631.

[33] M. Heymann, L. Feng, G. Meyer, and S. Resmerita, "Analysis of Zeno Behaviors in a Class of Hybrid Systems," *IEEE Transactions on Automatic Control*, vol. 50, pp. 376-383, 2005.

[34] A. D. Ames, A. Abate, and S. Sastry, "Sufficient Conditions for the Existence of Zeno Behavior," in *Proc. 44th IEEE Conference on Decision and Control and European Control Conference (CDC-ECC)*. Seville, Spain, 2005, pp. 696-701.

[35] A. D. Ames, A. Abate, and S. Sastry, "Sufficient Conditions for the Existence of Zeno Behavior in a Class of Nonlinear Hybrid Systems via Constant Approximations," in *Proc. 46th IEEE Conference on Decision and Control*. New Orleans, LA, 2007, pp. 4033-4038.

[36] A. Lamperski and A. Ames, "Sufficient Conditions for Zeno Behavior in Lagrangian Hybrid Systems," in *Proc. Hybrid Systems: Computation and Control*, M. Egerstedt and B. Mishra, Eds.: Springer Berlin / Heidelberg, 2008, vol. 4981, pp. 622-625.

[37] C. C. de Wit, B. Siciliano, and G. Bastin, *Theory of Robot Control*, 2nd ed. London, UK: Springer-Verlag, 1996.

[38] Naval Biodynamics Laboratory, "Anthropometry and Mass Distribution for Human Analogues." New Orleans, LA, 1988, vol. 1, pp. 5-31.

[39] National Aeronautics and Space Administration, "Man-Systems Integration Standards." Houston, TX, 1995, vol. 1, pp. 32-79.

[40] D. Winter, *Biomechanics and Motor Control of Human Movement*, 3rd ed. Hoboken, NJ: John Wiley & Sons, 2005.

[41] E&ESP, "Self-Aligning Couplers," vol. 2009. Warren, MI: E&E Special Products, 2009.

[42] Moog, "BN28 Silencer Series Brushless DC Motors," vol. 2009. Beaumont, TX: Moog Inc., 2009.

[43] K. Trifonov and S. Hashimoto, "Active Knee-lock Release for Passive-Dynamic Walking Machines," in *Proc. IEEE International Conference on Robotics and Biomimetics (ROBIO)*. Nice, France, 2007, pp. 958-963.

[44] A. Ames, R. Sinnet, and E. Wendel, "Three-Dimensional Kneed Bipedal Walking: A Hybrid Geometric Approach," in *Proc. Hybrid Systems: Computation and Control*, vol. 5469, *Lecture Notes in Computer Science*, R. Majumdar and P. Tabuada, Eds.: Springer Berlin / Heidelberg, 2009, pp. 16-30.

[45] S. Collins, M. Wisse, and A. Ruina, "A Three-Dimensional Passive-Dynamic Walking Robot with Two Legs and Knees," *The International Journal of Robotics Research*, vol. 20, pp. 607-615, 2001.

[46] Y. Or and A. D. Ames, "Existence of Periodic Orbits in Completed Lagrangian Hybrid Systems with Non-Plastic Collisions," California Institute of Technology, Pasadena, CA 2008.

[47] Y. Or and A. Ames, "Stability and Completion of Zeno Equilibria in Lagrangian Hybrid Systems," *IEEE Transactions on Automatic Control*, (in press).

APPENDIX A

Table 1: Bill of Materials (BOM) for building the physical model of the Double Pendulum

S. No.	***Part Name***	***Material***	***Specs / Dimensions***	***Quantity***
1	Ball bearing / rotary joint	Steel	Bearing trade no. 7612 / .75" ID / 1.75" OD	1
2	DC motor		3/4" dia / 822 in-lbs / 5 A / 33 RPM	1
3	Incremental Encoder (Two set screws included)		Miniature optical / 8000 rpm / 2000 resolution / 1/4" dia	2
4	Clamp-On Shaft Coupling	Steel	3/4" x 0.235" bore / 1133 in-lbs	1
5	Pendulum links	Multipurpose Aluminum (Anodized)	1" x 2" x 36"	1
6	Steel base plate	Steel 4140	24" x 48" x 0.125 in	1
7	Side, back supports	Aluminum	1" x 2" x 36"	3
8	Main support	Aluminum	3" x 3" x 36"	1
9	Support plate for motor	Aluminum	10" x 12" x 1"	1
10	Ball-type1	High-Strength Multipurpose Neoprene Rubber	1" dia / tensile strength 1500 psi / 55A durometer	Pack of 10
	Ball-type2	Ultra-Strength Silicone Rubber	1" dia / tensile strength 2000 psi / 70A durometer	Pack of 5
	Ball-type3	Polyurethane	1" dia / tensile strength 6500 psi / 95A durometer	1
	Ball-type4	Abrasion-Resistant Natural Gum Rubber	1" dia / tensile strength 2700 psi / 50A durometer	Pack of 10
11	Mechanical Stop (Plate)	Steel	8" x 8" x 0.125"	1
12	Wooden blocks	Treated Lumber	11.5” x 3.5” x 1.5”	13

Table 2: Bill of Materials (BOM) for building the circuit board

S. No.	***Part Name***	***Specifications***	***Quantity***
1	Printed Circuit boards (PCBs)		3
2	Bridge Rectifier	400V, 25A	1
3	Bridge Rectifier	100V, 6A	1
4	Capacitor	150V, 10A ripple current, 4700μF	3
5	Capacitor	25V, 100μF	3
6	Isolation Transformer	110V to 12V	1
7	Linear Regulator	2N3055	1
8	Linear Regulator	LM7805	1
9	Atmel AtMEGA128 microcontroller	Supply 4.5V to 5.5V, 128KB memory	1
10	BU407 Transistor	NPN, 150V, 7A, 60W	10
11	Power MOSFET-type1	P-channel, 150V	2
12	Power MOSFET-type2	N-channel, 150V	2
13	Heat sinks for MOSFETs		4
14	Fuse	250V AC, 5A	1
15	0603 Resistor Pack		1 pack
	0805 Resistor Pack		1 pack
	1206 Resistor Pack		1 pack
	2512 Resistor Pack		1 pack
16	D-25 connector	Male & female	2
17	Power Connector with cord	110V AC	1

APPENDIX B

1. The Mathematica file including the mathematical model used for numerical simulation of Zeno behavior for Case 2 ($e = 0.2$) has been provided here.

2. The expression for $\ddot{h}$ and the 3D plot of $\ddot{h}$ versus the state variables is also provided.

2-Link Locking Pendulum

```
Import["C:\Users\Bhargav\Desktop\Research Project\New
   Pendulum case 6 - Amber ball & Added mass\Robotlinks.m"]
SetDirectory["C:\Users\Bhargav\Desktop\Research Project\New
    Pendulum case 6 - Amber ball & Added mass"];
```

- **Functions to take Jacobians**

```
Clear[DJacobian];
DJacobian[h_, q_] :=
  Table[∂Transpose[q] Flatten[{h}][[i]], {i, 1, Length[Flatten[{h}]]}];
```

- **Substitutions**

$$\text{constsubs} = \left\{\ell_1 \to 18,\ \ell_2 \to 18,\ m_1 \to \frac{1325}{100},\ m_2 \to \frac{355+290}{100},\ g \to \frac{3217}{100}12,\ e \to \frac{2000}{10\,000}\right\};$$

```
statesubs =
  {θ1[t] → x[1], θ2[t] → x[2], θ1'[t] → x[3], θ2'[t] → x[4], Ia[t] → x[5]};
```

- **Compute the equations of motion and reset map**

- **Declare variables:**

```
q = Table[{θi[t]}, {i, 1, 2}];
dq = D[q, t];
```

- **Define twists:**

```
ξ0 = {0, 0, 0, 0, 0, 0}
ξθ1 = RevoluteTwist[{0, 0, 0}, {1, 0, 0}]
ξθ2 = RevoluteTwist[{0, 0, -ℓ1}, {1, 0, 0}]
```

```
{0, 0, 0, 0, 0, 0}
```

```
{0, 0, 0, 1, 0, 0}
```

```
{0, -ℓ1, 0, 1, 0, 0}
```

- **Define the initial configuration:**

$$g_{sl_1}[0] = \text{RPToHomogeneous}\left[\text{IdentityMatrix}[3], \left\{0, 0, \frac{-625\,\ell_1}{2650}\right\}\right]$$

$$g_{sl_2}[0] = \text{RPToHomogeneous}\left[\text{IdentityMatrix}[3], \left\{0, 0, -\ell_1 - \frac{\ell_2}{2} - 2\right\}\right]$$

$$\left\{\{1, 0, 0, 0\}, \{0, 1, 0, 0\}, \left\{0, 0, 1, -\frac{25\,\ell_1}{106}\right\}, \{0, 0, 0, 1\}\right\}$$

$$\left\{\{1, 0, 0, 0\}, \{0, 1, 0, 0\}, \left\{0, 0, 1, -2 - \ell_1 - \frac{\ell_2}{2}\right\}, \{0, 0, 0, 1\}\right\}$$

- **Calculate the Body Jacobian of each mass:**

$$\mathcal{J}_1 = \text{FullSimplify}[\text{BodyJacobian}[\{\xi_{\theta 1}, \theta_1[t]\}, \{\xi_0, \theta_2[t]\}, g_{sl_1}[0]]];$$
$$\mathcal{J}_2 = \text{FullSimplify}[\text{BodyJacobian}[\{\xi_{\theta 1}, \theta_1[t]\}, \{\xi_{\theta 2}, \theta_2[t]\}, g_{sl_2}[0]]];$$

- **Define the inertia matrices for each mass:**

$$\mathcal{M}_1 = \left\{\{m_1, 0, 0, 0, 0, 0\},\right.$$
$$\{0, m_1, 0, 0, 0, 0\},$$
$$\{0, 0, m_1, 0, 0, 0\},$$
$$\left\{0, 0, 0, \left(20\,200 + \frac{700}{100}\left(\frac{625\,\ell_1}{2650}\right)^2\right) + \left(\frac{350\left(\ell_1^2 + 4\right)}{1200} + \frac{350}{100}\left(8 - \frac{625\,\ell_1}{2650}\right)^2\right) + \right.$$
$$\left(\frac{130}{200} + \frac{130}{100}\left(\frac{625\,\ell_1}{2650}\right)^2\right) + \left(\frac{95}{1200}\left(8^2 + \frac{125^2}{1000^2}\right) + \frac{95}{100}\left(16 - \frac{625\,\ell_1}{2650}\right)^2\right) +$$
$$\left.\left(\frac{50}{1200}\left(4^2 + \frac{125^2}{1000^2}\right) + \frac{50}{100}\left(17 - \frac{625\,\ell_1}{2650}\right)^2\right), 0, 0\right\},$$
$$\{0, 0, 0, 0, 0, 0\},$$
$$\left.\{0, 0, 0, 0, 0, 0\}\right\}$$

$$\left\{\{m_1, 0, 0, 0, 0, 0\}, \{0, m_1, 0, 0, 0, 0\}, \{0, 0, m_1, 0, 0, 0\},\right.$$
$$\left\{0, 0, 0, \frac{310\,370\,077}{15\,360} + \frac{7}{2}\left(8 - \frac{25\,\ell_1}{106}\right)^2 + \frac{19}{20}\left(16 - \frac{25\,\ell_1}{106}\right)^2 + \frac{1}{2}\left(17 - \frac{25\,\ell_1}{106}\right)^2 + \right.$$
$$\left.\left.\frac{10\,375\,\ell_1^2}{22\,472} + \frac{7}{24}\left(4 + \ell_1^2\right), 0, 0\right\}, \{0, 0, 0, 0, 0, 0\}, \{0, 0, 0, 0, 0, 0\}\right\}$$

```
(*M1= {DiagonalMatrix[{m1,m1,m1}],DiagonalMatrix[{0,0,0}],
   DiagonalMatrix[{0,0,0}], DiagonalMatrix[{{20200+525ℓ1^2/300+m1 525^2 ℓ1^2/1914^2,0,0}}];*)
M2 = DiagonalMatrix[{m2, m2, m2, (355 (ℓ2^2 + 4))/1200 + 355/100 4 + (290 (15^2 + 1))/1200 + 290/100 4,
   (355 (ℓ2^2 + 1))/1200 + 355/100 4 + (290 (15^2 + 1))/1200 + 290/100 4, 0}]
{{m2, 0, 0, 0, 0, 0}, {0, m2, 0, 0, 0, 0},
 {0, 0, m2, 0, 0, 0}, {0, 0, 0, 9737/120 + 71/240 (4 + ℓ2^2), 0, 0},
 {0, 0, 0, 0, 965/12 + 71/240 (1 + ℓ2^2), 0}, {0, 0, 0, 0, 0, 0}}
```

- **Caculate the D matrix for impact:**

```
D = FullSimplify[Sum_{i=1}^{2} Transpose[Ji].Mi.Ji]
{{{ℓ1 (-3 288 120 + (138 701 + 7500 m1) ℓ1)/134 832 +
    (321 048 221 + 4544 ℓ2^2)/15 360 + 1/4 m2 (4 ℓ1^2 + 4 Cos[θ2[t]] ℓ1 (4 + ℓ2) + (4 + ℓ2)^2),
   1/240 (19 758 + 71 ℓ2^2 + 60 m2 (4 + ℓ2) (4 + 2 Cos[θ2[t]] ℓ1 + ℓ2))},
  {1/240 (19 758 + 71 ℓ2^2 + 60 m2 (4 + ℓ2) (4 + 2 Cos[θ2[t]] ℓ1 + ℓ2)),
   1/240 (19 758 + 71 ℓ2^2 + 60 m2 (4 + ℓ2)^2)}}
{{1/3 (1/4 m1 ℓ1^2 + m2 (3 ℓ1^2 + 3 Cos[θ2[t]] ℓ1 ℓ2 + 3/4 ℓ2^2)), 1/6 m2 ℓ2 (3 Cos[θ2[t]] ℓ1 + 2 ℓ2)},
 {1/6 m2 ℓ2 (3 Cos[θ2[t]] ℓ1 + 2 ℓ2), 1/3 m2 ℓ2^2}}
{{1/3 (1/4 m1 ℓ1^2 + m2 (3 ℓ1^2 + 3 Cos[θ2[t]] ℓ1 ℓ2 + (3 ℓ2^2)/4)), 1/6 m2 ℓ2 (3 Cos[θ2[t]] ℓ1 + 2 ℓ2)},
 {1/6 m2 ℓ2 (3 Cos[θ2[t]] ℓ1 + 2 ℓ2), 1/3 m2 ℓ2^2}}
```

- **Calculate the Coriolis matrix:**

```
C = InertiaToCoriolis[𝒟, Flatten[q], Flatten[dq]] // FullSimplify
```

$$\left\{\left\{-\frac{1}{2}\,\text{Sin}[\theta_2[t]]\,m_2\,\ell_1\,(4+\ell_2)\,(\theta_2)'[t],\right.\right.$$
$$\left.-\frac{1}{2}\,\text{Sin}[\theta_2[t]]\,m_2\,\ell_1\,(4+\ell_2)\,((\theta_1)'[t]+(\theta_2)'[t])\right\},$$
$$\left.\left\{\frac{1}{2}\,\text{Sin}[\theta_2[t]]\,m_2\,\ell_1\,(4+\ell_2)\,(\theta_1)'[t],\,0\right\}\right\}$$

- **Calculate the G vector:**

```
g1[θ] = ForwardKinematics[{ξθ1, θ1[t]}, gsl1[0]];
g2[θ] = ForwardKinematics[{ξθ1, θ1[t]}, {ξθ2, θ2[t]}, gsl2[0]];
For[i = 1, i ≤ 2, i++, hi = RigidPosition[gi[θ]][[3]] // FullSimplify];
V = Sum[mi g hi, {i, 2}] // FullSimplify;
G = {(∂#1 V &) /@ q} // Transpose // FullSimplify
```

$$\left\{\left\{\frac{1}{106}\,g\,(25\,\text{Sin}[\theta_1[t]]\,m_1\,\ell_1+53\,m_2\,(2\,\text{Sin}[\theta_1[t]]\,\ell_1+\text{Sin}[\theta_1[t]+\theta_2[t]]\,(4+\ell_2)))\right\},\right.$$
$$\left.\left\{\frac{1}{2}\,g\,\text{Sin}[\theta_1[t]+\theta_2[t]]\,m_2\,(4+\ell_2)\right\}\right\}$$

- **Calculate the guard:**

```
h = {{θ2[t]}};
A = DJacobian[h, q];
Adot = ∂t A;
dhdt = A.dq;
```

- **Define the kinematic constraint**

```
κ = {{θ2[t]}};
```

- **Compute the impact equations:**

```
ℰ = ∂{Flatten[q],1} Flatten[κ];
Pva = FullSimplify[dq -
     (1 + e) Inverse[𝒟].Transpose[ℰ].Inverse[ℰ.Inverse[𝒟].Transpose[ℰ]].ℰ.dq];
Pvb = FullSimplify[dq - (1 + e) Inverse[𝒟].Transpose[ℰ].
        Inverse[ℰ.Inverse[𝒟].Transpose[ℰ]].ℰ.dq /. e → 0];
R1a = {{q}, {Pva}, {Ia[t]}};
R1b = {{q[[1, 1]]}, {0}, {Flatten[Pvb][[1]]}, {0}, {Ia[t]}};
R2 = {{q}, {dq}, {Ia[t]}};
```

- **Control Law for periodic motion**

$$\theta_{1,e} = 0;$$

$$k = \frac{25}{10};$$

$$\theta_{1,e}' = 0;$$

$$c = \frac{-10}{10};$$

```
B = {{1}, {0}};

Ra = 1000/100;

K_ϕ = 177758/100;

K_e = 561/1000;

La = 80/10000;

Duty = {{-k (θ1[t] - θ1,e) - c (θ1'[t] - θ1,e')}}

Va = {{45 Duty}}

(*Vat ={{35}}*)

dIa = {{(Va - 53 K_e (θ1'[t]) - Ra (Ia[t]))/La}}

u = {{53 K_ϕ Ia[t] - 2/10 θ1'[t]}}
```

$$\left\{\left\{-\frac{5}{2}\,\theta_1[t] + (\theta_1)'[t]\right\}\right\}$$

$$\left\{\left\{\left\{\left\{45\left(-\frac{5}{2}\,\theta_1[t] + (\theta_1)'[t]\right)\right\}\right\}\right\}\right\}$$

$$\left\{\left\{\left\{\left\{\left\{\left\{125\left(-10\,\mathrm{Ia}[t] - \frac{29733\,(\theta_1)'[t]}{1000} + 45\left(-\frac{5}{2}\,\theta_1[t] + (\theta_1)'[t]\right)\right)\right\}\right\}\right\}\right\}\right\}\right\}$$

$$\left\{\left\{\frac{4710587\,\mathrm{Ia}[t]}{50} - \frac{1}{5}\,(\theta_1)'[t]\right\}\right\}$$

- **Calculate Lagrange multiplier for locked domain**

```
λ = -Simplify[Inverse[A.Inverse[𝒟].Transpose[A]].
      (A.Inverse[𝒟].(-C.dq - G + B.u) + Adot.dq)]
```

$$\left\{\left\{\left(\frac{1}{359\,552}\, m_2\, (4+\ell_2)\right.\right.\right.$$
$$\left(-1\,052\,198\,400\,\ell_1 + 320\,(138\,701 + 7500\,m_1)\,\ell_1^2 + 2809\,\left(321\,048\,221 + 4544\,\ell_2^2\right) + \right.$$
$$\left. 10\,786\,560\,m_2\,\left(4\,\ell_1^2 + 4\,\text{Cos}[\theta_2[t]]\,\ell_1\,(4+\ell_2) + (4+\ell_2)^2\right)\right)$$
$$\left(g\,\text{Sin}[\theta_1[t] + \theta_2[t]] + \text{Sin}[\theta_2[t]]\,\ell_1\,(\theta_1)'[t]^2\right) +$$
$$\frac{1}{2650}\,\left(19\,758 + 71\,\ell_2^2 + 60\,m_2\,(4+\ell_2)\,(4 + 2\,\text{Cos}[\theta_2[t]]\,\ell_1 + \ell_2)\right)$$
$$\left(249\,661\,111\,\text{Ia}[t] - 5\,\left(125\,g\,\text{Sin}[\theta_1[t]]\,m_1\,\ell_1 + 106\,(\theta_1)'[t] + \right.\right.$$
$$265\,m_2\,\left(g\,\text{Sin}[\theta_1[t] + \theta_2[t]]\,(4+\ell_2) + \ell_1\,\left(2\,g\,\text{Sin}[\theta_1[t]] - 2\,\text{Sin}[\theta_2[t]]\right.\right.$$
$$\left.\left.\left.\left.\left.(4+\ell_2)\,(\theta_1)'[t]\,(\theta_2)'[t] - \text{Sin}[\theta_2[t]]\,(4+\ell_2)\,(\theta_2)'[t]^2\right)\right)\right)\right)\Big/$$
$$\left(240\,\left(\frac{\ell_1\,(-3\,288\,120 + (138\,701 + 7500\,m_1)\,\ell_1)}{134\,832} + \frac{321\,048\,221 + 4544\,\ell_2^2}{15\,360} + \right.\right.$$
$$\left.\left.\frac{1}{4}\,m_2\,\left(4\,\ell_1^2 + 4\,\text{Cos}[\theta_2[t]]\,\ell_1\,(4+\ell_2) + (4+\ell_2)^2\right)\right)\right)\Big\}\Big\}$$

```
f1 = FullSimplify[Join[dq, Inverse[𝒟].(B.u - C.dq - G)]]
(*f1t=FullSimplify[Join[dq,Inverse[𝒟].(B.u-C.dq-G),dIat]]*)
(*odes=Table[∂t q[[i,1]]→f1[[Length[q]+i,1]],{i,1,Length[q]}];*)
```

$$\Big\{\{(\theta_1)'[t]\},\ \{(\theta_2)'[t]\},$$

$$\Big\{\Big(\frac{1}{2}\, m_2\ (4+\ell_2)\ \left(19\,758+71\,\ell_2^2+60\,m_2\ (4+\ell_2)\ (4+2\,\text{Cos}[\theta_2[t]]\,\ell_1+\ell_2)\right)$$
$$\left(g\,\text{Sin}[\theta_1[t]+\theta_2[t]]+\text{Sin}[\theta_2[t]]\,\ell_1\ (\theta_1)'[t]^2\right)+$$
$$\frac{1}{2650}\left(19\,758+71\,\ell_2^2+60\,m_2\ (4+\ell_2)^2\right)$$
$$(249\,661\,111\,\text{Ia}[t]+5\ (-125\,g\,\text{Sin}[\theta_1[t]]\,m_1\,\ell_1-106\ (\theta_1)'[t]+$$
$$265\,m_2\ (-g\,\text{Sin}[\theta_1[t]+\theta_2[t]]\ (4+\ell_2)+\ell_1\ (-2\,g\,\text{Sin}[\theta_1[t]]+$$
$$\text{Sin}[\theta_2[t]]\ (4+\ell_2)\ (\theta_2)'[t]\ (2\ (\theta_1)'[t]+(\theta_2)'[t])))))\Big)\Big/$$
$$\Big(240\left(-\frac{\left(19\,758+71\,\ell_2^2+60\,m_2\ (4+\ell_2)\ (4+2\,\text{Cos}[\theta_2[t]]\,\ell_1+\ell_2)\right)^2}{57\,600}+\right.$$
$$\frac{1}{240}\left(19\,758+71\,\ell_2^2+60\,m_2\ (4+\ell_2)^2\right)\left(\frac{\ell_1\ (-3\,288\,120+(138\,701+7500\,m_1)\,\ell_1)}{134\,832}+\right.$$
$$\left.\left.\left.\frac{321\,048\,221+4544\,\ell_2^2}{15\,360}+\frac{1}{4}\,m_2\ \left(4\,\ell_1^2+4\,\text{Cos}[\theta_2[t]]\,\ell_1\ (4+\ell_2)+(4+\ell_2)^2\right)\right)\right)\Big)\Big\},$$

$$\Big\{-\Big(\frac{1}{359\,552}\,m_2\ (4+\ell_2)\ \left(320\,\ell_1\ (-3\,288\,120+(138\,701+7500\,m_1)\,\ell_1)+2809\ \left(321\,048\,221+\right.\right.$$
$$\left.\left.4544\,\ell_2^2\right)+10\,786\,560\,m_2\ \left(4\,\ell_1^2+4\,\text{Cos}[\theta_2[t]]\,\ell_1\ (4+\ell_2)+(4+\ell_2)^2\right)\right)$$
$$\left(g\,\text{Sin}[\theta_1[t]+\theta_2[t]]+\text{Sin}[\theta_2[t]]\,\ell_1\ (\theta_1)'[t]^2\right)+$$
$$\frac{1}{2650}\left(19\,758+71\,\ell_2^2+60\,m_2\ (4+\ell_2)\ (4+2\,\text{Cos}[\theta_2[t]]\,\ell_1+\ell_2)\right)$$
$$(249\,661\,111\,\text{Ia}[t]+5\ (-125\,g\,\text{Sin}[\theta_1[t]]\,m_1\,\ell_1-106\ (\theta_1)'[t]+$$
$$265\,m_2\ (-g\,\text{Sin}[\theta_1[t]+\theta_2[t]]\ (4+\ell_2)+\ell_1\ (-2\,g\,\text{Sin}[\theta_1[t]]+$$
$$\text{Sin}[\theta_2[t]]\ (4+\ell_2)\ (\theta_2)'[t]\ (2\ (\theta_1)'[t]+(\theta_2)'[t])))))\Big)\Big/$$
$$\Big(240\left(-\frac{\left(19\,758+71\,\ell_2^2+60\,m_2\ (4+\ell_2)\ (4+2\,\text{Cos}[\theta_2[t]]\,\ell_1+\ell_2)\right)^2}{57\,600}+\right.$$
$$\frac{1}{240}\left(19\,758+71\,\ell_2^2+60\,m_2\ (4+\ell_2)^2\right)\left(\frac{\ell_1\ (-3\,288\,120+(138\,701+7500\,m_1)\,\ell_1)}{134\,832}+\right.$$
$$\left.\left.\left.\frac{321\,048\,221+4544\,\ell_2^2}{15\,360}+\frac{1}{4}\,m_2\ \left(4\,\ell_1^2+4\,\text{Cos}[\theta_2[t]]\,\ell_1\ (4+\ell_2)+(4+\ell_2)^2\right)\right)\right)\Big)\Big\}\Big\}$$

```
f2 = FullSimplify[Join[dq, Inverse[𝒟].(B.u + Transpose[A].λ - C.dq - G)] /.
   {θ2[t] → 0, θ2'[t] → 0}]
(*f2t=FullSimplify[Join[dq,Inverse[𝒟].(B.u+Transpose[A].λ-C.dq-G),dIat]/.
   {θ2[t]→0,θ2'[t]→0}]*)
```

```
{{(θ1)'[t]}, {0},
 {(81 408 (249 661 111 Ia[t] - 25 g Sin[θ1[t]] (25 m1 ℓ1 + 53 m2 (4 + 2 ℓ1 + ℓ2)) -
       530 (θ1)'[t])) / (5 (320 ℓ1 (-3 288 120 + (138 701 + 7500 m1) ℓ1) +
       10 786 560 m2 (4 + 2 ℓ1 + ℓ2)^2 + 2809 (321 048 221 + 4544 ℓ2^2)))}, {0}}
```

```
(*λdot=Simplify[∂t λ/.odes]*)
λdot = {{-1}};
```

- **Splice everything into a C file**

```
argsubs = Table[x[i] → "QARG(" <> ToString[i - 1] <> ")", {i, 1, 2 Length[q] + 1}]
```

```
{x[1] → QARG(0), x[2] → QARG(1), x[3] → QARG(2), x[4] → QARG(3), x[5] → QARG(4)}
```

```
assignToName[name_String, value_] :=
 ToExpression[name, InputForm, Function[var, var = value, HoldAll]]
toCShape[var_] :=
  Flatten[Transpose[var] /. constsubs /. statesubs /. argsubs] // N;
toCString[var_] := StringReplace[ToString[CForm[var]], "\"" → ""];
exprToC[var_] := Function[{va}, toCString[toCShape[va]]][var];
```

- **Convert expressions to C format**

```
xM = exprToC[𝒟];
xC = exprToC[C];
xG = exprToC[G];
xh1 = exprToC[h];
xh2 = exprToC[λ];
xA = exprToC[A];
xdh1dt = exprToC[dhdt];
xdh2dt = exprToC[λdot];
xR1a = exprToC[R1a];
xR1b = exprToC[R1b];
xR2 = exprToC[R2];

xVa = exprToC[Va];
xdIa = exprToC[dIa];
xu = exprToC[u];

xf1 = exprToC[f1];
xf1t = exprToC[f1t];
xf2 = exprToC[f2];
xf2t = exprToC[f2t];
```

- **Splice expressions into C template**

```
Splice["ccode\\eqns.c", "ccode\\geteqn.c",
 FormatType → TraditionalForm, PageWidth → 100 000]
```

```
ccode\eqns.c
```

The differential equation with the constants put in :

$$
\begin{aligned}
f1 = \Big\{ & \{\theta_1'[t]\},\ \{\theta_2'[t]\},\\
& \Big\{ \Big(\frac{1}{2500}\, 24\,437\,261 \Big(17\,754 + 625 \Big(\frac{33\,624\,689}{1\,000\,000} + \frac{121\,983 \left(\frac{557}{100} + \frac{457}{50} \operatorname{Cos}[\theta_2[t]] \right)}{2500} \Big) \Big) \\
& \Big(\frac{981}{100} \operatorname{Sin}[\theta_1[t] + \theta_2[t]] + \frac{457 \operatorname{Sin}[\theta_2[t]]\, \theta_1'[t]^2}{1000} \Big) - \\
& 1/1600 \quad 333\,809\,213 \Big(-2\,930\,476\, \mathrm{Ia}[t] + \frac{76\,251\,100\,311 \operatorname{Sin}[\theta_1[t]]}{1\,000\,000} + \\
& 2404\, \theta_1'[t] + \frac{43\,873}{25} \Big(\frac{546\,417 \operatorname{Sin}[\theta_1[t] + \theta_2[t]]}{10\,000} + \\
& \frac{457 \left(\frac{981}{5} \operatorname{Sin}[\theta_1[t]] - \frac{557}{100} \operatorname{Sin}[\theta_2[t]]\, \theta_2'[t]\, (2\, \theta_1'[t] + \theta_2'[t]) \right)}{1000} \Big) \Big) \Big) \Big/ \\
& \Big(9\,015\,000\,000 \Big(\frac{333\,809\,213 \left(\frac{2\,678\,595\,665\,635\,049}{433\,441\,200\,000\,000} + \frac{73 \left(\frac{229\,129}{2000} + \frac{254\,549 \operatorname{Cos}[\theta_2[t]]}{2500} \right)}{10\,000} \right)}{1\,200\,000\,000} - \\
& \Big(\frac{2959}{125\,000} + \frac{\frac{33\,624\,689}{1\,000\,000} + \frac{121\,983 \left(\frac{557}{100} + \frac{457}{50} \operatorname{Cos}[\theta_2[t]] \right)}{2500}}{1200} \Big)^2 \Big) \Big) \Big\}, \\
& \Big\{ - \Big(\frac{1}{2500}\, 40\,661 \Big(\frac{2\,678\,595\,665\,635\,049}{400} + 7\,910\,301\,900 \Big(\frac{229\,129}{2000} + \frac{254\,549 \operatorname{Cos}[\theta_2[t]]}{2500} \Big) \Big) \\
& \Big(\frac{981}{100} \operatorname{Sin}[\theta_1[t] + \theta_2[t]] + \frac{457 \operatorname{Sin}[\theta_2[t]]\, \theta_1'[t]^2}{1000} \Big) +
\end{aligned}
$$

$$2404\left(17\,754+625\left(\frac{33\,624\,689}{1\,000\,000}+\frac{121\,983\left(\frac{557}{100}+\frac{457}{50}\,\text{Cos}[\theta_2[t]]\right)}{2500}\right)\right)\left(2\,930\,476\,\text{Ia}[t]-\frac{76\,251\,100\,311\,\text{Sin}[\theta_1[t]]}{1\,000\,000}-2404\,\theta_1'[t]+\frac{43\,873}{25}\left(-\frac{546\,417\,\text{Sin}[\theta_1[t]+\theta_2[t]]}{10\,000}+\frac{457\left(-\frac{981}{5}\,\text{Sin}[\theta_1[t]]+\frac{557}{100}\,\text{Sin}[\theta_2[t]]\,\theta_2'[t]\,(2\,\theta_1'[t]+\theta_2'[t])\right)}{1000}\right)\right)\Big/$$

$$\left(21\,672\,060\,000\,000\left(\frac{333\,809\,213\left(\frac{2\,678\,595\,665\,635\,049}{433\,441\,200\,000\,000}+\frac{73\left(\frac{229\,129}{2000}+\frac{254\,549\,\text{Cos}[\theta_2[t]]}{2500}\right)}{10\,000}\right)}{1\,200\,000\,000}-\left(\frac{2959}{125\,000}+\frac{\frac{33\,624\,689}{1\,000\,000}+\frac{121\,983\left(\frac{557}{100}+\frac{457}{50}\,\text{Cos}[\theta_2[t]]\right)}{2500}}{1200}\right)^2\right)\right)\Big\}\Big\}$$

$$\Big\{\{\theta_1'[t]\},\{\theta_2'[t]\},\Big\{\Big(\frac{1}{2500}24\,437\,261\left(17\,754+625\left(\frac{33\,624\,689}{1\,000\,000}+\frac{121\,983\left(\frac{557}{100}+\frac{457}{50}\,\text{Cos}[\theta_2[t]]\right)}{2500}\right)\right)\left(\frac{981}{100}\,\text{Sin}[\theta_1[t]+\theta_2[t]]+\frac{457\,\text{Sin}[\theta_2[t]]\,\theta_1'[t]^2}{1000}\right)-1/1600\;\;333\,809\,213\left(-2\,930\,476\,\text{Ia}[t]+\frac{76\,251\,100\,311\,\text{Sin}[\theta_1[t]]}{1\,000\,000}+2404\,\theta_1'[t]+\frac{43\,873}{25}\left(\frac{546\,417\,\text{Sin}[\theta_1[t]+\theta_2[t]]}{10\,000}+\right.\right.\right.$$

$$\left.\left.\left.\frac{457\left(\frac{981}{5}\,\text{Sin}[\theta_1[t]]-\frac{557}{100}\,\text{Sin}[\theta_2[t]]\,\theta_2'[t]\,(2\,\theta_1'[t]+\theta_2'[t])\right)}{1000}\right)\right)\right)\Big/$$

$$\left(9\,015\,000\,000\left(\frac{333\,809\,213\left(\frac{2\,678\,595\,665\,635\,049}{433\,441\,200\,000\,000}+\frac{73\left(\frac{229\,129}{2000}+\frac{254\,549\,\text{Cos}[\theta_2[t]]}{2500}\right)}{10\,000}\right)}{1\,200\,000\,000}-\right.\right.$$

$$\left.\left.\left.\left(\frac{2959}{125\,000}+\frac{\frac{33\,624\,689}{1\,000\,000}+\frac{121\,983\left(\frac{557}{100}+\frac{457}{50}\,\text{Cos}[\theta_2[t]]\right)}{2500}}{1200}\right)^2\right)\right)\right\},$$

$$\left\{\left(-\frac{1}{2500}40\,661\left(\frac{2\,678\,595\,665\,635\,049}{400}+7\,910\,301\,900\left(\frac{229\,129}{2000}+\frac{254\,549\,\text{Cos}[\theta_2[t]]}{2500}\right)\right)\right.\right.$$

$$\left(\frac{981}{100}\,\text{Sin}[\theta_1[t]+\theta_2[t]]+\frac{457\,\text{Sin}[\theta_2[t]]\,\theta_1'[t]^2}{1000}\right)-$$

$$2404\left(17\,754+625\left(\frac{33\,624\,689}{1\,000\,000}+\frac{121\,983\left(\frac{557}{100}+\frac{457}{50}\,\text{Cos}[\theta_2[t]]\right)}{2500}\right)\right)\left(2\,930\,476\,\text{Ia}[t]-\right.$$

$$\frac{76\,251\,100\,311\,\text{Sin}[\theta_1[t]]}{1\,000\,000}-2404\,\theta_1'[t]+\frac{43\,873}{25}\left(-\frac{546\,417\,\text{Sin}[\theta_1[t]+\theta_2[t]]}{10\,000}+\right.$$

$$\left.\left.\left.\frac{457\left(-\frac{981}{5}\,\text{Sin}[\theta_1[t]]+\frac{557}{100}\,\text{Sin}[\theta_2[t]]\,\theta_2'[t]\,(2\,\theta_1'[t]+\theta_2'[t])\right)}{1000}\right)\right)\right)\Big/$$

$$\left(21\,672\,060\,000\,000\left(\frac{333\,809\,213\left(\frac{2\,678\,595\,665\,635\,049}{433\,441\,200\,000\,000}+\frac{73\left(\frac{229\,129}{2000}+\frac{254\,549\,\text{Cos}[\theta_2[t]]}{2500}\right)}{10\,000}\right)}{1\,200\,000\,000}-\right.\right.$$

$$\left.\left.\left.\left(\frac{2959}{125\,000}+\frac{\frac{33\,624\,689}{1\,000\,000}+\frac{121\,983\left(\frac{557}{100}+\frac{457}{50}\,\text{Cos}[\theta_2[t]]\right)}{2500}}{1200}\right)^2\right)\right)\right\}\right\}$$

Taking out the theta2 component,
and putting in the requirement that we are at a Zeno equilibrium point (theta2 = theta2dot = 0):

```
hddotexpr = FullSimplify[N[First[f1[[4]]]] //. {θ2[t] → 0, θ2'[t] → 0}]
```

```
0. - 91.2473 Ia[t] - 25.394 Sin[θ1[t]] + 0.0748542 θ1'[t]
```

Now make hddot a function of three variables.

```
hddot[x_, y_, z_] := hddotexpr //. {θ1[t] → x, θ1'[t] → y, Ia[t] → z}
hddot[x, y, z]
```

```
0. + 0.0748542 y - 91.2473 z - 25.394 Sin[x]
```

Plotting hddot to determine the region where it is negative :

```
RegionPlot3D[hddot[x, y, z] ≤ 0, {x, -Pi / 2, Pi / 2}, {y, -2, 2},
 {z, -2, 2}, AxesLabel → {"θ1[t]", "θ1'[t]", "Ia[t]"}]
```

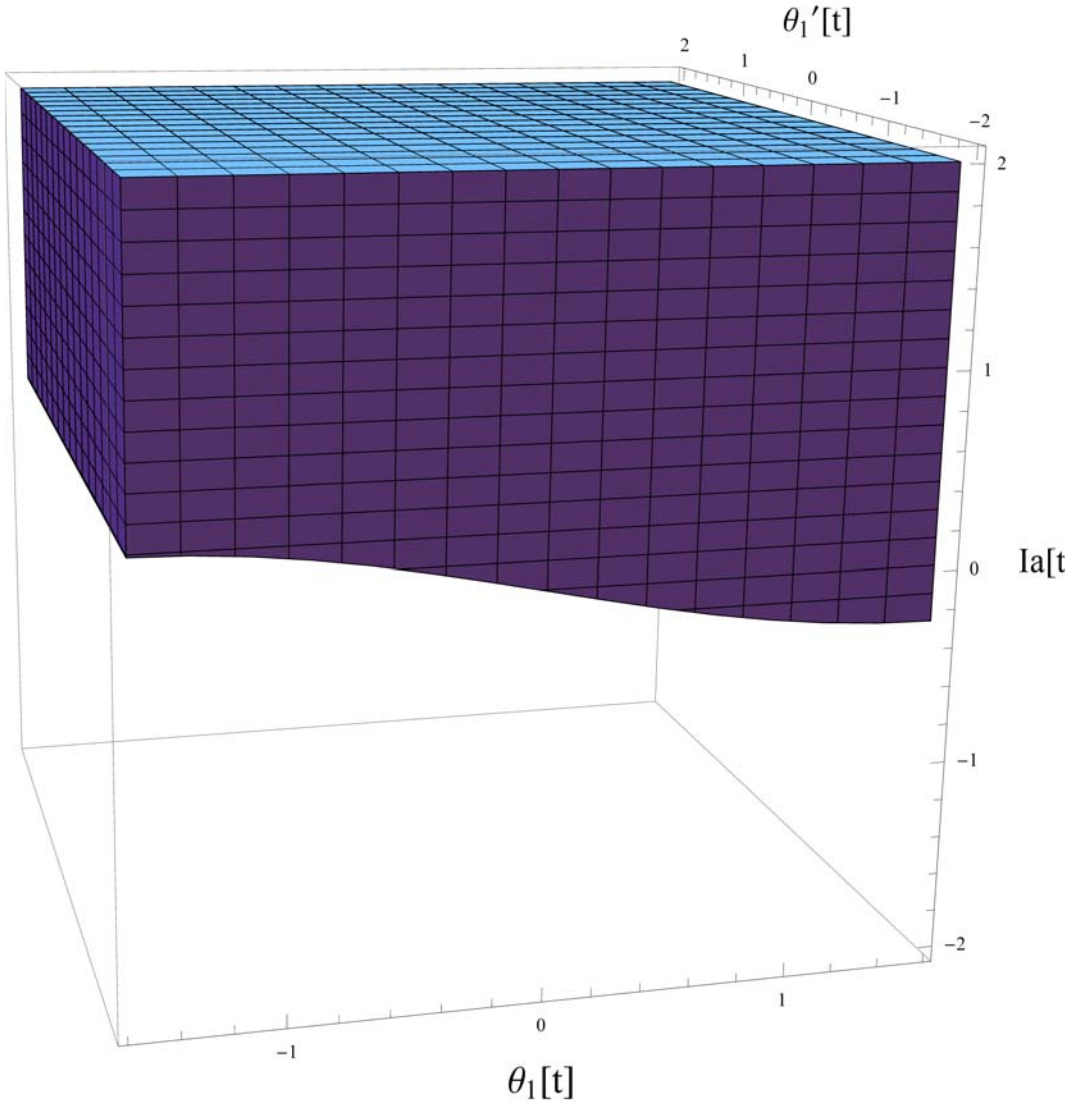

What we can say from this plot : Essentially, we will have stable Zeno equilibria for any value of theta1 and theta2 as long as the current is positive. Therefore, the stable equilibria of the system are the points where the pendulum is swinging from right to left, and it does not matter if the pendulum is on the " left " side or on the " right " side.

Therefore, the theory validates where we see Zeno behavior, and the Zeno periodic orbits that we see. In addition, this analysis motivates the introduction of completed hybrid systems since we will have Zeno behavior at a large collection of points.

VITA

Name:	Bhargav Kothapalli
Address:	Department of Mechanical Engineering, 3123 TAMU College Station, TX 77843
Email Address:	kbhargav1985@yahoo.com
Education:	B.Tech., Mechanical Engineering, Jawaharlal Nehru Technological University, India, 2007 M.S., Mechanical Engineering, Texas A&M University, 2011